



UNIVERSITÀ
DEGLI STUDI
FIRENZE

SCUOLA DI SCIENZE MATEMATICHE,
FISICHE E NATURALI

CORSO DI LAUREA MAGISTRALE
IN SCIENZE FISICHE E ASTROFISICHE

Production of homogeneous ultracold atomic gases

Produzione di gas atomici ultrafreddi
omogenei

Candidate

Alberto Terenzi (ID number 7120730)

Thesis Advisor

Dr.ssa Giulia Del Pace

Co-Advisor

Dr. Giacomo Roati

Academic Year 2024/2025

Thesis defended on 21 October 2025
in front of a Board of Examiners composed by:
Prof. Chiara Fort (chairman)

Production of homogeneous ultracold atomic gases
Tesi di Laurea Magistrale. University of Florence

© 2025 Alberto Terenzi. All rights reserved

This thesis has been typeset by \LaTeX and the UniFiTh class.

Version: December 15, 2025

Author's email: alberto.terenzi@lens.unifi.it

*Dedicato a Elio
Da sempre la persona che ha stimolato la mia curiosità.*

*Ci sono cose che non capiamo per niente,
ed altre che capiamo ancora di meno
Franco Aste*

Contents

Introduction	vii
1 Quantum gases in box potentials	1
1.1 Fermions and Bosons	1
1.1.1 Fermions or Bosons in a box potential	3
1.2 Scattering theory and Feshbach resonances	5
1.2.1 The BEC-BCS crossover	7
1.3 Harmonic potentials, BOX potentials and differences	9
1.3.1 Harmonic potential	9
1.3.2 Box potential	12
1.3.3 Comparison Harmonic-Box potentials	13
2 Box potential for Ultracold Li-6	15
2.1 Experimental setup	15
2.2 Imaging Systems	18
2.2.1 Absorption Imaging	19
2.2.2 Horizontal Imaging Setup	20
2.2.3 Vertical Imaging Setup	20
2.3 Design of the box potential	21
2.3.1 Simulation of the Box Optical Trap	21
2.3.2 Digital Micromirror Device	22
2.3.3 DMD optical properties	23
2.3.4 DMD control and feedback process	27
2.4 Optical set up for box confinement	29
2.4.1 The Laser	29
2.4.2 Optical set up	29
2.5 Making the Box Potential Uniform	34
2.5.1 Aligning, focusing and fine tuning the DMD setup	34
2.5.2 Gravity compensation	35
2.5.3 Gradients compensation	41
3 Probing quantum statistics	45
3.1 Expansion model	45
3.2 Fermi distribution	47
3.2.1 Preparation of the gas	47
3.2.2 Time of flight analysis	47

3.2.3	Momentum distribution	52
3.3	Bose distribution	54
3.3.1	Production of the gas	54
3.3.2	Momentum distribution	55
3.3.3	Time of flight analysis	59
4	Conclusions and outlooks	63
A	Atoms light interaction	65
A.1	Atom light interaction	65
A.2	Photon Absorption and Re-emission	66
A.3	Optical Dipole Force and Potentials	66

Introduction

The field of ultracold atomic gases has developed over the past three decades into one of the most versatile and powerful platforms for the study of quantum many-body physics [1]. By cooling dilute atomic ensembles to temperatures of the order of nanokelvin, it is possible to realize systems in which quantum statistics and interactions dictate the macroscopic behavior, giving rise to a wealth of emergent phenomena. One of the key features that has made ultracold gases so successful is the possibility to confine and manipulate atoms in externally applied potentials with a high degree of control and flexibility. Optical and magnetic techniques allow researchers to design trapping geometries that go far beyond the traditional harmonic confinement, effectively creating model systems for a wide spectrum of problems in condensed matter, statistical physics, and quantum simulation [1, 2].

Already in the early days of the field, a variety of trapping configurations were implemented to address specific questions in many-body physics. Low-dimensional traps were developed to study the crossover between one-, two-, and three-dimensional systems [3–6], opening new avenues to observe the role of dimensionality in superfluidity and quantum correlations. Double-well potentials made it possible to investigate quantum tunneling and coherence phenomena [7], while optical lattices created periodic landscapes for atoms that closely mimic the crystalline structure of solids [2]. The possibility of dynamically tuning such potentials has been another defining aspect of ultracold atom research [8], enabling experiments that probe out-of-equilibrium dynamics, the excitation spectrum, and even the reversible crossing of phase transitions [9–11]. In this sense, the external control of the trapping environment has represented a decisive experimental degree of freedom, comparable in importance to interaction tuning via Feshbach resonances.

In more recent years, the capability of shaping light fields with high spatial precision has led to a further leap in the design of trapping geometries. Among the most important advances is the realization of *uniform box potentials*, sometimes referred to as flat-bottom traps [12–14]. While the harmonic oscillator potential has traditionally been the standard workhorse of ultracold atom experiments [15, 16], it imposes a non-uniform density distribution that complicates the comparison between experiment and theory. Physical observables are spatially averaged over a cloud whose density varies significantly from the center to the edges, often obscuring critical behaviors or washing out sharp features predicted for homogeneous systems. By contrast, box traps enable the preparation of nearly uniform gases, in which the density is approximately constant over a large region of space. This uniformity greatly simplifies both the theoretical description of the system and the analysis of experimental data. More importantly, it opens the possibility of addressing qualitatively new questions that are inaccessible in harmonic confinement [17].

Homogeneous systems are of central importance in many branches of physics. Most theoretical models in statistical mechanics and quantum field theory are derived under the

assumption of translational invariance, which vastly simplifies the mathematical treatment. For example, properties such as the equation of state [18], excitation spectra [19], and scaling behavior near phase transitions [20] are most naturally formulated in the homogeneous limit. Ultracold gases in box traps provide an experimental platform where these theoretical predictions can be directly tested in controlled conditions. This capability marks a transition from studying systems with external confinement to truly realizing many-body physics “in the bulk,” allowing precise connection between ultracold atom experiments and fundamental questions of condensed matter and high-energy physics.

The implementation of box potentials has already led to important experimental successes. These include the observation of critical phenomena in low-dimensional uniform gases [12] and the characterization of thermodynamic properties of Fermi and Bose gases with unprecedented precision [17]. Furthermore, box traps allow for the investigation of domain formation [21], non-equilibrium phenomena such as quench dynamics across phase transitions [22], and universality in the scaling laws of defect production [23]. In combination with state-of-the-art imaging techniques, homogeneous systems open the door to spatially resolved studies of correlations, topological defects, and collective excitations in regimes that had previously been inaccessible [24].

It is important to emphasize that the recent progress in box trapping is part of a broader development in the field of light shaping for ultracold atoms. Advances in optical technologies such as spatial light modulators, digital micromirror devices, and holographic beam shaping techniques have provided the ability to generate highly customizable trapping landscapes [8]. This has not only made homogeneous box traps possible, but has also stimulated progress in related areas. One example is the design of ring-shaped traps [25], which serve as building blocks of the study of persistent currents and quantized circulation [26, 27], allowing the study of atomtronic circuits. Another is the use of arrays of tightly focused optical tweezers, where individual atoms or molecules can be trapped and manipulated with single-particle resolution [28]. These different directions highlight the ongoing trend of bringing the level of control over neutral atoms closer to that already established in quantum optics and solid-state systems.

Within this landscape, the realization of homogeneous box potentials represents not only a technical achievement but also an important step forward for quantum simulation [29]. By minimizing density inhomogeneities and allowing direct comparison with translationally invariant theoretical models, box traps enable more faithful implementations of many-body Hamiltonians. This brings ultracold atomic systems closer to the goal of quantitatively reproducing the behavior of idealized models under well-controlled experimental conditions. In addition, this opens access to a direct comparison with other quantum simulators since the properties are just directly linked to the density of the system.

Building upon these advances, the present thesis is dedicated to the implementation of a uniform optical box trap. The motivation is twofold. On one hand, the creation of a homogeneous potential represents a crucial step toward experiments that directly connect ultracold atom physics to homogeneous theoretical models. On the other hand, the practical realization of such potentials poses technical and conceptual challenges, from the optical design and alignment of the trapping beams to the characterization of homogeneity in the presence of experimental imperfections such as optical aberrations and gravity. The implementation of a box trap is therefore not only a necessary step toward fundamental experiments, but also an opportunity to explore state-of-the-art optical control methods.

Thesis outline

This manuscript is structured as follows:

- **Chapter 1** introduces the general context of ultracold atomic gases, focusing on the distinct properties of fermions and bosons. It reviews atomic interactions and the experimental techniques for their control, such as Feshbach resonances. The chapter concludes with a comparison between harmonic and box trapping potentials, highlighting their differences and implications for quantum gas research.
- **Chapter 2** presents the experimental realization of a uniform box potential for ${}^6\text{Li}$ atoms. It describes the main components of the experimental apparatus, including vacuum and laser systems, and the absorption imaging for atom detection. The chapter details the design and simulation of the optical trap using a Digital Micromirror Device, alongside the optical configuration and active feedback for stability. Special emphasis is placed on procedures for obtaining a homogeneous potential, including alignment, gravity compensation, and minimization of optical gradients.
- **Chapter 3** focuses on probing the quantum statistical properties of ultracold gases in the box trap. It introduces the theoretical model of atomic expansion after release and reports on the preparation and characterization of fermionic and bosonic gases. The chapter includes a careful examination of the validity of the model, which requires sufficiently long time-of-flight to ensure that the resulting momentum distributions faithfully reflect the quantum statistical properties of the trapped gases, thereby demonstrating clear signatures of bosonic and fermionic behavior.
- **Chapter 4** discusses possible future directions and applications of box potentials. It addresses the scientific opportunities opened by homogeneous trapping, such as exploring new many-body phenomena and non-equilibrium dynamics, and outlines potential technical enhancements to the setup.

Chapter 1

Quantum gases in box potentials

In this chapter, the fundamentals of quantum statistics for bosonic and fermionic systems will be introduced, with particular emphasis on gases confined in box potentials. The discussion will then briefly review the essential concepts of scattering theory and highlight the distinctive nature of the BEC-BCS crossover. Finally, a comparison will be made between the main properties exhibited by bosonic and fermionic gases trapped in harmonic and box potentials.

1.1 Fermions and Bosons

The most convenient framework for studying the quantum statistical properties of a non-interacting gas is the grand canonical ensemble, where analytical calculations are particularly tractable. In this formalism, the probability of realizing a configuration with N particles in a state of momentum $\hbar k$, with associated single-particle energy E_k , is given by [30]

$$P_N(E_k) = e^{-\beta(E_k - \mu N)}, \quad (1.1)$$

where $\beta = 1/k_B T$, μ is the chemical potential of the reservoir with which the system is in thermal equilibrium, and T is the temperature.

For a free particle of mass m , the dispersion relation between the energy and the wave vector k is simply

$$E_k = \frac{\hbar^2 k^2}{2m}, \quad (1.2)$$

where $\hbar = \frac{h}{2\pi}$ and h is the Planck constant.

Since we are working in the grand canonical ensemble, the total particle number is not fixed but rather fluctuates around an average value. The grand canonical partition function of the gas can be written as

$$Z = \sum_{N=0}^{\infty} \sum_{\{n_k\}} e^{-\beta \sum_k (E_k - \mu) n_k}, \quad (1.3)$$

where $N = \sum_k n_k$. The sum over $\{n_k\}$ runs over all possible microscopic configurations consistent with a fixed N .

To extract the average occupation number of the state with energy E_k from Eq.1.3, we must take into account the quantum statistics of the particles. For fermions, the Pauli

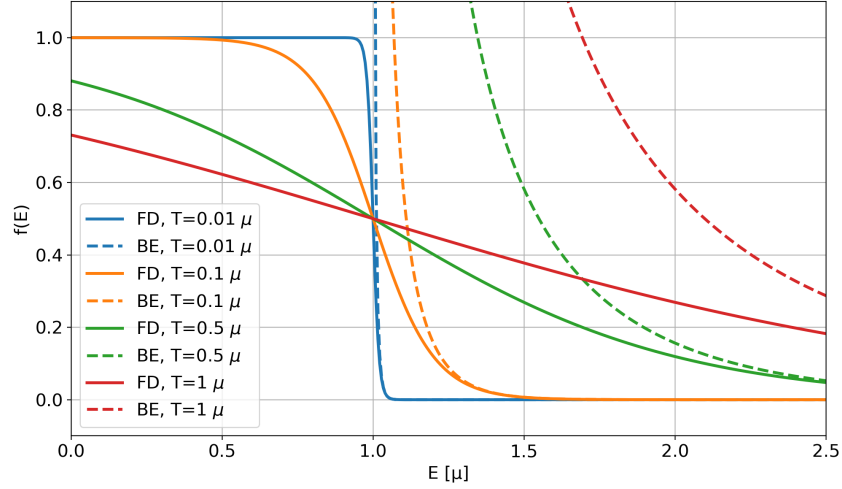


Figure 1.1. Comparison of Fermi–Dirac (solid lines) and Bose–Einstein (dashed lines) occupation distributions as a function of energy for several temperatures. Due to the Pauli exclusion principle, Fermi–Dirac occupation is limited to 1, while Bose–Einstein occupation can diverge at low energies. In the plot we consider natural units $k_B = 1$.

exclusion principle dictates that each state can be occupied by at most one particle, such as $n_k = 0$ or 1. This constraint makes the calculation of the partition function straightforward, leading to the well-known Fermi-Dirac distribution for the average occupation number:

$$\langle n_k \rangle_F = \frac{1}{e^{\beta(E_k - \mu)} + 1}. \quad (1.4)$$

In contrast, for bosons multiple occupation numbers are allowed ($n_k = 0, 1, 2, \dots$) and the partition function involves a geometric series, and the average occupation number is given by the Bose-Einstein distribution:

$$\langle n_k \rangle_B = \frac{1}{e^{\beta(E_k - \mu)} - 1}, \quad (1.5)$$

with the condition $\mu < E_0$ (the ground-state energy) ensuring convergence [30].

The major difference between the two statistics is revealed in the occupation of the low-energy states (see fig. 1.1) in the limit $T \rightarrow 0$.

For bosons, below a critical temperature T_c , the ground state can acquire a macroscopic occupation, giving rise to Bose-Einstein condensation [15]. The number of atoms in this case can be expressed as

$$N = N_0 + \sum_{k \neq 0} \langle n_k \rangle_B, \quad (1.6)$$

where N_0 denotes the condensate population. At $T = 0$, all particles collapse into the lowest-energy single-particle state $N_0 \rightarrow N$.

Fermions, on the other hand, behave in a fundamentally different way. Due to the exclusion principle, at $T = 0$ each single-particle state is occupied by at most one particle (per spin component). The system therefore fills all available states starting from the lowest energy up to the so-called Fermi energy E_F . This defines the Fermi surface in momentum

space, with a characteristic Fermi wave vector k_F such that

$$E_F = \frac{\hbar^2 k_F^2}{2m} \quad (1.7)$$

where the Fermi wave vector is defined for an homogeneous gas, as:

$$k_F = \left(\frac{6\pi^2 N}{g_s V} \right)^{1/3} \quad (1.8)$$

where g_s is multiplicity of spin. At finite temperatures, fermionic excitations appear only near the Fermi surface, within an energy window of order $k_B T$, which is the key feature underlying the stability of the degenerate Fermi gas [31].

In summary, while both bosons and fermions can be treated within the grand canonical ensemble, their statistical properties diverge dramatically: bosons may undergo Bose-Einstein condensation with macroscopic occupation of the ground state, whereas fermions build a Fermi sea, filling states up to E_F with a sharp cutoff at zero temperature.

1.1.1 Fermions or Bosons in a box potential

In general, the presence of an external trapping potential modifies the statistical properties of an ideal gas. Here we focus on the case of a three-dimensional box potential [12, 13], defined as

$$V(x, y, z) = \begin{cases} 0 & \text{if } 0 < x < L_x, 0 < y < L_y, 0 < z < L_z, \\ +\infty & \text{elsewhere.} \end{cases} \quad (1.9)$$

Within this potential, the single-particle eigenvalues and eigenfunctions follow directly from the Schrödinger equation:

$$\left[\frac{\hbar^2 (\hat{k}_x^2 + \hat{k}_y^2 + \hat{k}_z^2)}{2m} + \hat{V}(x, y, z) \right] \psi(x, y, z) = E \psi(x, y, z). \quad (1.10)$$

The normalized eigenstates are:

$$\psi_{n_x, n_y, n_z}(x, y, z) = \prod_{\xi=x, y, z} \sqrt{\frac{2}{L_\xi}} \sin\left(\frac{\pi \xi}{L_\xi} n_\xi\right), \quad (1.11)$$

with corresponding energies:

$$E_{n_x, n_y, n_z} = \sum_{\xi=x, y, z} \frac{\hbar^2}{8mL_\xi^2} n_\xi^2, \quad (1.12)$$

with $n_\xi = 1, 2, 3, \dots$

For a many-particle system of non-interacting atoms in such a potential, the state of the system can be described by the semiclassical distribution function in phase space,

$$f_{B,F}(\vec{r}, \vec{p}) = \frac{1}{e^{\beta \left(\frac{|\vec{p}|^2}{2m} + V(\vec{r}) - \mu \right)} \mp 1}, \quad (1.13)$$

where the minus sign applies to bosons and the plus sign to fermions.

At finite temperature ($T \neq 0$), the spatial density is then obtained by integrating over momenta:

$$n_{B,F}(\vec{r}) = \frac{g_s}{(2\pi\hbar)^3} \int d^3p f_{B,F}(\vec{r}, \vec{p}) = \pm \frac{g_s}{\lambda_{dB}^3} \text{Li}_{3/2}(\pm e^{\beta\mu}), \quad (1.14)$$

where g_s is the spin degeneracy, $\lambda_{dB} = \sqrt{\frac{h^2}{2\pi m k_B T}}$ is the thermal de Broglie wavelength, and $\text{Li}_s(z)$ is the polylogarithm function of order s , defined as

$$\text{Li}_s(z) = \sum_{k=1}^{\infty} \frac{z^k}{k^s}. \quad (1.15)$$

As can be seen, the density is position-independent, indicating that the system is uniform. This holds within the semiclassical approximation, where the discreteness of quantum states is neglected, and is therefore valid in the regime of large particle numbers.

The total number of particles follows from spatial integration:

$$N_{B,F} = \int_0^{L_x} \int_0^{L_y} \int_0^{L_z} d^3r n_{B,F}(\vec{r}) = V n_{B,F}, \quad (1.16)$$

with $V = L_x L_y L_z$ the box volume.

The thermal wavelength λ_{dB} introduces a natural length scale [32]. Quantum degeneracy sets in when λ_{dB} becomes comparable to the mean interparticle spacing which is linked on the other hand to the density of the system

$$d \sim n^{-1/3}. \quad (1.17)$$

For fermions the density itself defines the Fermi temperature,

$$T_F = \frac{E_F}{k_B}, \quad E_F = \frac{\hbar^2}{2m} \left(\frac{6\pi^2}{g_s} n \right)^{2/3}, \quad (1.18)$$

below which the Fermi sea is formed and quantum statistics govern the system behavior.

For bosons, instead, the condition $\lambda_{dB} \gtrsim d$ signals the onset of Bose-Einstein condensation and one can define a critical temperature:

$$T_C = \frac{2\pi\hbar^2}{m k_B} \left(\frac{n}{\zeta(3/2)} \right)^{2/3}. \quad (1.19)$$

Below this temperature, a macroscopic number of bosons occupy the ground state of the box.

In the classical regime, $T \gg T_{F,C}$, one has $\lambda_{dB} \ll d$, and the gas follows in both cases a Maxwell–Boltzmann distribution.

In typical ultracold atom experiments, these degeneracy temperatures are below microkelvin. Thus, achieving and probing quantum statistics in a uniform box trap requires extreme control over cooling, but offers the advantage of a homogeneous system, closely mirroring the assumptions of textbook statistical mechanics.

1.2 Scattering theory and Feshbach resonances

So far, we have discussed the static properties of a non-interacting gas. However, the most intriguing features of physical systems usually emerge in the presence of interactions, as most real systems are inherently interacting. One of the most remarkable aspects of ultracold atomic gases is the ability to tune both the strength and the sign of interatomic interactions by means of *Feshbach resonances* [33]. This unique feature provides access to a wide range of interaction regimes.

Neutral atoms interact through the Lennard-Jones potential [34]:

$$V(r) = -\frac{C_6}{r^6} + \frac{C_{12}}{r^{12}}, \quad (1.20)$$

where $C_{6,12}$ are positive constants. The attractive $-r^{-6}$ term is short-ranged and quickly vanishes beyond a characteristic interparticle distance r_0 . At distances of a few Bohr radii ($a_0 \simeq 0.5 \text{ \AA}$), the electronic clouds of the atoms begin to overlap, and the Pauli exclusion principle induces a strong repulsion, accounted for by the r^{-12} term.

Since ultracold atoms systems are usually very dilute, the mean interparticle distance is much larger than the range of the interaction such as $nr_0^3 \ll 1$. In this regime, three-body processes are negligible, and the system is well described by elastic two-body collisions. Moreover, because the degeneracy condition is $n\lambda_{\text{dB}}^3 \simeq 1$, the thermal de Broglie wavelength λ_{dB} is much larger than r_0 . As a consequence, colliding atoms do not probe the microscopic details of the short-range potential, but rather experience an effective potential averaged over the wavefunction.

The scattering of two particles in a central potential is a standard topic in quantum mechanics. Far from the interaction region, the asymptotic wavefunction can be written as a superposition of incoming and scattered waves:

$$\psi_{\text{as}}(\mathbf{r}) \sim e^{i\mathbf{k}\cdot\mathbf{r}} + f(\mathbf{k}, \mathbf{k}') \frac{e^{ikr}}{r}, \quad (1.21)$$

where \mathbf{k} and \mathbf{k}' denote the incoming and outgoing momenta, respectively, and $f(\mathbf{k}, \mathbf{k}')$ is the scattering amplitude. The corresponding differential cross-section is:

$$\frac{d\sigma}{d\Omega} = |f(\mathbf{k}, \mathbf{k}')|^2. \quad (1.22)$$

Because the potential is central, the wavefunction can be expanded in partial waves:

$$\psi_{\text{as}}(\mathbf{r}) = \sum_l Y_l^0(\theta) \frac{u_l(r)}{r}, \quad (1.23)$$

where $Y_l^0(\theta)$ are the spherical harmonics with $m = 0$, and $u_l(r)$ is the radial component. Substitution into the Schrödinger equation yields

$$\left(\frac{\hbar^2}{2m} \frac{d^2}{dr^2} + \frac{\hbar^2 k^2}{2m} \right) u_l(r) = V_{\text{eff}}(r) u_l(r), \quad (1.24)$$

with the effective potential

$$V_{\text{eff}}(r) = V(r) + \frac{\hbar^2 l(l+1)}{2mr^2}. \quad (1.25)$$

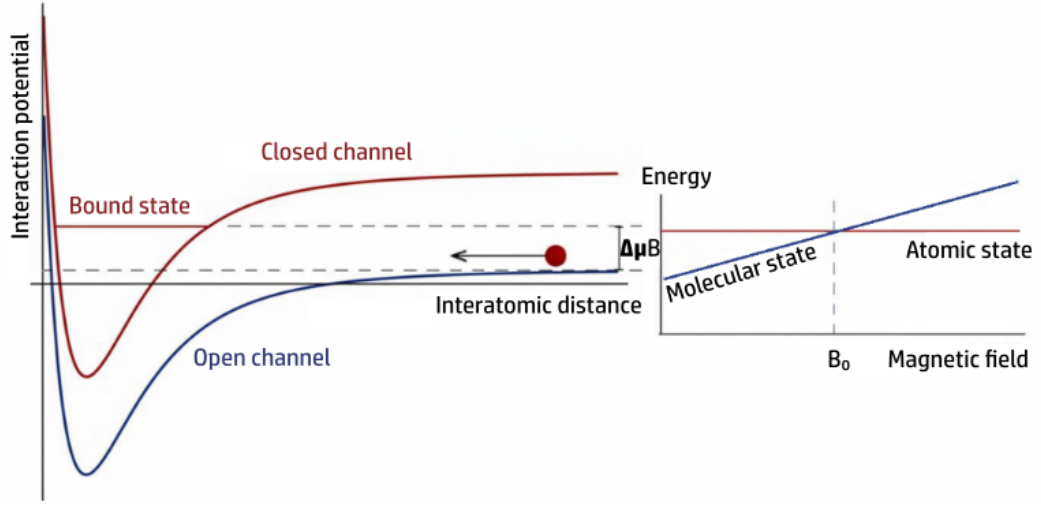


Figure 1.2. Closed and open channels for a scattering event (left): the closed channel presents a bound state that affects the properties of the scattering particles in the open channel. Thanks to the Zeeman effect, it is possible to tune the energy difference between the two channels with an external magnetic field (right). When $B = B_0$, the two channels are resonant and the scattering length diverges.

At low temperatures, the centrifugal barrier strongly suppresses all partial waves with $l > 0$, leaving only s -wave ($l = 0$) scattering. For fermions, the antisymmetry of the wavefunction prohibits s -wave collisions between identical fermions, whereas higher-order (p, d, \dots) channels are strongly suppressed at ultralow temperatures. Thus, ultracold identical fermions in a single spin state effectively do not interact. To restore interactions, one typically works either with different atomic species or, more commonly, with a mixture of fermions in two different hyperfine states. In this case, the spin part of the wavefunction ensures overall antisymmetry, while the spatial part is symmetric, allowing for s -wave collisions to occur.

For s -wave scattering, the asymptotic solution can be written as

$$u_0(r) \simeq \sin(kr - \delta_0(k)), \quad (1.26)$$

where $\delta_0(k)$ is the phase shift induced by the collision. Defining the scattering length as

$$a = -\lim_{k \rightarrow 0} \frac{\tan \delta_0(k)}{k}, \quad (1.27)$$

the interaction potential can be approximated by a contact pseudopotential:

$$V_p(r) = \frac{4\pi\hbar^2 a}{m} \delta(r). \quad (1.28)$$

Since the scattering length is usually much larger than r_0 , this approximation is well justified. Therefore, the properties of ultracold collisions are entirely determined by the scattering length a , whose sign and magnitude dictate whether interactions are attractive ($a < 0$) or repulsive ($a > 0$).

The interaction between two alkali atoms in different hyperfine states depends on their total electronic spin configuration, giving rise to both singlet and triplet potentials. The

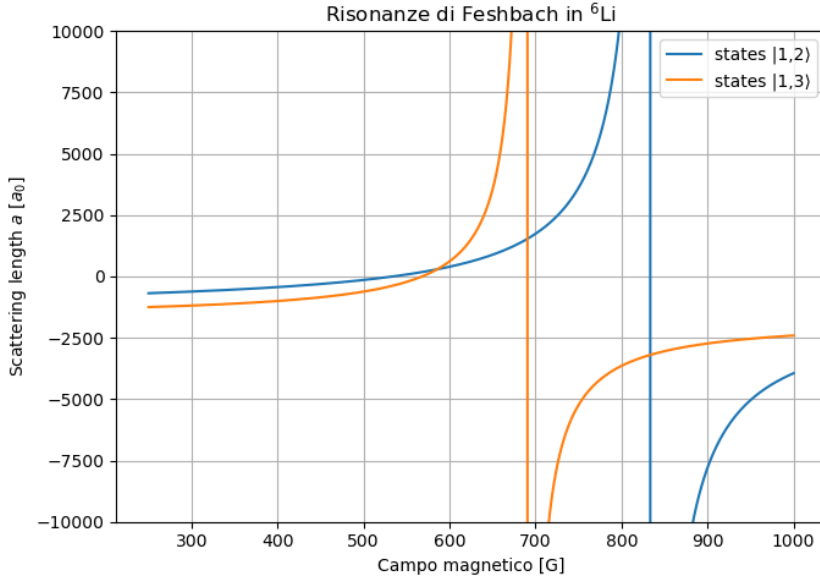


Figure 1.3. Feshbach resonances between the ground state and the first two excited hyperfine states for ${}^6\text{Li}$. The scattering length of s – wave collisions between two atom in different states depends on the external magnetic field. Thus, by changing this magnetic field we can effectively tune the interaction strength and sign over a wide range.

open channel corresponds to the scattering state of the incoming particles, while the closed channel contains bound states that may couple to the open channel via hyperfine interactions. If the bound state energy in the closed channel approaches that of the colliding atoms, the scattering length diverges, producing a Feshbach resonance.

Because the open and closed channels typically have different magnetic moments, the energy difference between them can be tuned with an external magnetic field. The magnetic-field dependence of the scattering length can be phenomenologically written as

$$a(B) = a_{\text{bg}} \left(1 - \frac{\Delta B}{B - B_0} \right), \quad (1.29)$$

where a_{bg} is the background scattering length, B_0 the resonance center, and ΔB its width.

A particularly attractive feature of Feshbach resonances is that both the magnitude and the sign of a can be tuned at will. This flexibility allows experimentalists to access a wide variety of regimes, from weakly to strongly interacting, and with either attractive or repulsive interactions. As we will see, we are interested in the specific case of ${}^6\text{Li}$, the lowest hyperfine states exhibit broad Feshbach resonances, which are extensively used in our experiments to study degenerate Fermi gases across different regimes.

1.2.1 The BEC-BCS crossover

The ability to control interactions provided by Feshbach resonances, combined with the ultralow temperatures achievable in Fermi gases allow to investigate the phenomenon of fermionic superfluidity [35]. This kind of superfluidity arises from the pairing of atoms in opposite spin states due to the presence of strong interactions between them. Fermionic pairs

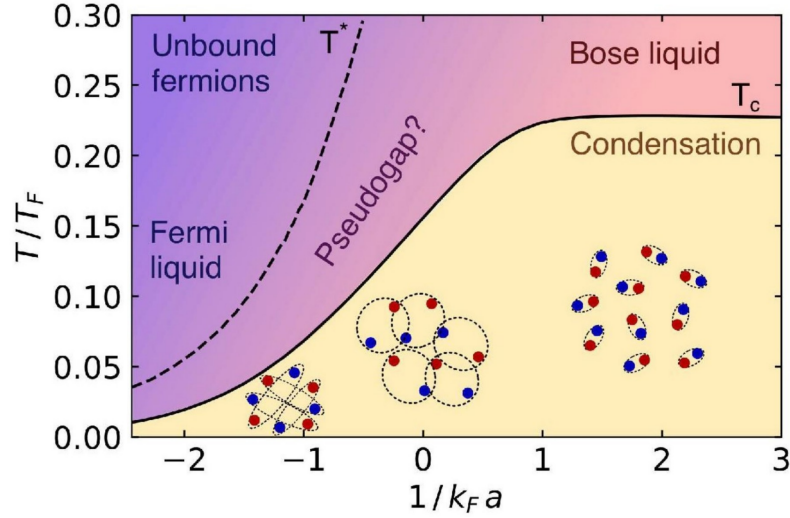


Figure 1.4. Phase diagram of the BEC-BCS crossover in a homogeneous fermionic gas. Below the pairing temperature T^* , fermions in opposite spin states form pairs. The pair size depends on the interaction parameter $1/k_F a$, where k_F is the Fermi momentum and a the s -wave scattering length tunable via Feshbach resonances. By varying $1/k_F a$, the system transitions smoothly from tightly bound molecules (BEC regime) to long-range Cooper pairs (BCS regime). The intermediate unitary Fermi gas (UFG) regime corresponds to maximum interaction strength and pair size comparable to interparticle spacing. Upon cooling below the critical temperature T_c , pairs condense, leading to fermionic superfluidity. The pseudogap region, where $T_c < T < T^*$, hosts preformed pairs that have not yet condensed. Image taken from [37]

are indeed bosons which can undergo Bose-Einstein condensation and display a superfluid behavior.

For attractive interactions, a Fermi gas is unstable towards the formation of long-range Cooper pairs, analogous to the mechanism described by Bardeen–Cooper–Schrieffer (BCS) theory of conventional superconductivity. At zero temperature, even an infinitesimally weak attraction ($a \rightarrow 0^-$) is sufficient to induce pairing among fermions near the Fermi surface. At finite temperature, however, a stronger attraction is required. By tuning the scattering length via a Feshbach resonance, one can increase the pairing temperature T^* , above which the system behaves as a weakly interacting Fermi gas.

On the opposite side of the resonance, where the scattering length is positive and large, fermions form tightly bound bosonic molecules. Above the critical temperature T_c , these molecules behave as a non-condensed Bose gas, while below T_c they undergo Bose–Einstein condensation, giving rise to a *molecular Bose–Einstein condensate* (mBEC). This regime is usually referred to as the *BEC limit* of fermionic superfluidity.

Despite their different microscopic constituents, the BCS and BEC regimes are continuously connected, since their ground-state wavefunctions share the same formal structure. The smooth crossover between these two limits defines the so-called *BEC-BCS crossover* [36]. In between the two extremes lies the *unitary Fermi gas* (UFG), where the scattering length diverges ($a \rightarrow \infty$) and the system reaches the strongest possible interactions allowed by quantum mechanics. In this regime, the pair size is comparable to the interparticle spacing, making the UFG a paradigmatic strongly correlated many-body system. At unitarity,

the scattering cross section is maximized and the only relevant length scale is set by the interparticle spacing, or equivalently by the Fermi wavevector k_F . As a consequence, the system becomes *universal*, in the sense that all its equilibrium and dynamical properties can be expressed in terms of the Fermi energy $E_F = \hbar^2 k_F^2 / (2m)$ and temperature T , without reference to microscopic details of the interatomic potential. The ground state at $T = 0$ is a strongly correlated superfluid, whose energy per particle is reduced with respect to that of a free Fermi gas by a universal factor ξ , known as the *Bertsch parameter*, with current best estimates around $\xi \simeq 0.37$.

At temperatures below the critical temperature T_c , fermions form a superfluid regardless of whether they are bound into molecules (BEC side) or weakly paired (BCS side). Between T_c and the pairing temperature T^* , fermions are paired but not condensed. This region, known as the *pseudogap regime*, is of particular interest because it exhibits features analogous to those of high- T_c superconductors.

In the BCS limit, $T^* \rightarrow T_c$ and no preformed pairs exist above T_c , as in conventional superconductors. Towards unitarity, however, T^* can be significantly larger than T_c , allowing for the existence of uncondensed pairs above the critical temperature. This intermediate regime remains an active subject of research in both ultracold atomic physics and condensed matter systems.

1.3 Harmonic potentials, BOX potentials and differences

Since the earliest studies involving ultracold atoms, optical potentials, and in particular harmonic potentials, have been widely employed for atomic trapping. One of the main reasons for their extensive use lies in the relative simplicity with which such potentials can be realized. In fact, the intensity of a laser beam is directly proportional to the potential experienced by the atoms. Consequently, a tightly focused laser beam can serve directly as an optical trap, which near the trap center can be approximated as harmonic to first order. Since we will explore both the bosonic and fermionic regimes, I will present here some characteristics of gases confined in a harmonic potential for comparison with the uniform case.

1.3.1 Harmonic potential

Let us consider a focused gaussian beam. Its intensity at the focal point can be written as:

$$I(x, y) = I_0 e^{-2 \frac{(x^2 + y^2)}{w_0^2}}, \quad (1.30)$$

where w_0 denotes the beam waist and x, y are the transverse coordinates with respect to the propagation direction z .

If the temperature of the atomic gas is sufficiently low such that only the lowest energy states of the gaussian potential are relevant—those localized near the central region of the beam—the gaussian potential can be approximated by a parabolic, such as harmonic, potential [38]. More precisely, this approximation is valid under the condition

$$\hbar\omega \ll U_0, \quad (1.31)$$

where U_0 is the trap depth and $\hbar\omega$ represents the level spacing of the harmonic oscillator. Under these conditions, the potential experienced by the atoms, in the isotropic case (such as with the same trapping frequency ω along all directions), can be written as:

$$V(r) = V_0 + \frac{1}{2}m\omega^2 r^2, \quad (1.32)$$

where the oscillator frequency is given by

$$\omega = \sqrt{\frac{4U_0}{mw_0^2}}. \quad (1.33)$$

With this potential, the Hamiltonian of the system reads:

$$H = \frac{p^2}{2m} + V(r). \quad (1.34)$$

The corresponding eigenstates and eigenvalues of the Schrödinger equation

$$H\psi(r) = E\psi(r) \quad (1.35)$$

are:

$$\psi_{nlm}(r, \theta, \phi) = R_{n,l}(r)Y_{l,m}(\theta, \phi), \quad E_N = \hbar\omega \left(N + \frac{3}{2} \right), \quad (1.36)$$

where $R_{n,l}(r)$ denotes the radial wavefunctions, that can be expressed in terms of generalized Laguerre polynomials, $Y_{l,m}(\theta, \phi)$ are the spherical harmonics (defined through associated Legendre polynomials), and N is the total quantum number, given by $N = n + l$.

We now turn to the study of the properties of a degenerate gas confined in a harmonic potential. In order to describe a Bose–Einstein condensate at $T = 0$, one has to solve the Gross–Pitaevskii equation:

$$i\hbar \frac{\partial \psi}{\partial t} = \left[-\frac{\hbar^2}{2m} \nabla^2 + V(\mathbf{r}) + g|\psi|^2 \right] \psi, \quad (1.37)$$

where $g = \frac{4\pi\hbar^2 a}{m}$ is the interaction strength and a denotes the s -wave scattering length. This equation does not admit a general analytical solution, and in most cases it must be solved numerically. However, two limiting cases allow for analytical insight: the non-interacting regime ($g \rightarrow 0$) and the strongly interacting regime ($g \rightarrow \infty$).

Let us first consider the non-interacting limit $g \rightarrow 0$. In this case, all atoms occupy the single-particle ground state of the harmonic potential. Consequently, the density profile of the gas reflects the squared modulus of the ground-state wavefunction. Since the ground state of the harmonic oscillator is gaussian, the condensate density acquires the same gaussian shape.

In contrast, in the strongly interacting regime $g \rightarrow \infty$, the kinetic term $-\frac{\hbar^2}{2m} \nabla^2$ in Eq. (1.37) can be neglected. This approximation is valid when holds the condition

$$\frac{Na}{a_{h.o.}} \gg 1 \quad (1.38)$$

where $a_{h.o.} = \sqrt{\frac{\hbar}{m\omega}}$ is the harmonic oscillator length. Under this assumption, one may look for a stationary solution of the form

$$\psi(r, t) = \psi(r)e^{i\frac{\mu t}{\hbar}}, \quad (1.39)$$

where μ is the chemical potential. Inserting this ansatz into Eq. (1.37), one obtains the algebraic equation

$$\mu = V(r) + gn(r), \quad (1.40)$$

with $n(r) = |\psi(r)|^2$ being the condensate density.

This relation immediately yields the density profile of the interacting condensate:

$$n(r) = \begin{cases} \frac{\mu - V(r)}{g}, & \text{if } \mu > V(r), \\ 0, & \text{otherwise.} \end{cases} \quad (1.41)$$

With reference to the harmonic potential in Eq. (1.32), the density profile can be conveniently expressed in the form

$$n(r) = \frac{\mu}{g} \left(1 - \frac{r^2}{R^2}\right), \quad \text{for } r \leq R, \quad (1.42)$$

where

$$R = \sqrt{\frac{2\mu}{m\omega^2}} \quad (1.43)$$

defines the so-called Thomas–Fermi radius. This quantity sets the characteristic spatial extent of the condensate and serves as a natural measure of its size in the presence of harmonic confinement.

Thus, in this limit the condensate density assumes an inverted-parabolic shape, which is a hallmark of Bose–Einstein condensates confined in harmonic traps.

Turning now to the fermionic case, let us first consider a non-interacting Fermi gas at $T = 0$. As previously discussed, such a system fills the N lowest-energy single-particle states. Within the local density approximation, in which the harmonic potential is treated as locally constant, and for the same potential considered in the bosonic case (Eq. (1.32)), the density profile reads:

$$n(r) = \frac{1}{6\pi^2} \left(\frac{2m}{\hbar^2} \left[E_F - \frac{1}{2}m\omega^2 r^2 \right] \right)^{3/2}, \quad \text{for } r \leq R_F, \quad (1.44)$$

where

$$R_F = \sqrt{\frac{2E_F}{m\omega^2}} \quad (1.45)$$

defines the Fermi radius.

The resulting density thus follows an inverted-parabolic profile raised to the power of $3/2$.

For the unitary Fermi gas, under the same approximations, the functional form of the density remains analogous to the ideal case, with the only modification being the inclusion of the Bertsch parameter ($\xi \approx 0.37$):

$$n(r) = \frac{1}{6\pi^2} \left(\frac{2m}{\hbar^2 \xi} \right)^{3/2} \left[E_F - \frac{1}{2}m\omega^2 r^2 \right]^{3/2}, \quad \text{for } r \leq R_F. \quad (1.46)$$

The presence of the external potential, together with the application of the Local Density Approximation, implies that the Fermi energy, and thus the Fermi temperature, varies from point to point within the system. As a consequence, if we consider real systems (with $T \neq 0$), different regions of the cloud are characterized by different local ratios of T/T_F , meaning that each point may exhibit distinct superfluid properties. This spatial inhomogeneity significantly complicates the analysis of measurements performed in such systems.

In conclusion, in harmonic confinement the density profile is always spatially dependent: for bosonic condensates it takes either gaussian or inverted-parabolic forms, while for degenerate fermions it follows a characteristic $(3/2)$ -power parabolic profile.

1.3.2 Box potential

The realization of a box potential, which will be discussed in detail in the next chapter, is more challenging than the harmonic case. In short, one possible method to implement such a potential is to use a blue-detuned laser beam to create repulsive walls that confine the gas within the box. If the walls are sufficiently steep and intense, the potential can be well approximated by infinitely hard boundaries.

At finite temperature ($T \neq 0$), the density profiles of bosonic and fermionic systems in a box potential have already been discussed in Sec. 1.1.1. Here, we restrict the analysis to the zero-temperature ($T = 0$) isotropic ($L_x = L_y = L_z = L$) case ($T = 0$), in direct analogy with the harmonic confinement.

We therefore consider a potential of the form given in Eq. (1.9). As in the harmonic case, all atoms occupy the single-particle ground state, so the density profile coincides with the squared modulus of that state. More explicitly, as described in Eq. (1.12), the ground-state wavefunction can be written as

$$\psi(x, y, z) = \left(\frac{2}{L}\right)^{3/2} \sin \frac{\pi x}{L} \sin \frac{\pi y}{L} \sin \frac{\pi z}{L}, \quad (1.47)$$

which gives rise to the density profile

$$n(x, y, z) = \frac{8N}{L^3} \sin^2 \frac{\pi x}{L} \sin^2 \frac{\pi y}{L} \sin^2 \frac{\pi z}{L}. \quad (1.48)$$

Thus, the density is not uniform inside the box.

When interactions are included, however, the situation changes. Analogously to the harmonic case, the density follows the shape of the confining potential and becomes uniform within the box:

$$n = \frac{\mu}{g}. \quad (1.49)$$

Consistency with the infinite potential barrier at the box boundaries requires that the condensate wavefunction vanishes at the walls. This occurs over a characteristic length scale given by the healing length,

$$\xi = \frac{\hbar}{\sqrt{2mgn}}, \quad (1.50)$$

which determines the distance over which the wavefunction recovers its bulk value near the boundaries.

Concerning the fermionic case, let us first consider a non-interacting Fermi gas. As before, the system occupies the N lowest-energy single-particle states. For large N , the superposition of many sinusoidal wavefunctions leads to an almost uniform density, given by

$$n = \frac{N}{V}, \quad (1.51)$$

with the characteristic presence of residual oscillations, also known as Friedel oscillations, which have a wavelength

$$\lambda_{osc} = \frac{\pi}{k_F} = \frac{1}{2}\lambda_F, \quad (1.52)$$

that is, half of the Fermi wavelength. A comparable length scale also characterizes the rise of the density from zero—at the infinitely repulsive walls of the box—towards its average value inside the system.

When interactions are included, these oscillations are suppressed, resulting in a more homogeneous density profile. Nevertheless, the characteristic length scale over which the density rises from zero to its bulk value remains of the same order.

1.3.3 Comparison Harmonic-Box potentials

To conclude, let us highlight some key differences between the harmonic and box potentials, beyond those already discussed in the previous sections. A first distinction concerns the single-particle energy spectra. In a harmonic potential, the level spacing is constant and equal to $\Delta E^{h.o.} = \hbar\omega$, whereas in the box potential it depends on the quantum number n :

$$\Delta E_n^{box} = E_{n+1}^{box} - E_n^{box} = \frac{\hbar^2 \pi^2}{2mL^2}(2n + 1). \quad (1.53)$$

Focusing on Bose-Einstein condensates, one finds that condensation in the harmonic trap occurs both in momentum and in position space, due to the localized shape of the ground-state wavefunction [12]. In contrast, in a box potential condensation manifests only in momentum space, since the real-space density remains nearly identical for the condensed and the thermal gas, being homogeneously distributed throughout the box. This makes the identification of condensation more challenging in the box geometry, and typically requires time-of-flight (TOF) measurements to reveal the macroscopic occupation of the zero-momentum state.

Another important difference emerges when studying the condensate fraction as a function of temperature. For the harmonic potential, the critical temperature and condensate fraction are given by

$$T_c = \frac{\hbar\omega}{k_B} \left(\frac{N}{\zeta(3)} \right)^{1/3}, \quad \frac{N_0}{N} = 1 - \left(\frac{T}{T_c} \right)^3, \quad (1.54)$$

where ζ denotes the Riemann zeta function.

For the uniform box potential, instead, one finds

$$T_c = \frac{2\pi\hbar^2}{mk_B} \left(\frac{n}{\zeta(3/2)} \right)^{2/3}, \quad \frac{N_0}{N} = 1 - \left(\frac{T}{T_c} \right)^{3/2}. \quad (1.55)$$

Thus, in the harmonic case the critical temperature scales with the total atom number N , whereas in the uniform box it instead depends on the density n . Moreover, the condensed fraction exhibits a different temperature dependence in the two cases.

Turning to Fermi gases, the different single-particle spectra (Eq. (1.12) and (1.36)) also lead to different definitions of the Fermi temperature [39]. In the harmonic trap, it reads

$$T_F = \frac{\hbar\omega}{k_B} (6N)^{1/3} , \quad (1.56)$$

whereas in the uniform box potential one finds

$$T_F = \frac{\hbar^2}{2mk_B} (6\pi^2n)^{2/3} . \quad (1.57)$$

Here, as for the bosonic case, the Fermi temperature depends on the atom number in the harmonic trap and on the density in the uniform box.

In summary, harmonic and box potentials not only determine different real-space density profiles but also profoundly affect the thermodynamic properties of both bosonic and fermionic quantum gases, from the onset of condensation to the scaling of characteristic temperatures.

Chapter 2

Box potential for Ultracold Li-6

In this chapter, the experimental sequence employed to cool and probe clouds of fermionic ${}^6\text{Li}$ atoms is described. The basic setup is only briefly outlined, while details on the experimental infrastructure are provided in reference [40]. The second part of the chapter focuses on the implementation — which represents the main objective of this thesis — of the uniform trap along the vertical direction, realized through the use of a digital micromirror device (DMD). First a simulation carried out to estimate the optical power required for confinement will be briefly discussed. Subsequently, the optical properties of the DMD will be discussed in detail, followed by a precise description of the vertical confinement optical setup, as constructed during this work. The chapter concludes with an analysis of techniques employed to render the box potential truly uniform, including compensation of the gravitational potential and elimination of any residual gradients in the system.

2.1 Experimental setup

The vacuum system, shown in Figure 2.1a, comprises an oven, a Zeeman slower and a science chamber. Inside the oven, a sample of artificially enriched ${}^6\text{Li}$ is heated to ~ 460 °C, to produce a significant vapour pressure and create an atomic beam, which is then collimated by a copper cold finger. This beam then passes through the Zeeman slower, which decelerates the atoms to around 60 m/s before they enter the science chamber.

The science chamber is a custom-made octagonal stainless-steel cell; on its vertical axis it has two large re-entrant view-ports allowing for a high-resolution imaging system. The pressure in this last segment is kept below 10^{-11} mBar in order to guarantee a sufficiently long lifetime of the atomic sample. The detailed description of the ultra-high vacuum system can be found in reference [40].

In the chamber the atoms that arrive from the Zeeman slower, are captured in a magneto-optical trap. A Magneto-Optical Trap (MOT) can be described as a hybrid device in which magnetic confinement and optical forces act together to cool and trap neutral atoms. The quadrupole magnetic field, generated by a pair of anti-Helmholtz coils (mounted inside the science chamber), produces a position-dependent Zeeman shift:

$$\Delta E(\mathbf{r}) = \mu_B g_F m_F B(\mathbf{r}), \quad (2.1)$$

which effectively breaks the spatial symmetry of the atomic resonance. When combined with circularly polarized, red-detuned laser beams, this mechanism ensures that atoms

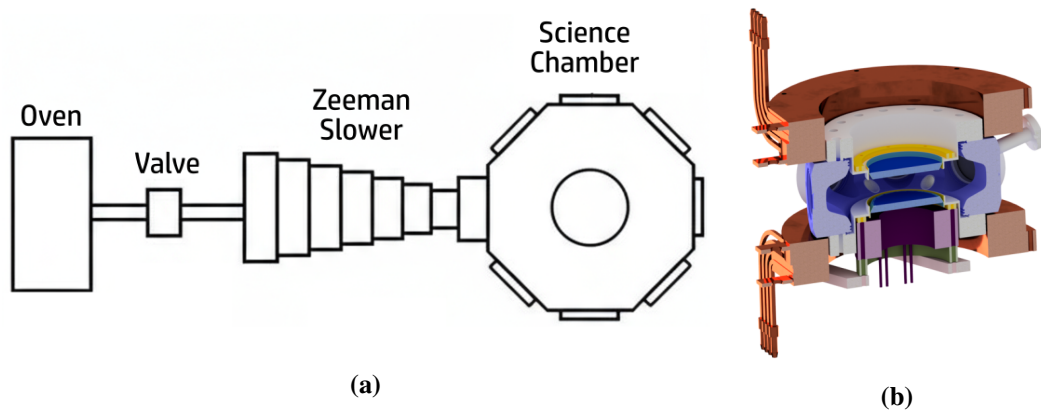


Figure 2.1. (a) Scheme of the ultra-high vacuum (UHV) apparatus used to isolate cold atoms from the background gas. Atoms are evaporated from an oven, travel through a valve, and are slowed down using a Zeeman slower before being collected in the science chamber where the experiments are performed. (b) Above and below the chamber, large coils in Helmholtz configuration (in orange) generate the homogeneous Feshbach magnetic field, while smaller concentric coils in anti-Helmholtz configuration (one is shown in purple) provide the quadrupole field for magneto-optical trapping (MOT).

moving away from the trap center preferentially absorb photons that push them back towards equilibrium. At the same time, the detuning of the light field provides a velocity-dependent damping force through Doppler cooling, which gradually removes kinetic energy from the ensemble. Together, these effects result in both a restoring force that confines the atoms and a dissipative force that cools them to microkelvin temperatures.

To realize the MOT, we employ a Toptica TA-Pro laser followed by a MOPA amplifier to increase the available optical power. The laser is tuned around 671 nm and locked to the $D2$ transition of ${}^6\text{Li}$ (see Fig. 2.2). Fine control of the laser frequency is achieved by means of a chain of acousto-optical modulators (AOMs), which provide both precise frequency shifts and fast intensity modulation.

After the MOT, atoms are loaded in an attractive optical dipole trap, made by two infrared lasers: the IPG, a 1073 nm multi-mode ytterbium fiber laser with a maximum output power of 200 W, and the Mephisto, a 1064 nm Nd:YAG laser with a maximum output power of 50 W. The intensity of both lasers is actively stabilized using AOMs controlled by a feedback loop.

As shown in Fig. 2.3, the two beams are focused at the center of the science chamber, crossing at an angle of 14° . Both beams have a waist of approximately $40 \mu\text{m}$. In the end, the optical trap produced by the intersection of these two lasers has a size of about $80 \mu\text{m}$.

Once the atoms are loaded into the ODT, evaporative cooling is performed. By gradually reducing the power of the trapping lasers the trap depth is lowered, allowing the most energetic atoms to escape. Through subsequent rethermalization of the remaining cloud, the atomic ensemble is cooled to temperatures on the order of a few tens of nanokelvin, with final samples containing about 10^5 atoms. The horizontal and vertical view of the atoms at this stage is shown in Figure 2.4 and 2.5 respectively.

As shown in Fig. 1.3, the Feshbach resonance between the $|1\rangle$ and $|3\rangle$ states occurs at lower magnetic fields. To explore the entire BEC–BCS crossover without encountering technical issues associated with driving excessively high currents through the coils, it is

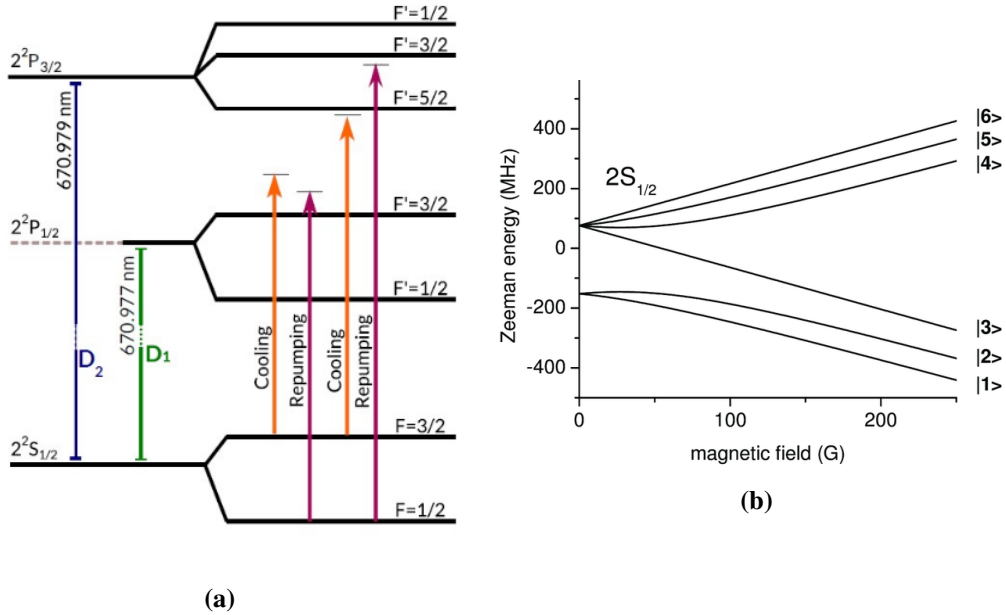


Figure 2.2. (a) The D1 and D2 line structure of ${}^6\text{Li}$ at zero magnetic field is shown. The D2 line is used for the MOT, imaging, and optical blasting, while the D1 line is employed for sub-Doppler cooling. The orange arrows represent the cooling transitions, whereas the purple arrow indicates the repumper, which brings atoms from the $2^2S_{1/2}$ $F = \frac{1}{2}$ state back to the $F = \frac{3}{2}$ state. (b) The splitting of the ground state is displayed. The bottom three energy states at high field, labeled as $|1\rangle$, $|2\rangle$, and $|3\rangle$, are the ones usually used in the experiments of the laboratory.

therefore convenient to work with a mixture of atoms in the $|1\rangle$ and $|3\rangle$ states.

However, after the preceding cooling and trapping processes, almost half of the atoms are populating the $|2\rangle$ state. To transfer these atoms efficiently into the desired $|3\rangle$ state, the evaporative cooling sequence is carried out in three steps:

- (1) First, evaporation is performed with the atoms in the $|1\rangle$ and $|2\rangle$ states at the Feshbach resonance of these two states, 832 G, so as to maximize interactions and promote rapid rethermalization.
- (2) Second, the magnetic field is lowered to 585 G, where the scattering lengths of the $|1\rangle$ - $|2\rangle$ and $|1\rangle$ - $|3\rangle$ interactions are equal. At this field, the $|2\rangle \rightarrow |3\rangle$ transition has a frequency of about 80 MHz; so radio-frequency pulse is applied to efficiently transfer the atoms from state $|2\rangle$ to $|3\rangle$.
- (3) Finally, after the transfer is complete, the magnetic field is ramped to the Feshbach resonance of the $|1\rangle$ - $|3\rangle$ pair, at 690 G, and the final stage of evaporative cooling is carried out under these conditions.

After the evaporative cooling stage, the gas is ready for experiments. To control various properties of the gas, or to create defects and excitations, a repulsive and controllable potential is employed. This potential is generated by a blue-detuned green laser beam whose intensity profile is shaped using a digital micromirror device (DMD). At the start of this thesis work, this DMD setup was already installed in the experimental system, and, as will be

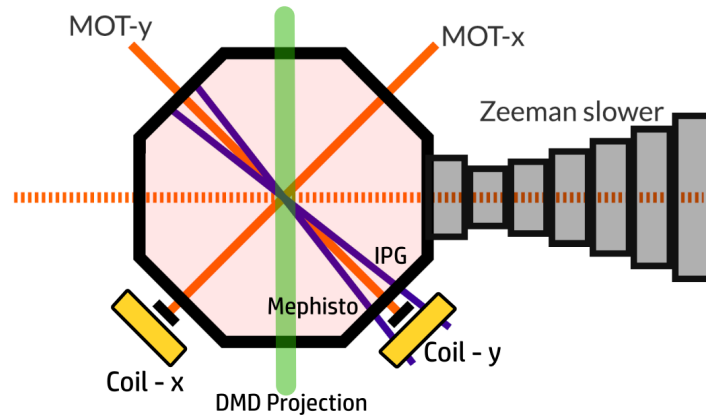


Figure 2.3. Sketch of the cooling and trapping lights in the science chamber view from below. The Zeeman slower beam is shown in dashed orange, the MOT beams along the x and y directions are in solid red. The two crossing optical dipole trap (ODT) beams, the IPG and the Mephisto, are depicted in violet. They intersect at an angle of 14° . In yellow, in correspondence of the beam dumps of the IPG and Mephisto beams, are shown the x and y coils, used for the compensation of horizontal gradients (see Sec. 2.5.3). In green is shown the propagation pattern of the light projected by the DMD and used for the vertical confinement, as will be described in Sec. 2.4.

discussed shortly, it is also used for horizontal confinement. The light for the DMD setup is provided by a Coherent Verdi V8 laser operating at 532 nm, and a high-numerical-aperture microscope objective, manufactured by Special Optics, is included in the system to enable high resolution and precise control of the repulsive potential. Further details of this setup can be found in [37].

In this chapter, we have cited the DMD setup already implemented in the system, which provides horizontal confinement of the ^6Li gas. Building on this, the focus of this thesis has been the creation and implementation of an analogue optical setup for vertical confinement. Both systems aim to produce a uniform potential for the atoms, achieved through the use of a DMD, thus enabling a homogeneous environment within the optical box potential. While the pre-existing DMD ensures horizontal confinement, the configuration presented here is dedicated to vertical confinement.

2.2 Imaging Systems

We extract information on the atomic sample, such as the number of atoms, temperature, and density distribution, by means of absorption imaging. Resonant light pulses are shone onto the cloud, and by recording the shadow cast by the atoms on a camera we acquire images of the sample. Two independent optical paths allow imaging both along the horizontal and vertical directions. To magnify and focus the atomic cloud onto the cameras, we employ a simple telescope for the horizontal direction and a high-resolution microscope objective for the vertical one.

Both imaging setups are overlapped with the corresponding DMD beam paths (horizontal and vertical). In this configuration, the detection axis of the imaging system is exactly aligned with the projection axis of the DMD light. This arrangement provides high precision and enhanced versatility of the system, enabling the generation of arbitrary optical landscapes.

For example, one can intentionally create localized defects or excite sound waves and vortices either parallel or perpendicular to the imaging axis, thereby maximizing the detectable signal from these excitations.

2.2.1 Absorption Imaging

To measure the density distribution of the atomic sample we employ absorption imaging. The presence of atoms is revealed by the shadow they cast in the recorded light pattern, which results from absorption of the probe beam. This behavior is described by the Lambert-Beer law [41]:

$$\frac{dI}{dz}(x, y) = -n(x, y) \sigma, \quad (2.2)$$

where I is the light intensity propagating along the z -direction through the atomic cloud, n is the local atomic density, and σ is the atom-photon interaction cross section. In general, σ depends on the probe intensity, making the absorption profile intensity-dependent.

In the low-intensity limit ($I \ll I_{\text{sat}}$), the cross section approaches its resonant value $\sigma \rightarrow \sigma_0$, and the absorption profile becomes independent of intensity. The resonant cross section is given by

$$\sigma_0 = \frac{3\lambda^2}{2\pi}. \quad (2.3)$$

However, when imaging optically dense clouds in this regime, very few photons are transmitted, leading to a poor signal-to-noise ratio (SNR). To increase the SNR, one can operate in the high-intensity regime, where saturation effects become relevant. In this case, the effective cross section modifies the Lambert-Beer relation as

$$\frac{dI}{dz}(x, y) = -n(x, y, z) \sigma_{\text{eff}} \frac{I}{1 + I/I_{\text{eff}}}, \quad (2.4)$$

where $\sigma_{\text{eff}} = \sigma_0/\alpha$ and $I_{\text{eff}} = \beta I_{\text{sat}}$ represent the effective cross section and effective saturation intensity, respectively. The deviations from the ideal two-level values, introduced by the multi-level structure of the atomic transition and by misalignment between the probe polarization and the quantization axis, are absorbed into the calibration factors α and β .

The measured shadow profile provides access to the local optical density (OD), obtained by integrating Eq.(2.4) along the imaging direction:

$$OD(x, y) = \sigma_{\text{eff}} n_{2D}(x, y) = -\ln\left(\frac{I_{\text{out}}}{I_{\text{in}}}\right) - \frac{I_{\text{out}} - I_{\text{in}}}{I_{\text{eff}}}, \quad (2.5)$$

where I_{in} and I_{out} are the incident and transmitted intensities, respectively. In the limit $I \ll I_{\text{eff}}$, the second term vanishes and one recovers the standard Lambert-Beer law.

The integrated column density of the atoms is then expressed as

$$n_{2D}(x, y) = -\frac{\alpha}{\sigma_0} \ln\left(\frac{I_{\text{out}}}{I_{\text{in}}}\right) - \frac{\alpha}{\beta\sigma_0} \frac{I_{\text{out}} - I_{\text{in}}}{I_{\text{eff}}}. \quad (2.6)$$

Reliable quantitative measurements of atomic density require the calibration of the coefficients α and β . More information about the calibration procedure can be found in [42, 43] The calibration procedure ensures that both α and β account for experimental imperfections

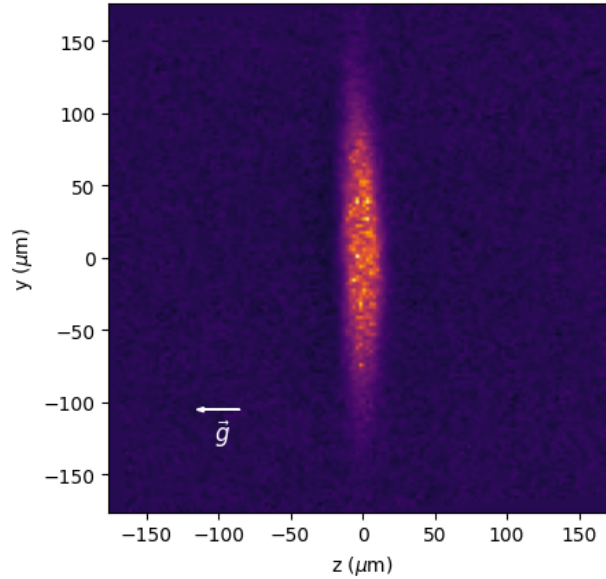


Figure 2.4. Typical absorption image acquired by the horizontal imaging system, showing the atomic cloud confined in a cigar-shaped optical dipole trap.

and deviations from the idealized two-level model, enabling accurate extraction of atomic densities from absorption images. In the experiment both high and low intensity imaging are used, respectively in the vertical and horizontal imaging.

2.2.2 Horizontal Imaging Setup

The horizontal imaging system consists of a telescope composed of two lenses with focal lengths $f_a = 150$ mm and $f_b = 1000$ mm, providing a total magnification of $M = \frac{f_b}{f_a} = 6.67$. The atomic image is projected onto an *Andor Ultra* camera operated in the Fast Kinetic Series (FKS) acquisition mode. This feature allows us to record a sequence of images with short time delays of order $200 \mu\text{s}$, at the expense of using only a restricted region of the CCD chip. This camera pixel has a size of $16 \mu\text{m} \times 16 \mu\text{m}$, corresponding to $2.4 \mu\text{m}$ on the atoms after accounting for the magnification factor.

Figure 2.4 presents a representative image of the gas trapped into the harmonic optical trap acquired using the horizontal *Andor* camera.

2.2.3 Vertical Imaging Setup

The vertical imaging system is based on a custom high-resolution, high-numerical-aperture microscope objective manufactured by Special Optics. The objective is corrected for both resonant light at $\lambda = 671$ nm and blue-detuned light at $\lambda = 532$ nm, enabling its use for high-resolution imaging as well as for projecting DMD-tailored optical potentials onto the atomic sample. The achievable resolution, defined as the minimum resolvable distance between two points in the object plane, is below $1 \mu\text{m}$ for both wavelengths. The imaging light is focused onto an *Andor iXon3 EMCCD* camera using an additional $f = 1000$ mm lens, resulting in a total magnification of $M = 21.8$. The camera pixels have a size of

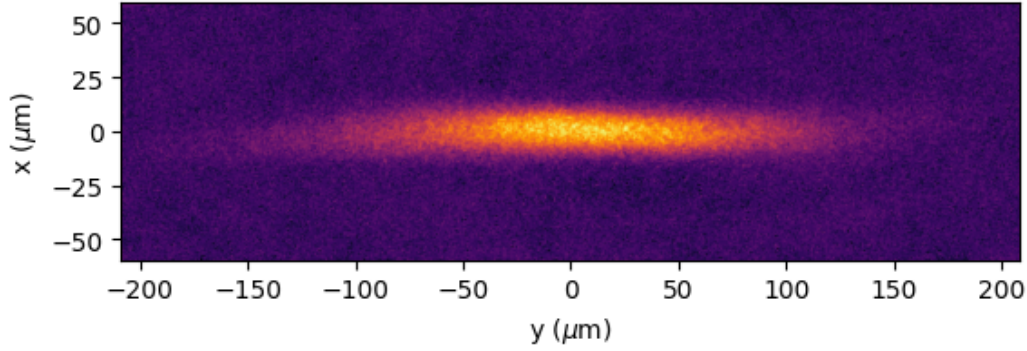


Figure 2.5. Typical absorption image acquired by the vertical imaging system, showing the atomic cloud confined in a cigar-shaped optical dipole trap. As one can see, in this case the resolution is greater than the horizontal case.

$13 \mu\text{m} \times 13 \mu\text{m}$. An example of an image of the atoms trapped into the harmonic optical trap, recorded with the vertical camera is shown in Fig. 2.5.

2.3 Design of the box potential

2.3.1 Simulation of the Box Optical Trap

To assess the feasibility of the trapping scheme and estimate the optical power required to generate a box potential, a Python simulation was developed. This simulation incorporates the properties of lithium gas, the characteristics of the gaussian beam incident on the DMD, and the desired dimensions of the box trap.

The gaussian beam impinging on the DMD is characterized by waists $w_y = w_z = 8 \text{ mm}$. The DMD reflection efficiency is assumed to be 50%. Combining these parameters with the relevant atomic properties of lithium – such as the atomic mass and optical response – enables calculation of the optical potential experienced by the atoms.

The repulsive optical potential is derived from Eq. (A.14). For sufficiently large laser detuning, the logarithmic term is expanded as $\ln(1+x) \simeq x$ for $x \ll 1$. Including contributions from both $D1$ and $D2$ transitions, the potential is given by

$$V_L(y, z) = \frac{3}{2} \pi c^2 (\alpha_1 + \alpha_2) I(y, z), \quad (2.7)$$

where the intensity profile of the beam at the waist is

$$I(y, z) = \frac{2P}{\pi w_y w_z} \exp\left(-\frac{2y^2}{w_y^2}\right) \exp\left(-\frac{2z^2}{w_z^2}\right), \quad (2.8)$$

and

$$\alpha_{1,2} = \frac{\Gamma_{D_{1,2}}}{\omega_{D_{1,2}}^3} \left(\frac{1}{\omega_{D_{1,2}} - \omega_L} + \frac{1}{\omega_{D_{1,2}} + \omega_L} \right), \quad (2.9)$$

with ω_L the laser frequency.

After characterizing the gaussian beam that will produce the potential, the beam is patterned by the DMD and set to zero in regions where light is reflected away from the

atoms. In this way we are able to simulate the light shaped by the DMD that arrives to the atoms. And in this way, we can define the effective potential $V_{\text{eff}}(y, z)$ experienced by the atoms. Based on this effective potential, the number of fermionic atoms that can be confined is estimated by considering the quantum statistics of a degenerate Fermi gas. More in details, knowing the geometry and the height of the trap, we can count the maximum number of atoms that we can trap, that corresponds, due to the Pauli principle, to the number of states available for the simulated trap. Indeed, for an ideal system at zero temperature ($T = 0$), the Fermi gas occupies its ground state, and all quantum states up to the Fermi energy E_F are filled. In a three-dimensional box potential, the number of fermionic atoms N that can be trapped at $T = 0$ within a box of volume V is

$$N = \frac{V}{6\pi^2} \left(\frac{2m}{\hbar^2} E_F \right)^{3/2}, \quad (2.10)$$

which follows from filling all available quantum states up to the Fermi energy.

Based on these simulations, the trapping energy required to confine on the order of 10^5 atoms - a typical reference value for the optical dipole trap - can be estimated. The results indicate that a total input power of 600 mW on the DMD (corresponding to 300 mW delivered to the atoms, accounting for 50% DMD reflection efficiency) enables trapping of approximately 9×10^4 atoms in a cubic box of side $50 \mu\text{m}$ (see Fig. 2.6). Based on these findings, optimal laser powers and components can be selected for the new system that will be discussed in Sec. 2.4.

Initially, the simulation is performed neglecting gravity. Gravity is subsequently included to quantify its influence on the trapping potential. The gravitational contribution is added as

$$V_g = mgz, \quad (2.11)$$

where m is the mass of lithium and g is the gravitational acceleration.

As shown in Figs. 2.6 and 2.7, gravity produces a significant modification of the trapping potential. In the presence of gravity, the gas can only be confined in a reduced region of the trap - approximately $18 \mu\text{m}$ in the simulated case - corresponding to a maximally trapped atom number of 1.5×10^4 . Accordingly, it will be necessary to implement a compensation strategy for the gravitational potential, as detailed in Sec. 2.5.2.

2.3.2 Digital Micromirror Device

A Digital Micromirror Device (DMD) is a reflective spatial light modulator (SLM) that controls the amplitude and phase of an incoming laser beam. Consequently, DMDs are ideal for generating arbitrary potentials for atoms, and they are, in fact, employed to construct the box potential, which is the objective of this thesis. In particular, two DMDs are employed: the first (V-7001) projects light vertically and has been implemented in previous years and widely used in the research group previous work[37]. The second DMD (V-9501), conversely, projects light horizontally towards the science chamber and was assembled as main part of this thesis project. This will serve as a case study to elucidate the operational mechanisms of DMDs.

The DMD employed in this thesis is composed by micrometric squared mirrors with a side length of $10.8 \mu\text{m}$, displaced in an array of 1920×1080 mirrors. These mirrors are programmable and they can assume two positions, which we can term "states". In both

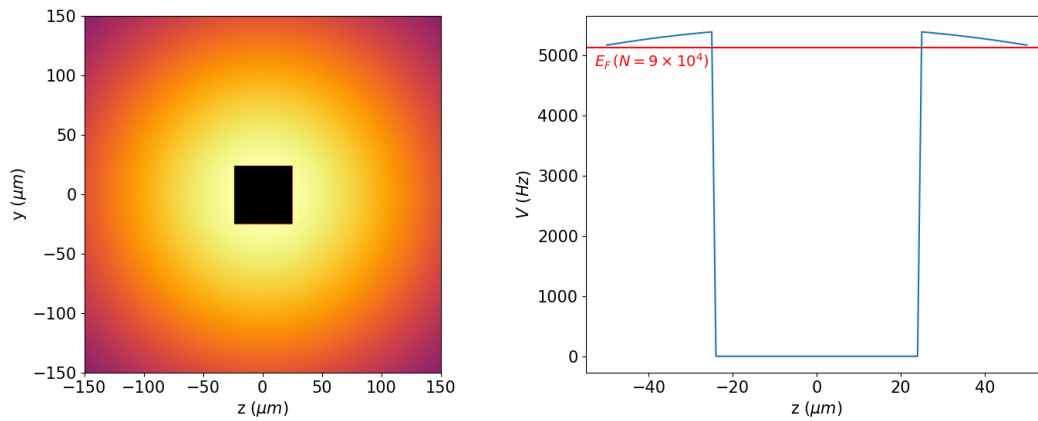


Figure 2.6. Results of the simulation of the box potential without including the gravitational potential with a laser power of 600 mW that corresponds at about 300 mW on the atoms. **On the left:** Lateral view of the repulsive potential generated by the green laser light and shaped into a square in the center using the DMD. **On the right:** 1D profile along the center (blue) together with the Fermi energy corresponding to 9×10^4 atoms (red). Since this Fermi energy approaches the depth of the potential well, this atom number can be taken as a reference for the maximum number of atoms that can be trapped in this potential.

cases, the mirror undergoes a rotation over its diagonal, by an angle of either -12° (ON state) or $+12^\circ$ (OFF state), thereby enabling the arbitrary modification of the incident light. In fact, as it will be demonstrated in the following section, the configuration is designed in such a manner that solely the mirrors in the ON state project light towards the optical set-up, while light from the OFF state is blocked.

The mounting support is tilted by an angle of about 45° , in such a way that the tilting axis of the mirrors is vertical (as the one in Fig.2.8a). This configuration is advantageous in obtaining a predominantly horizontal diffraction pattern and offers enhanced ease and safety when using that optical system. Given the tilt of the DMD mount, the image projected onto the DMD must be rotated by approximately the same angle in the opposite direction as we will see in section 2.5.1.

2.3.3 DMD optical properties

It is worth examining the behaviour of the DMD, a reflecting device, when subjected to illumination by a laser beam. In this thesis work, a 532 nm laser beam is used to illuminate the DMD, thereby realising a repulsive optical potential for ^6Li . As previously stated, each mirror of the DMD can be configured in one of two distinct states, tilted by an angle of $\pm 12^\circ$ from the DMD surface plane. It is evident that the light impinging on a mirror can be reflected in two different directions, depending on the tilt state of the mirror. In order to comprehend the complete optical behaviour of the device, it is essential to account for the fact that the DMD is composed of a series of micrometric mirrors. Therefore, the diffraction grating is comparable to a two-dimensional diffraction grating for the incoming light, as the dimensions of the mirror are commensurate with the wavelength of the laser beam. Consequently, the laser light impinging on the DMD surface is not merely reflected into one of the two directions determined by the tilt state of the mirrors, but rather into a multitude of diffraction orders. The distribution of laser power over a multitude of diffraction orders

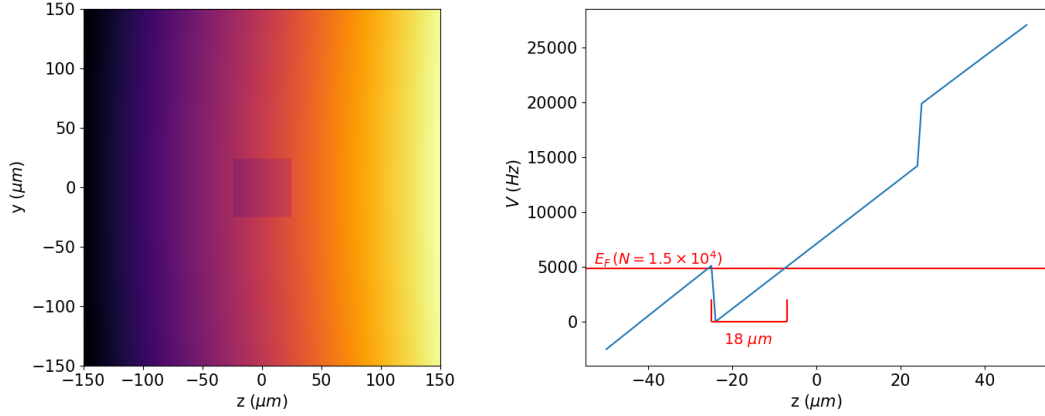


Figure 2.7. Results of the simulation of the box potential including the gravitational potential, using the same laser power as in Fig. 2.6. **On the left:** Unlike the case without gravity, the gaussian profile of the optical potential is no longer evident, indicating that the gravitational contribution dominates the total potential. **On the right:** Potential profile along the center. With the simulated laser power, the accessible region is limited to about $18 \mu\text{m}$, allowing for a maximum of approximately 1.5×10^4 trapped atoms.

is disadvantageous, as only a single direction is used and so the power distributed in the other orders is lost. Moreover, the strength of the reflected light in a specific direction can be optimised, identifying the so called blazing condition of the device.

To understand the blazing condition, we will now rapidly study the theory of diffraction of a 2D grating. In a diffraction grating, the laser light reflected from a single element of the grating interferes with light reflected from the surrounding ones. Given the orientation, the interference can be either constructive or destructive. Consequently, light is reflected in specific directions, which are designated as diffraction orders. The equation governing the diffraction grating problem is the following[41]:

$$m\lambda = d(\sin \theta_i + \sin \theta_m) , \quad (2.12)$$

where m is the diffraction order, λ is the wavelength of the impinging light, d is the spacing of the grating, θ_i is the incident angle and θ_m the reflection angle, respect to the DMD surface normal \hat{n}_s , as shown in figure 2.8c. We note so that angles that turn anti-clockwise with respect to the normal are positive while the ones that go clockwise are negative.

As soon as the DMD mirrors are tilted from the device surface plane, we have to consider this additional angle for the blazing condition. If, with the same reference of figure 2.8c, we consider the angles with respect to the mirrors normal \hat{n}_m , we can redefine the new incident angle: $\phi = \theta - \alpha$, where $\alpha = -12^\circ$ is the angle of the tilting of the micromirrors.

Fixed the incident angle of the laser beam, the device is said to be in a blazing state when the specular direction of reflection of the mirrors corresponds to a diffraction order m of the diffraction grating. Formally that means that the angles must satisfy this condition:

$$\theta_r = \theta_m , \text{ where } \theta_r = \phi_r - \alpha . \quad (2.13)$$

For the reflection rule, $\phi_i = -\phi_r$, that means:

$$\theta_m = 2\alpha - \theta_i , \quad (2.14)$$

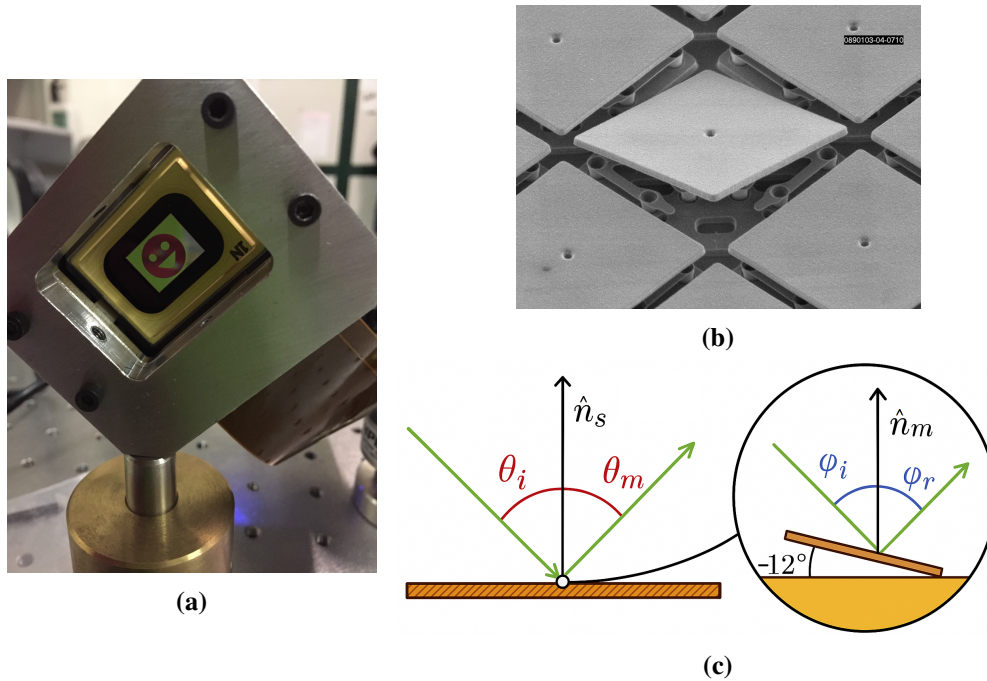


Figure 2.8. (a) Picture of the DMD (V-7001) mounted in its support with a smiling image loaded on board. Image taken from [44]. (b) Scanning Electron Microscope (SEM) image of the micromirror array of the DMD. Each mirror can be individually tilted around its axis, enabling precise modulation of the incident light in diffraction-based optical setups. Image taken from [45]. (c) Illustration of the adopted angles convention: θ angles are taken from the DMD surface normal \hat{n}_s , while ϕ angles are taken from the mirrors normal \hat{n}_m . The angle between \hat{n}_s and \hat{n}_m is equal to the rotation angle of the DMD mirror α that in this case, is considered equal to -12° .

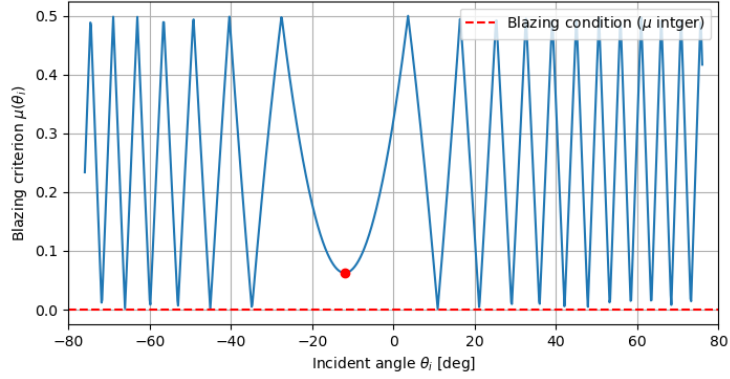


Figure 2.9. Blazing condition for the DMD. The plot shows the blazing criterion, μ , as a function of the incident angle, θ_i . The red dashed line indicates the ideal blazing condition (Eq. (2.15)), such as, when μ takes integer values. The red dot marks the experimental condition used in our setup, where the blazing criterion is not fully satisfied but it is locally minimized. Our configuration corresponds to the retro-reflection (or Littrow) configuration, in which the incident beams strike the tilted micromirrors perpendicularly and the outgoing beams are reflected back along the same path.

so, from the equation (2.12) we can define a function $\mu(\theta_i)$ that we can call the *Blazing criterion*, defined as:

$$\mu(\theta_i) = \left| \text{frac} \left(\frac{d}{\lambda} [\sin \theta_i + \sin(2\alpha - \theta_i)] \right) \right|, \quad (2.15)$$

where $\text{frac}(x) = x - [x]$ denotes the fractional part of x , the more μ is close to zero, the more the blazing condition is satisfied and the efficiency of the DMD reflection is good.

As will be discussed in more detail in the following section, our system is implemented in a retro-reflection geometry, which can be regarded as the analogue of the Littrow configuration for classical diffraction gratings. In this arrangement, the diffracted beam is directed back along a path that nearly coincides with the incident beam. For a DMD, this geometry ensures that the specular reflection imposed by the micromirrors, each tilted by -12° with respect to the device surface, is almost, though not exactly, consistent with the global grating equation. Consequently, as we can see in figure 2.9, the blazing parameter μ does not take an exact integer value but remains very close to zero.

Although perfect blazing is not achieved and diffraction into a single order is not fully maximized, this configuration represents an excellent compromise by providing relatively high diffraction efficiency while maintaining a simple optical setup.

Moreover, retro-reflection simplifies the focusing of the projected pattern: since the incident and reflected beams propagate nearly along the same axis, the imaging optics observe the DMD plane under highly symmetric conditions. This reduces angular aberrations, facilitates precise alignment, and results in a focus that is notably more robust against small misalignments. For these reasons, we adopt the retro-reflection configuration, whose final efficiency is on the order of 50%.

2.3.4 DMD control and feedback process

The DMDs used in the experiment are operated via a computer that controls their function through a program written in Python. This program relies on the ALP (Application Library Programming) software suite developed by ViALUX, which provides the ALP API and associated DLLs and the Python library ALP4lib [46]. The ALP library enables seamless control over both DMDs installed in the setup, supporting both static and dynamic operational modes. This flexibility allows the user to load sequences of images to the devices and update them dynamically, resulting in time-dependent optical potentials capable of creating moving barriers, shifting box walls, and other dynamic structures. Such dynamic control has been extensively employed in previous works of the research group, paving the way for diverse applications ranging from moving repulsive defects to generate vortices, sound and so on. Specifically for the horizontal DMD, the target of this thesis, the dynamic programming approach is used during the transfer phase, when atoms are loaded from the harmonic ODT into the box potential generated by the DMDs. The use of Python, together with the ALP4lib module, permits intuitive programming of these sequences. The workflow generally involves generating the required image sequence in Python, allocating the onboard memory in the DMD via the ALP API, and uploading the sequence. The image update rate and overall timing are precisely controlled by setting an appropriate number of TTL signals in the experiment control program. For the horizontal DMD, the nominal switching rate is approximately 18 kHz, corresponding to a minimum picture time of about $56 \mu\text{s}$. This switching time is significantly shorter than the typical timescales of the physical dynamics we are interested in controlling, making the device well-suited for generating dynamic optical potentials in ultracold atom experiments. A characteristic timescale that can be used as a reference for the dynamics of a Fermi system is the Fermi time,

$$t_F = \frac{\hbar}{E_F}, \quad (2.16)$$

which defines the timescale over which the quantum properties of the gas become relevant. For a typical system produced with this experimental setup, the Fermi time is on the order of $t_F \sim 300 \mu\text{s} > 56 \mu\text{s}$. This comparison indicates that the DMD switching is sufficiently fast to address the dynamics of the Fermi gas, though not entirely negligible relative to t_F .

Furthermore, by employing a Python-written program that operates with a CMOS camera integrated into the setup for the vertical DMD (and adaptable to the horizontal one), it is possible to optimize the arrangement of the mirrors — either switched ON or OFF — in order to obtain an arbitrary optical potential in both shape and height on the atoms. For example, this optimization can be used to eliminate the gaussian profile of the laser beam to create a more uniform potential for the atoms, or alternatively to generate potential gradients or potentials with variable heights.

The program implements a feedback loop algorithm in which the image measured by the camera is compared with the target image set in the software. The difference between the two images is then evaluated, and through the algorithm the error is propagated to the neighboring pixels, which correspond to the adjacent mirrors of the DMD. By iteratively applying this procedure, mirror configurations are generated that reproduce the desired potential landscapes. A detailed explanation of how this process works can be found in thesis [44], while Figure 2.10b shows an example of a box with an internal potential gradient, obtained through the feedback process.

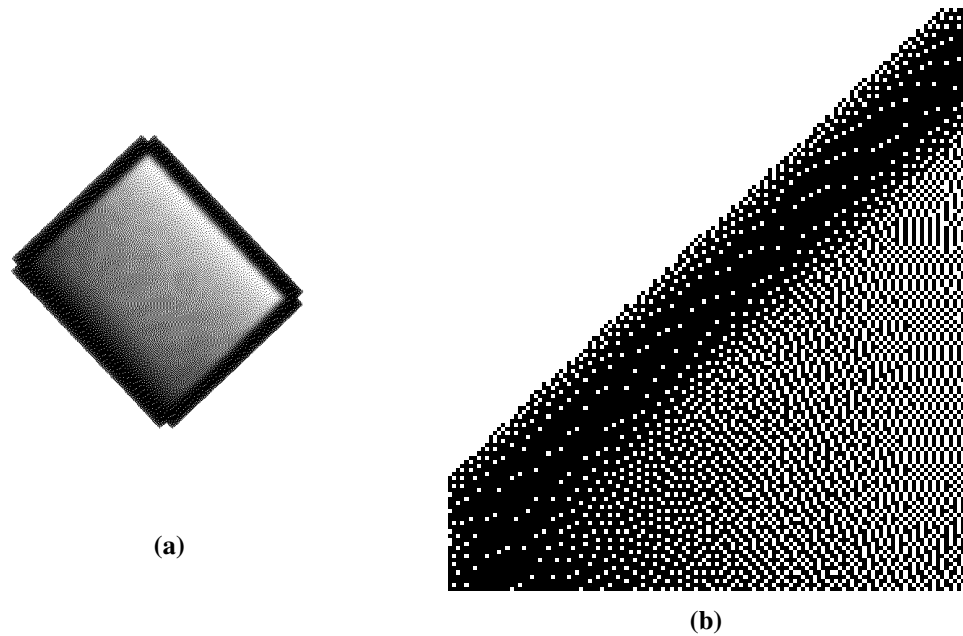


Figure 2.10. (a) Example of a box with a gradient inside it, generated using the feedback system. The program loads a grayscale image as the target and, by iteratively applying a feedback loop, produces the displayed result. As shown in detail in panel (b), the gradient is realized by varying the density of fully black pixels. This is necessary because the DMD mirrors can only be in one of two possible states, ON or OFF, so the image uploaded to the DMD must consist exclusively of black or white pixels.

2.4 Optical set up for box confinement

In this section, the experimental setup developed during this thesis work is described in detail, starting from the characterization of the laser used to generate the green light for repulsive confinement, passing to the description of the two optical setups that have been developed during this thesis: the *light preparation* and the *DMD-projecting* setup.

2.4.1 The Laser

The laser used to create the repulsive trap for vertical box confinement is an *AZURLIGHT System* laser with a wavelength of 532 nm and a nominal maximum output power of 10 W. The laser operates in a single transverse mode (TEM_{00}) with a narrow linewidth of less than 20 kHz, ensuring excellent beam quality and coherence. Moreover, the laser beam exits vertically polarized and nearly collimated, with an output diameter of approximately 1 mm.

According to the manufacturer guidelines, the laser should be operated within a power range of 10% to 100% of its maximum output. Given the relatively low power required for trapping in our system (as discussed in the simulation in Sec. 2.3.1), we set the operating power between 1.5 and 2 W. This choice provides sufficient trap depth for effective vertical confinement while minimizing thermal effects on the optics components and potential beam distortions.

Before building the setup for the DMD, we characterize the laser output power as a function of the setpoint power set on the laser itself, in order to verify its validity. A preliminary measurement of this quantity is provided by the manufacturer. In addition, other similar measurements had already been carried out previously using a powermeter from "Ophir", model "Nova II", the same used for the new ones. The results of these measurements are shown in Figure 2.11a. From the figure, we can see that the trend is very linear. However, we can also see that the power set in the laser and the output power are not the same and differ from the values given by the manufacturer. This is anyway not a problem for the system because the power that from the laser goes to the science chamber is fine controlled in other ways (see Sec. 2.4).

If we perform a linear fit on the data, we find that we can approximate the output power (P_{out}) as a function of the set power (P_{set}) very accurately, as follows:

$$P_{out} = 1.26 \times P_{set} . \quad (2.17)$$

From this point onward, as well as for the previously mentioned values (typically 1.5–2 W set on the laser), we refer to the *setpoint power* of the laser. The actual output power may therefore vary due to system and component characteristics, resulting in an effective output ranging approximately from 1.9 to 2.5 W.

Another useful analysis is the characterization of the output power as a function of the internal pump current of the laser. As shown in Fig. 2.11b, our measurements follow the same trend across all data sets and are in good agreement with the behavior reported in the datasheet.

2.4.2 Optical set up

The optical system developed for the realization of the vertical part of the box potential, the aim of this thesis, can be divided into two main sections. The first section, the *light*

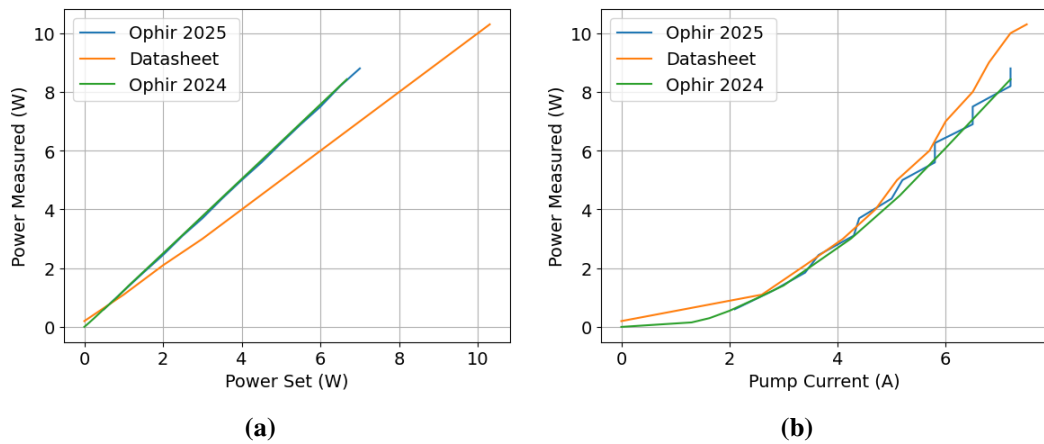


Figure 2.11. (a) Comparison between the laser power set on the controller and the power measured. The measurements were carried out with the Ophir powermeter, one in 2024 (in green) and the other one year later (in blue). The two measurements are shown together with the reference curve provided in the datasheet (orange). The results indicate that the actual output power is consistently higher than the set value by a factor of approximately 1.26. Moreover, the comparison of Ophir measurements taken one year apart demonstrates excellent stability of the laser output over time. (b) Output power, measured with the same powermeters of figure (a), as a function of pump current, indicated on the control screen of the laser. The results are compared with the manufacturer datasheet values (orange). The measurements from different powermeters are in good agreement, while the datasheet reports slightly higher output power.

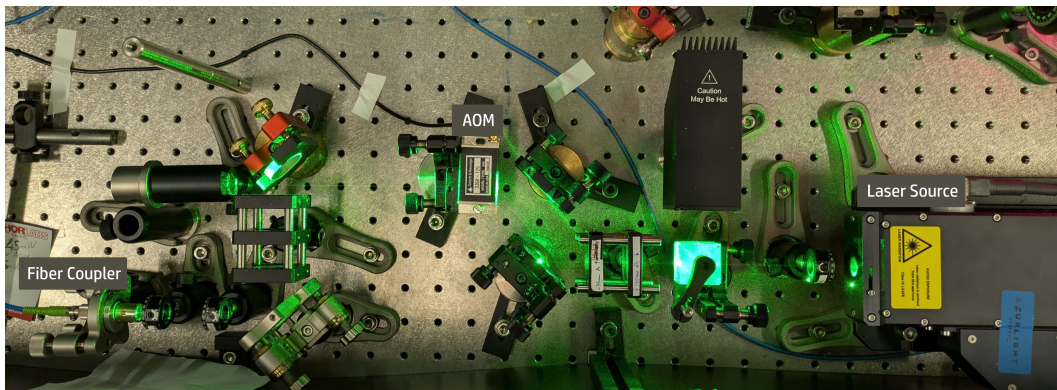


Figure 2.12. Photo of the *light preparation setup*, the first part of the setup realized during this thesis work. In this stage, the laser output beam is cleaned and stabilized in both power and polarization before being coupled into a fiber and transmitted to the second section of the setup.

preparation setup, is devoted to beam conditioning and cleaning, ensuring high-quality control of the laser before use. Instead, the second section, the *DMD-projecting setup*, involves the DMD and delivers the light into the science chamber, directly onto the atoms, thus enabling the actual creation of the box potential.

A photo of the light preparation setup is reported in figure 2.12. Starting from the laser output on the right, the beam, that exits vertically polarized, is split in two parts with the use of a half-wave plate ($\lambda/2$) followed by a high-power polarizing beam splitter cube. The transmitted beam continues through the optical setup, whereas the reflected portion is safely absorbed by a high-power beam dump. This configuration allows the laser to operate at a relatively high power - within the range specified by the manufacturer - while preventing excessive power from entering the setup, which could otherwise damage some optical components.

After the output power is divided, the beam size is reduced using a telescope with a magnification factor of 0.75. The telescope is composed of a first lens with focal length $f_1 = 100$ mm and a second, diverging lens with $f_2 = -75$ mm. The use of a diverging lens makes it possible to compact the optical setup significantly. Indeed, for a telescope configuration the distance between the two lenses is given by $f_1 + f_2$, which in this case amounts to only 25 mm. For comparison, an analogous telescope realized with two converging lenses of 100 mm and 75 mm focal length would require a separation of 175 mm.

The telescope is designed so that the beam diameter matches the optimal value required for the operation of an Acousto-Optic Modulator (*AOM, Gooch & Housego 3350-125*). The two mirrors after the telescope are used to align the beam on the AOM.

The AOM exploits the interaction between light and sound waves inside an optical crystal. A piezoelectric transducer, driven at radio frequencies (RF), generates an acoustic wave that propagates through the crystal, producing a periodic modulation of the refractive index. This modulation acts as a diffraction grating, whose spacing is determined by the acoustic wavelength. When the laser beam passes through the crystal, it is diffracted into several orders. The first-order diffracted beam is selected to propagate through the optical path, while the undiffracted zeroth-order beam is blocked by an homemade beam dump. Since the intensity of the first-order beam can be controlled directly by adjusting the RF drive power (this will be specified in the description of the second part of the setup), the AOM provides fast and precise control over the optical power.

The diffracted mode, once selected by reflection from the edge of a mirror, is directed through a second telescope with a magnifying factor of 0.5. This telescope is realized by a pair of lenses, a converging lens with focal length $f_3 = 100$ mm and a diverging lens with $f_4 = -50$ mm. In this way, the beam size is adjusted to match the mode field diameter required by the collimator *Schafter Kirchhoff 60FC* for efficient fiber coupling.

The beam is then coupled into an *NKT-photonics aeroGUIDE-PM-10* polarization-maintaining fiber. In order for the fiber to preserve the polarization state, the input polarization must first be properly aligned. For this purpose, a set of waveplates – a quarter-wave plate ($\lambda/4$) followed by a half-wave plate ($\lambda/2$) – is inserted before the fiber input, allowing fine control and stabilization of the polarization state.

It is worth noting that the polarization-maintaining fiber requires a well-defined linear polarization at its input, aligned along one of its birefringent axes. For this reason, the order of the two waveplates is crucial. The quarter-wave plate, placed first, compensates for any residual ellipticity of the input beam, converting it into a purely linear polarization. The subsequent half-wave plate then rotates this linear polarization, enabling precise alignment

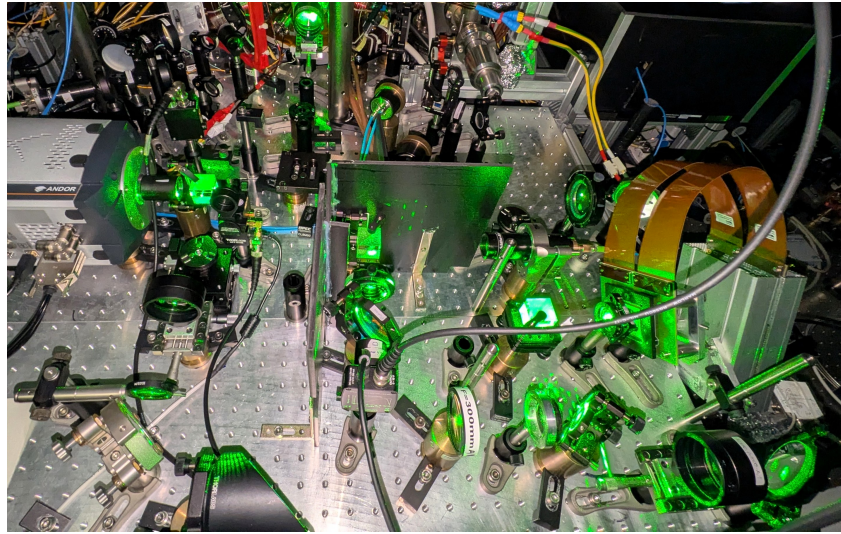


Figure 2.13. Photo of the *DMD-projecting setup*, the second part of the setup developed during this thesis. In this stage, the laser beam emerging from the optical fiber is power-stabilized, its spatial profile is shaped by the DMD, and subsequently directed onto the atoms.

with the slow or fast axis of the fiber. If the order were reversed, the half-wave plate would only rotate the initial polarization state, while the quarter-wave plate would introduce an uncontrollable ellipticity, preventing the correct coupling into the fiber. The fiber delivers the gaussian beam to the optical table of the science chamber, ensuring stable mode quality and well-defined polarization for the second stage of the optical system.

A photograph of the *DMD-projecting setup* is shown in Figure 2.13, while a diagram of the setup, for easier understanding, is shown in image 2.14. The laser beam exits the fiber through a collimator *Schafter Kirchhoff 60FC-Q*, which already makes the beam size suited for the dimensions of the DMD (with a beam diameter of approximately 1.6 cm). Thanks to the properties of the polarization-maintaining fiber and proper alignment of the collimator, the beam emerges with an almost perfectly vertical polarization. This polarization is further purified by reflection from a polarizing cube, which transmits the majority of exiting power. The beam polarization is then rotated by 90° using a half-wave plate and directed, via a dichroic mirror, toward a second polarizing cube. After passing through the cube and a quarter-wave plate placed immediately afterwards, the beam impinges on the DMD, where it is retro-reflected and arbitrarily shaped. Upon passing again through the quarter-wave plate, the beam is reflected by the polarizing cube and continues along the optical setup.

A photodiode, *Thorlabs PDA36A2*, is positioned behind the dichroic mirror to collect the small fraction of light transmitted through it. In this setup, the dichroic mirror is not used to reflect one frequency and transmit another; rather, it serves as an optical element whose loss can be readily measured by the photodiode itself. The photodiode signal is utilized to stabilize the output power from the fiber. Specifically, this signal is fed into a PID controller, *SRS SIM960* (Proportional–Integral–Derivative), which regulates the AOM located in the light preparation setup by adjusting the amplitude of the radio-frequency signal driving the AOM. This feedback loop allows the system to maintain a stable fiber output power. This approach enables also dynamic control of the laser power at the fiber output, and consequently on the DMD. This makes it possible to generate tailored power

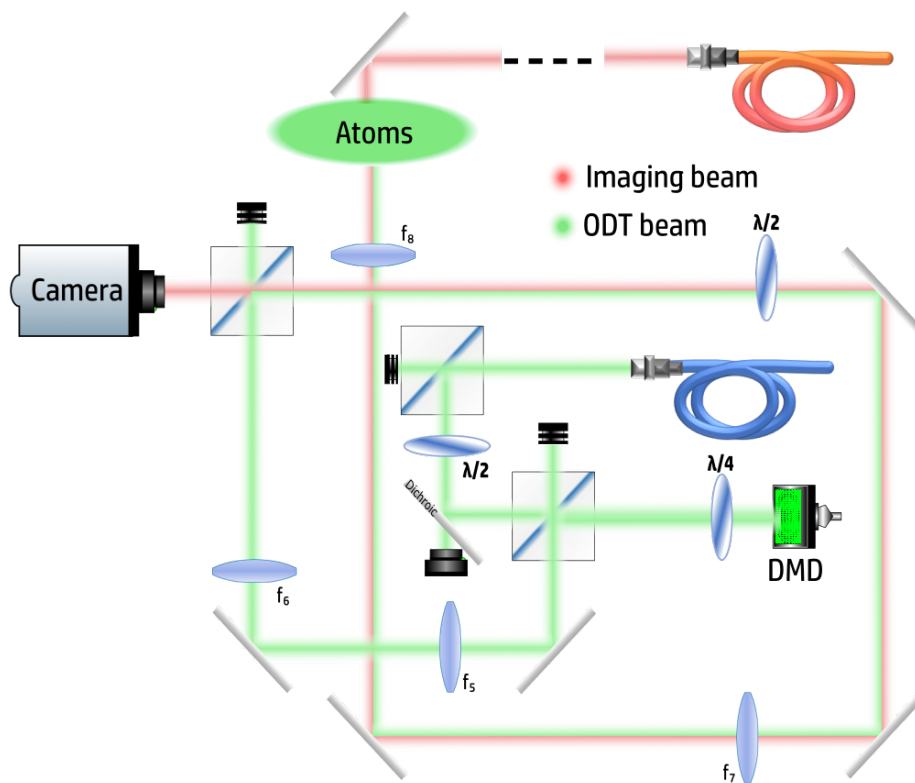


Figure 2.14. Scheme of the *DMD-projecting setup*. As illustrated in the schematic, part of the setup is shared with the horizontal imaging system. This feature, as discussed in Section 2.5.1, is extensively exploited for aligning the light from the DMD with respect to the atomic cloud.

ramps for gradual beam switching on or attenuation, as required.

After being reflected by the cube, the beam passes through a first telescope composed of two converging lenses with focal lengths of $f_5 = 300$ mm and $f_6 = 75$ mm. The first lens is placed at a distance f_5 from the DMD plane. This arrangement ensures not only the collimation of the beam but also the imaging of the DMD, which must be sharply focused onto the atoms. By placing the first lens at a distance equal to its focal length from the object, and the second at $f_5 + f_6$ from the first, the image is re-imaged at a distance f_6 from the second lens.

After the first telescope, the beam is reflected by a polarizing cube and then passes through a second telescope, this time consisting of two lenses with focal lengths $f_7 = 1000$ mm and $f_8 = 150$ mm. The first lens of this second telescope is positioned at a distance $f_6 + f_7$ from the second lens of the first telescope. In this way, the image of the DMD is refocused at $f_8 = 150$ mm from the last lens, precisely at the position of the atoms.

Thanks to the two telescopes, the image projected onto the DMD reaches the atoms demagnified by a factor equal to

$$M = \frac{f_6}{f_5} \times \frac{f_8}{f_7} = \frac{75}{300} \times \frac{150}{1000} \simeq \frac{1}{26.67}, \quad (2.18)$$

This means that the dimensions of the DMD are reduced by a factor of 26.67. Consequently, each micromirror of the DMD, with a size of approximately $10.8 \mu\text{m}$, will correspond to a length of about $0.4 \mu\text{m}$ on the atoms.

The setup also includes mirrors, which are needed to direct the beam to the atoms, and a half-wave plate ($\lambda/2$) designed for a wavelength of 670 nm. The presence of this wave plate is related to the fact that part of the second section of the setup developed in this thesis is shared with the imaging system, which propagates in the opposite direction. In addition, the setup includes irises that serve to block unwanted diffraction orders generated by the DMD and to facilitate alignment with the atomic sample by exploiting the partial overlap between the projection and imaging paths, as explained in Sec 2.5.1. Moreover, the first iris also blocks a portion of the high-frequency Fourier components. This is done to ensure that the Fourier components reaching the atoms are immediately filtered, enabling a direct diagnosis of the actual potential experienced by the atoms. This configuration also guarantees that the feedback process operates using the same available Fourier components, preserving consistency between the measured and applied potentials (see Sec. 2.3.4).

2.5 Making the Box Potential Uniform

2.5.1 Aligning, focusing and fine tuning the DMD setup

Regarding the alignment of the DMD setup, the irises mentioned in Sec. 2.4 were employed. More precisely, since part of the DMD projection setup is shared with the horizontal imaging system, the irises positioned along the optical path are initially aligned with the atoms trapped in the ODT. This alignment ensures that a fully closed iris corresponds exactly to the position of the atoms. By subsequently aligning the beam reflected from the DMD to these irises, an initial coarse alignment of the beam on the atoms is achieved. Consequently, the trapped gas in the ODT is effectively intersected by the green light of the new setup. Once a signal from the potential on the atoms is detected, the final fine alignment of the setup on the atoms can proceed. By aligning the center of the DMD with the center of the

cigar-shaped atomic cloud in the optical dipole trap, one ensures that the atoms experience the maximum incident power from the DMD, which is available at its center.

To have the best precision in the control and the best resolution as possible for the system is necessary to properly focus the horizontal setup, both for the imaging and for the DMD. The focusing procedure for the horizontal setup proceeds as follows:

- (1) First, the horizontal imaging system is brought into focus. This is achieved by creating a cut in the atomic cloud confined in the ODT using the vertical DMD. Two closely spaced vertical light sheets are projected so that the atomic cloud is sliced, leaving only a narrow strip of atoms inside the region between the two sheets. By translating the lens f_8 (see Section 2.4) and minimizing the width of the remaining atomic strip, measured by the horizontal camera, the optimal position of this lens — and hence the best focus of the horizontal imaging system — is determined.
- (2) Finally, once the imaging system is properly focused—so that the optical path of the DMD system, which is shared with the imaging path, is fixed—the DMD itself is brought into focus. To this end, the atoms are loaded into a box potential that is wide horizontally but narrow vertically. In addition to the horizontal DMD light sheets required for trapping, two vertical lines are projected to cut the gas. The lens f_6 is then translated (see Sec. 2.4), and the atomic distribution is imaged with the vertical camera. As shown in Fig. 2.15, when the DMD is correctly focused the projected vertical lines produce sharp, well-defined cuts; if the lens position is not optimal, these regions appear broadened. By optimizing the sharpness of these lines, the DMD focus can be precisely adjusted. The system is aligned so that the two DMDs are perfectly overlapped when both are focused on the atomic plane. As shown in the figure, translating lens f_6 also causes a shift of the projected lines with respect to the box (by about $10\ \mu\text{m}$), indicating that the lens is not perfectly perpendicular to the laser beam. Because the light travels more than one meter after this lens before reaching the atoms, achieving perfect perpendicularity is extremely challenging. For this reason, during the alignment and focusing procedure, the lens is slightly rotated to minimize the residual displacement.

Once the system is optimally focused, the atoms can be loaded into the box potential by simply projecting a vertical square and two horizontal light sheets. However, in this configuration, atoms that lie outside the regions defined by the DMD light are inevitably lost, resulting in a poor loading efficiency of the box potential. To overcome this limitation and capture as many atoms as possible, a dynamic loading protocol can be implemented by taking advantage of the dynamical control offered by the two DMDs. Starting from a very large square on the vertical DMD and two widely spaced light sheets on the horizontal DMD, all dimensions are then gradually reduced. Because the initial size of the projected box exceeds the spatial extent of the atomic cloud in the ODT, a large fraction of atoms can be transferred into the final box trap by gradually reducing the projected dimensions.

2.5.2 Gravity compensation

Once the entire system has been set and properly aligned, the signal measured by the horizontal imaging system is as shown in figure 2.17a.

As can be seen, the atoms do not occupy the entire box potential but are instead compressed toward the bottom of the trap and unbalanced to one side. The compression

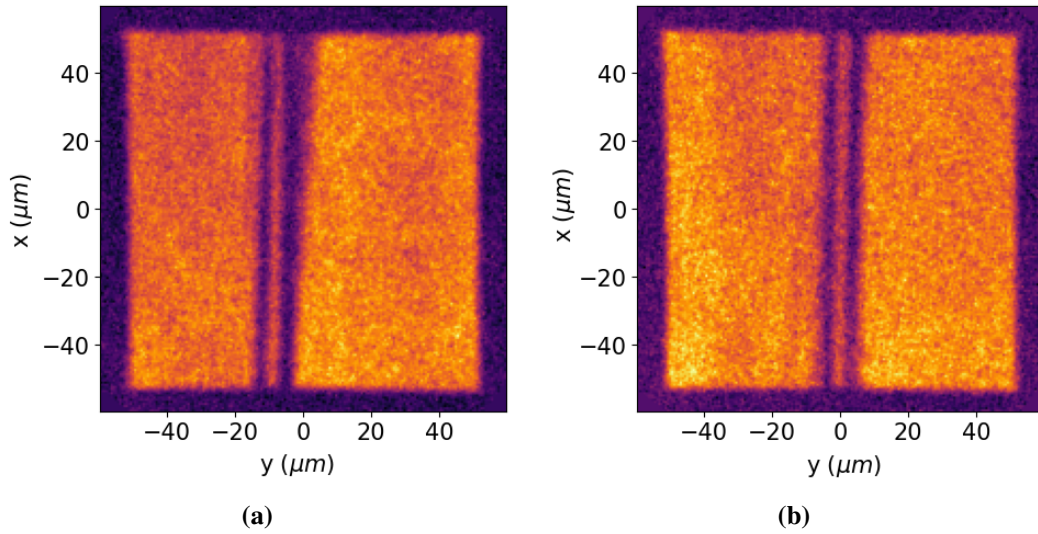


Figure 2.15. Vertical absorption images of atomic gases in the UFG regime, confined in a $100 \times 100 \times 25 \mu\text{m}^3$ box potential, with two additional vertical light sheets projected by the DMD to cut the atomic cloud. **(a)** shows the effect of the DMD light being out of focus: the cuts are broadened and non-uniform, particularly at the top of the image, due to vertical divergence of the projected beam, resulting in imperfect atomic separation. **(b)** displays the result after optimal focus is achieved, yielding sharp, uniform light sheets and well-defined atomic cuts, demonstrating precise optical control.

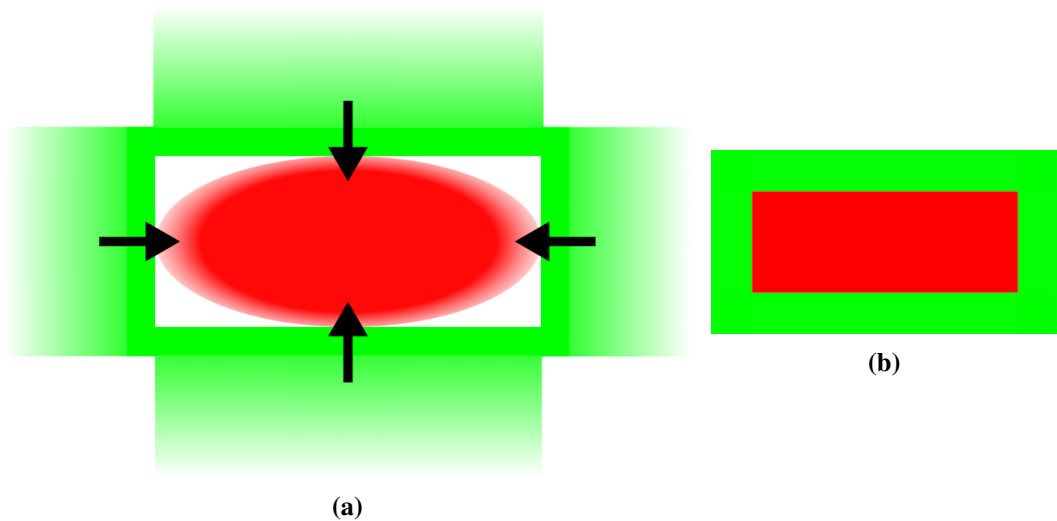


Figure 2.16. Schematic representation of the atomic cloud squeezing process, designed to maximize the loading efficiency into the box potential. **(a)** Initially, the DMD projects light in such a way that it does not intersect the atomic cloud. Subsequently, dynamic control of the DMD is used to gradually squeeze the optical potential down to the final box dimensions **(b)**. If the box potential were projected at its final size from the beginning, only a small fraction of atoms would fall inside, resulting in minimal loading efficiency.

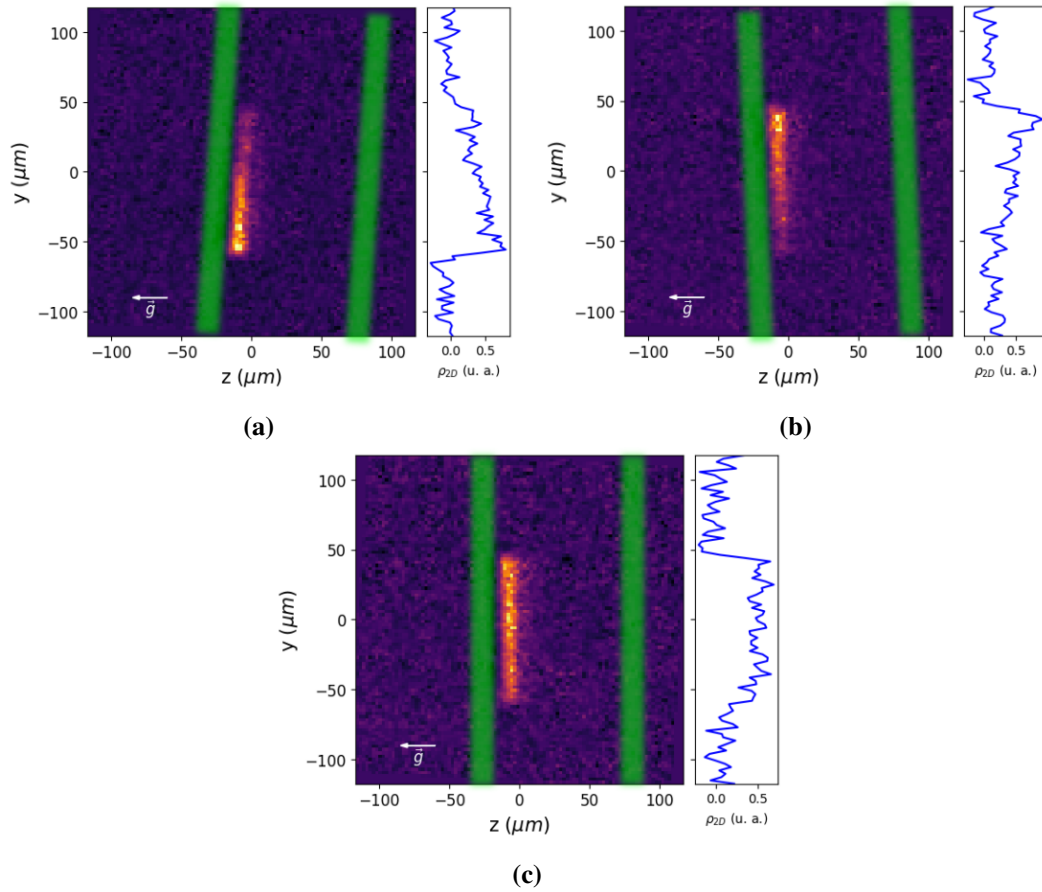


Figure 2.17. Images of the gas in the BEC regime, taken with the horizontal imaging system during the alignment procedure of the rotation angle of the vertical confinement of the box. **(a, b)** show that, by rotating this angle, the atomic cloud—being compressed against the bottom of the box—will accumulate on one side if the box is not perfectly horizontal. As a result, the gas density increases on one side of the box. **(c)** shows that, once the correct rotation angle of the light sheets is found, the gas density becomes horizontally uniform.

occurs because the atoms are naturally pulled downward by gravity, which, in the absence of other potentials, becomes the dominant contribution. The lateral unbalance also indicates that the box projected by the DMD is not perfectly horizontal. In general, gravity is a typical and specific concern for uniform 3D potentials. In contrast, for harmonic potentials, gravity does not pose a significant problem: adding a linear potential such as gravity to a harmonic trap simply results in a shifted harmonic potential. Thus, apart from a slight realignment, gravity does not introduce any substantial complications in this configuration.

Thanks to the great versatility of the DMD, the imbalance of the system can be easily compensated by slightly rotating the orientation angle of the box image on the DMD. As explained in Section 2.4, the DMD is mounted on a stage rotated by approximately 45° , which means that the image of the line projecting the light sheet necessary for confinement must be rotated by the same angle in the opposite direction with the respect to the DMD axes. By adjusting this angle, the imbalance can be effectively corrected, ensuring that the resulting box is optimally horizontal. As shown in Fig. 2.17c, the gas is approximately balanced along the horizontal direction; however, it remains compressed at the bottom of the box. In fact, the projected box on the atoms measures about $100 \mu\text{m}$, while the gas exhibits a vertical size of about $18 \mu\text{m}$, in perfect agreement with the simulation presented in Section 2.3.1.

To compensate for gravity, we must therefore create a linear potential equal in magnitude and opposite in direction to the gravitational one. There are several possible strategies to achieve this, among which is the use of linear intensity gradients generated with the DMD, implemented through feedback processes described in section 2.3.4. However, introducing additional light inside the box is not an ideal solution. The main advantage of working with a repulsive potential lies precisely in keeping the atoms "in the dark", reducing light scattering which is in any case non-zero, and causes losses or heating of the sample. This approach helps maintain a naturally homogeneous system and minimizes adverse effects on the atoms.

Moreover, if one attempts to generate an optical linear potential, the accuracy with which it is created and calibrated to match and counteract gravity becomes critical and is a potential source of error. Moreover, introducing an optical potential inside the box reduces the effective height of the confinement, which is designed to be hard-wall. In practice, the effective wall height is lowered to the difference between the maximum value of the optical gradient and the wall potential itself. A scheme of this fact is shown in figure 2.18. In addition, as shown by the simulation in Section 2.3.1, it becomes clear that — unless one employs powers greater than 2 W, which are very far to those considered in the simulated case — optical compensation of the simulated potential is not feasible. This is because the region over which such a balance could be applied is limited to the $18 \mu\text{m}$ where the atoms remain trapped, and the resulting trap depth would be essentially negligible.

The choice therefore falls on the use of a magnetic potential. Indeed, from the Zeeman interaction (see Eq. (2.1)) one can obtain a linear potential by employing a pair of coils in a Anti-Helmholtz configuration. For this reason, the MOT coils are ramped up just before the loading of the box potential and in this way, as shown in figure 2.19c, the atoms are no longer compressed against the lower light sheet used for vertical confinement, but, upon increasing the current in the MOT coil, they expand to fully occupy the box. In this way, the orientation of the box is no longer strictly tied to the density and thus to possible inhomogeneities in the system. As a result, small tilts of the box with respect to the horizontal direction do not pose a problem for the experiment. In any case, the angle previously determined for

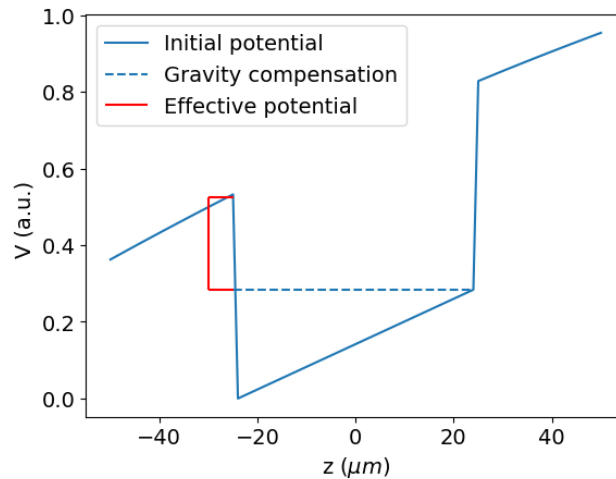


Figure 2.18. Simulation of gravity compensation using an optical gradient. The solid blue line shows the trapping potential including the gravitational potential. In this simulation, an optical potential equal and opposite to the gravitational potential is added inside the box, so that the resulting sum is constant (blue dashed line). Although the potential inside the box becomes flat, the effective trap depth is given by the difference between the highest point of the gradient and the height of the confining walls. Consequently, the effective confinement potential is reduced, as shown by the red line.

the horizontal direction is used, ensuring that the two DMDs are orthogonal. In this way, the vertical imaging system is also well aligned with the box, as soon as it is collinear with the green light from the vertical DMD. This avoids imaging distortions caused by different regions of the gas being brought into focus at different depths.

As shown in Fig. 2.19, the atomic distribution before and after gravity compensation demonstrates that the density along the vertical axis (z -axis in Fig. 2.19c) remains essentially uniform. This observation indicates that the residual effect of gravity on the system is negligible once the compensation is applied. To quantitatively confirm the cancellation of gravity, we investigate the free expansion of the atomic cloud. This procedure is implemented using a cloud in the BEC regime, confined in the optical trap generated by the IPG and Mephisto laser systems. Subsequently, all trapping potentials are switched off, and the free fall of the gas is measured both while keeping the compensation field active and without any compensation field.

Figure 2.20 shows the atomic cloud position, obtained from a gaussian fit of the expanding cloud, as a function of the time of flight of the expansion, for both cases. From the fits of a parabolic function like $z(t) = z_0 + \frac{1}{2}at^2$, we extract an acceleration of

$$a = -10.26 \pm 0.04 \text{ m/s}^2, \quad (2.19)$$

without any compensation active. The difference between the expected value of 9.81 m/s^2 can be attributed to the Feshbach field that is constant in the horizontal plane, but it creates an anti-confinement quadratic potential in the vertical direction. More than this it could be present also spurious magnetic field gradients remaining within the system that are not easily controlled or eliminated. By measuring the expansion of the gas with the compensation field

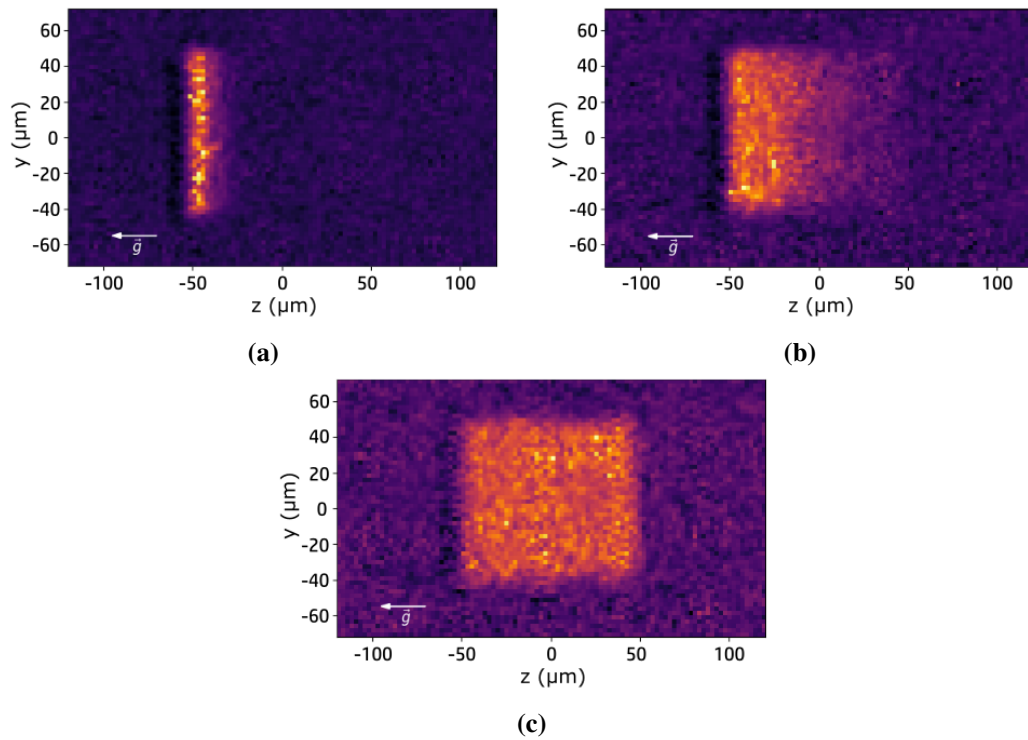


Figure 2.19. Images of the gas in the BEC regime confined in a cubic box with a side length of $100 \mu\text{m}$. (a) The atoms are displaced downwards (to the left in the image) due to the effect of gravity. (b,c) After applying the magnetic compensation field, the atoms redistribute uniformly throughout the entire box potential.

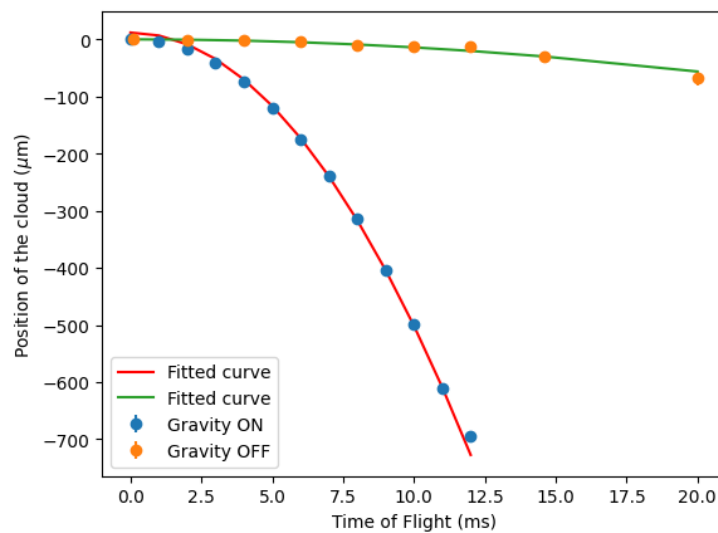


Figure 2.20. Plot of the gas position as a function of time of flight. Once all confining potentials are switched off, leaving only the magnetic field that compensates gravity, the gas expands while falling with an acceleration equal to the residual acceleration. The gas position is extracted from a gaussian fit. The system was in a weakly interacting BEC regime. Despite the BEC regime, the condensed fraction is negligible; nevertheless, the gaussian fit provides reliable information about the cloud position.

on, we measure an acceleration of

$$a = -0.27 \pm 0.02 \text{ m/s}^2. \quad (2.20)$$

This corresponds to a gravity compensation of approximately 97 %. This does not imply that generating gradients beyond this value is impossible; in fact, by further increasing the current through the MOT coils, we can overcompensate gravity, pushing the atoms against the upper light sheet of the box potential. The remaining acceleration is likely due to the anti-confining component of the Feshbach field. Unlike gravity or the MOT-induced potential, which are linear, this component is quadratic, and therefore cannot be perfectly compensated at every point in space. Nevertheless, since the condition of in-situ homogeneity is well satisfied, we consider this level of compensation sufficiently accurate for the purposes of this thesis. Furthermore, as expected we observe that the field needed for the gravity compensation vary depending on the Feshbach field at which the system is operating, due to the different curvature that it introduces, and thus on the regime under investigation (BEC, BCS, or UFG).

2.5.3 Gradients compensation

After compensating for gravity and achieving a uniform density along the vertical direction, we can turn our attention to the density distribution in the horizontal plane, as observed from the vertical imaging. To this end, we operate in the weakly interacting BEC regime, where the low chemical potential makes the system highly sensitive to even small deviations of the potential from homogeneity, which directly manifest as density modulations.

Under these conditions, the system appears as shown in Fig. 2.21. A clear imbalance in the atomic density is visible in the upper-right region of the image, revealing the presence of a relatively strong potential gradient in that direction.

To identify these gradients with higher precision, I developed a Python program that processes the absorption images acquired by the imaging system. The algorithm extracts the atomic signal and performs a linear fit of the density profile as a function of the angle with respect to the center of the atomic cloud, and represents this gradient with an arrow pointing along its direction (as one can see in fig 2.21a and 2.23a). In this way, it determines the axis along which the gradient is strongest, indicating how the system should be moved. Indeed, such gradients can arise from a slight misalignment of the MOT or Feshbach coils. By translating the box trap, together with the ODT itself, toward the center of these coils, the gradients are significantly reduced. For an even finer compensation, I have also installed a pair of additional coils.

The two coils are made by 20×5 spires each one and are placed vertically around the science chamber in order to generate additional magnetic fields that compensate for small potential gradients. In particular, with the reference to Fig. 2.3, the coils are positioned in correspondence with the MOT beam exit windows. Due to the limited accessibility of the mounting region, as one can guess from Fig. 2.22, the alignment of the coils is not perfect. As a result, they generate not only horizontal gradients but also a residual vertical component.

It is therefore necessary to iteratively adjust the currents in the MOT and vertical coils so that gravity and any other unwanted gradients in all directions are properly compensated. The result of the horizontal compensation is shown in Fig. 2.23b. As can be seen, the system is not yet perfectly uniform, in contrast to the unitary gas shown in Fig. 2.24, where strong interactions enhance homogeneity by making high-density regions energetically unfavorable.

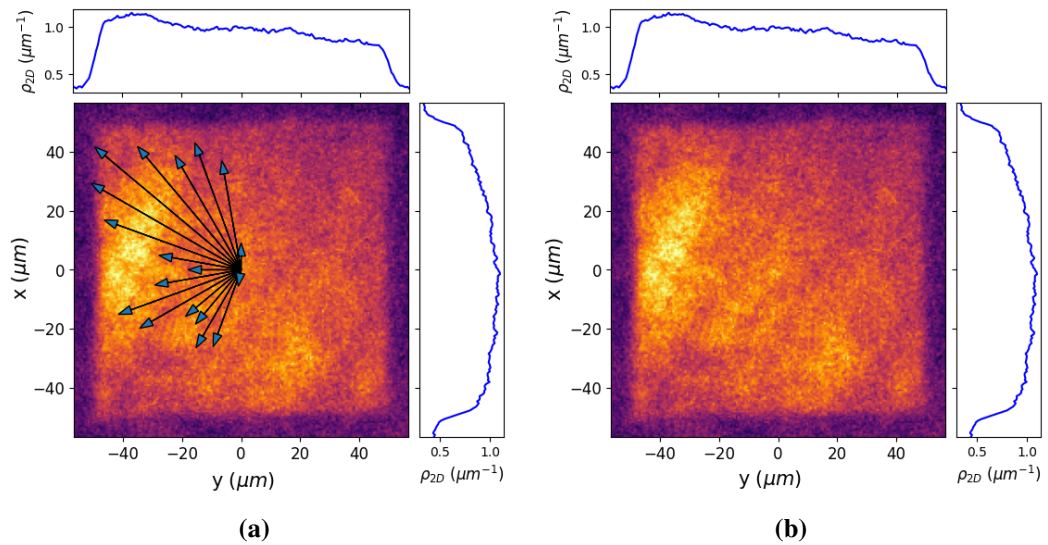


Figure 2.21. Image of the gas in the BEC regime, confined in a cubic box with a side length of $100\ \mu\text{m}$, taken with vertical imaging. In this case, gravity is compensated, but a residual gradient in the plane pushes the atoms towards the left side of the box (in the image). Above and to the right of the main panel, the integrated density profiles along the two directions are shown. In figure (a), the arrows indicate the directions and magnitudes of the remaining density gradients, as obtained with the Python analysis program.

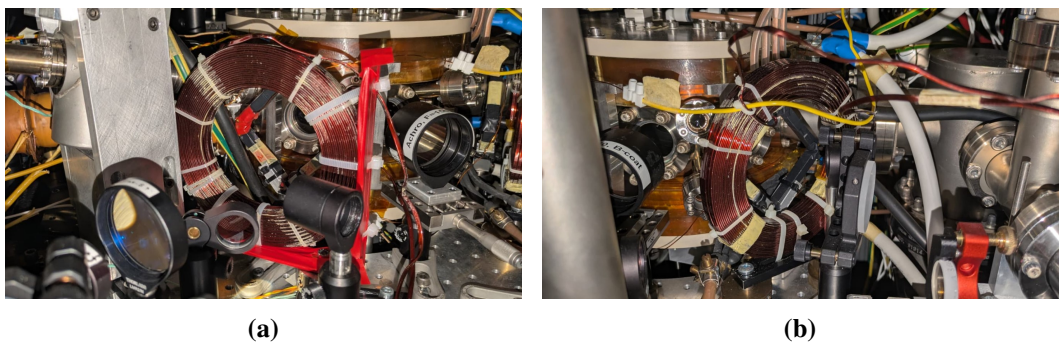


Figure 2.22. Photo of the horizontal coils, used to compensate for residual magnetic field gradients along the horizontal direction. These coils are mounted around the science chamber, as shown in figure 2.3

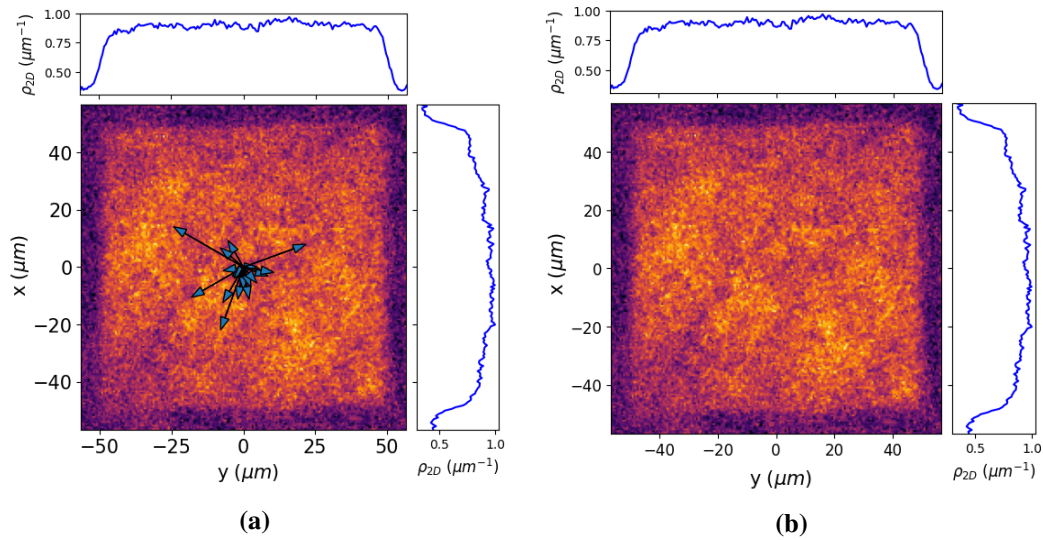


Figure 2.23. Image analogous to Fig. 2.21. Here, the compensation coils are switched on. The field makes the potential inside the box more uniform, resulting in a more homogeneous density, as shown by the integrated density profiles and the arrows in (a). Indeed, the arrows are shorter and approximately distributed in all directions.

Nevertheless, one should keep in mind that the square system realized here corresponds to a cube with a side length of $100 \mu\text{m}$, which is already comparable to the largest system sizes typically employed in such studies. Since homogeneity is expected to improve as the system size is reduced, we consider the degree of uniformity achieved here to be well suited for operating the box trap under these conditions.

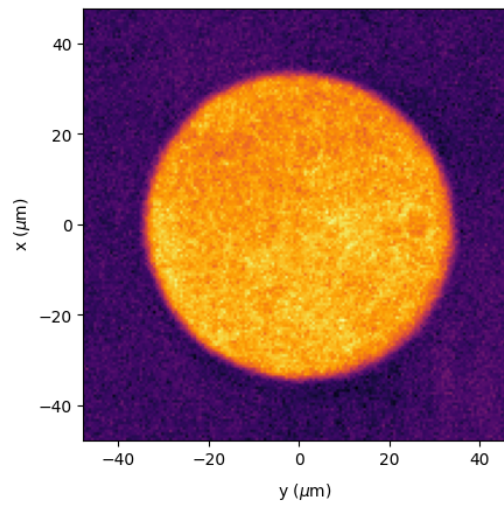


Figure 2.24. Example of a cylindrical box potential, with the image taken using the vertical imaging system. Thanks to the use of DMDs, it is very simple to change the shape of the box potential by simply modifying the image loaded onto the DMD.

Chapter 3

Probing quantum statistics

The following chapter deals with the initial measurements performed using the new trapping system. In particular, after discussing the model describing the expansion of the gas, measurements are carried out to obtain the momentum distributions of the gas in the ideal regime for fermions—Fermi-Dirac distribution—and for bosons—Bose-Einstein distribution. From these quantities, temperature and chemical potential can also be derived, enabling a direct comparison with theoretical models. Alongside the primary measurements, additional auxiliary measurements were performed to verify the applicability of the chosen model, specifically testing its underlying assumptions.

3.1 Expansion model

Let's consider a non degenerate Bose or Fermi gas. If the mean free path λ_c between collisions is longer than the size of the cloud $\lambda_c \gg L$, we can neglect collisions during expansion, which is hence ballistic. This condition can be expressed in terms of the density n and the scattering length a . Indeed:

$$\lambda_c = \frac{1}{n\sigma} = \frac{1}{4\pi na^2} \gg L \quad (3.1)$$

where σ is the scattering cross section of the atoms and L represents the longest dimension that the trap can accommodate.

In this expansion regime, also called ballistic expansion, a particle initially at point r_0 in the trap, will reach point $r = r_0 + \frac{p_0}{mt}$ after expansion time t . By integrating all the contributes of the momenta, we can find that the density of the gas expanding in time of flight, for a general case, can be written as:

$$\begin{aligned} n_{3D}^{TOF}(r, t) &= \int d^3r_0 \int \frac{d^3p_0}{(2\pi\hbar)^3} f(r_0, p_0) \delta\left(r - r_0 - \frac{p_0}{m}t\right) = \\ &= \frac{1}{(2\pi\hbar)^3} \frac{m^3}{t^3} \int d^3r_0 \frac{1}{\exp\left[\beta\left(\frac{m}{2t^2}|r - r_0|^2 + V(r_0) - \mu\right)\right] \mp 1}, \end{aligned} \quad (3.2)$$

where r_0 is the initial position of the atom inside the trap, $V(r_0)$ is the trap potential and the \mp are referred to the bosonic and fermionic case respectively.

Now, if we consider the scenario of a box potential of volume $\Omega = L_x L_y L_z$, with the trapping potential defined as $V(r) = 0$ if $r \in \Omega$ and $V(r) = +\infty$ otherwise, we can write the density as:

$$n(r, t) = \left(\frac{m}{2\pi\hbar t} \right)^3 \int \frac{1}{\exp \left[\beta \left(\frac{|r-r_0|^2}{R_{th}^2} - \beta\mu \right) \right] \mp 1} \prod_{i=x,y,z} \text{rect} \left(\frac{r_{0,i}}{L_i} \right) d^3 r_0, \quad (3.3)$$

where $R_{th} = \sqrt{\frac{2k_B T}{m}} t$ is the thermal radius and rect the rectangular function which is defined as $\text{rect}(x) = 1$ if $|x| \leq \frac{1}{2}$ and $\text{rect}(x) = 0$ otherwise. Now, if we consider the limit for small volumes, $\Omega \rightarrow 0$, the integral can be calculated and we find that:

$$n(r, t) \stackrel{\Omega \rightarrow 0}{=} \left(\frac{m}{2\pi\hbar t} \right)^3 \frac{\Omega}{\exp \left[\left(\frac{r^2}{R_{th}^2} - \beta\mu \right) \right] \mp 1}. \quad (3.4)$$

Anyway, the limit of $\Omega \rightarrow 0$ corresponds to the limit where the initial volume is very small compared to the dimension of the expanded cloud. This means that we can consider the limit analogue to the limit $\frac{\Omega}{R_{th}^3} \ll 1$ that, seen the definition of R_{th} , is comparable to the limit for long time of flight, when the atomic distribution has lost any information about where the atoms were inside the trap when the trap was turned off.

In this way we have a direct link between the density of the cloud, measured in long time of flight, and the momentum distribution $f(k)$. Indeed we can write the equation (3.4) for the 1D case as [47]:

$$n_{1D}(z_t) = A f_{1D}(k_z) = \frac{A}{4\pi^2} \int_{-\infty}^{+\infty} f(k_x, k_y, k_z) dk_x dk_y, \quad (3.5)$$

where, for the ballistic expansion hypothesis $z_t = \frac{\hbar k_z}{m} t$, A is a constant and $f(k_i)$ denotes the momentum distribution along the i -th direction.

By switching to cylindrical coordinates and assuming that the distribution is spherically symmetric in momentum space, so that $f(\vec{k}) \equiv f(k)$ with $k = |\vec{k}|$, one obtains

$$\frac{df_{1D}(k_z)}{dk_z^2} = -\frac{1}{4\pi} f(k), \quad (3.6)$$

which, combined with Eq. (3.5), allows the three-dimensional momentum distribution $f(k)$ to be reconstructed directly from the derivative of the measured density $n_{1D}(z_t)$.

The constant A is determined from the total particle number:

$$N = \frac{V}{2\pi} \int_{-\infty}^{+\infty} f_{1D}(k_z) dk_z = \frac{Vm}{2\pi\hbar t A} \int_{-\infty}^{+\infty} n_{1D}(z_t) dz_t, \quad (3.7)$$

which yields:

$$A = \frac{Vm}{2\pi\hbar t}. \quad (3.8)$$

Finally, the occupation-number distribution can be expressed as

$$f(k) = -\frac{8\pi^2 \hbar^3 t^3}{Vm^3} \frac{dn_{1D}(z_t)}{d(z_t^2)}. \quad (3.9)$$

In the following sections, we describe the experimental sequence required for the preparation of both fermionic and bosonic systems, as well as the subsequent analysis and the results obtained. Once $f(k)$ has been obtained, one can perform a fit using either a Fermi-Dirac or a Bose-Einstein distribution, depending on the case, from which the system temperature and chemical potential can be extracted.

3.2 Fermi distribution

3.2.1 Preparation of the gas

For the preparation of the ideal Fermi gas, we have two possibilities: the first one is by flashing out one of the two species present in the system, remaining with just one species that is naturally non interacting, while the second possibility is to not blast out the gas, remaining with the two species, but going with the Feshbach resonance to the zero crossing, a condition where the scattering length and so the interaction goes to zero and the mixture acts as two non interacting ideal gas that do not feel each other. For the following measures we have chosen the second possibility. This choice arises from the fact that the blasting process uses light resonant with the state we intend to remove. Seen that the resonances of the two states are relatively close to each other, the resonant light for one species also affects the other state via scattering force, eventually heating up the remaining atoms.

The lithium gas is initially prepared at the crossover field, as described in section 2.1. After the evaporation the magnetic field is tuned from 690 G, to 300 G where we finish the evaporation of the Fermi gas. We choose to conclude the evaporation of the ODT at this magnetic field because, under these conditions, the atoms do not form Cooper pairs. In fact, the critical temperature - which at this field essentially coincides with the pair formation temperature - is very low and will certainly not be reached by the gas at this stage. This can be understood from Fig. 1.4, considering the interaction at a magnetic field of 300 G and the density of our system, the interaction parameter takes values of about $1/k_F a = -12$. After the evaporation in the ODT, the gas is transferred into a box potential with cubic geometry and a side length of $45 \mu\text{m}$. Once confined in the box, an additional cooling stage is implemented through a procedure analogous to evaporative cooling: the box walls are temporarily lowered and gravity is partially reintroduced, allowing the most energetic atoms to escape from the bottom of the trap and thereby cooling the system. This step is performed at a magnetic field of 300 G to enhance rethermalization. Subsequently, the box walls and gravity compensation are restored to their initial values, and the magnetic field is tuned to the zero crossing at 568 G, where the gas is non-interacting.

Finally, the trap is switched off and the gas undergoes time-of-flight expansion. An example of the absorption image recorded with the horizontal camera, used for these measurements, is shown in Fig. 3.1, where both the atoms confined in the box potential and their distribution after 4 ms of time of flight can be observed.

3.2.2 Time of flight analysis

To validate the assumption of long expansion times introduced in Chap. 3.1, we carried out measurements at different times of flight (TOF), from 0 to 9 ms, while keeping the final evaporation power of the box trap fixed.

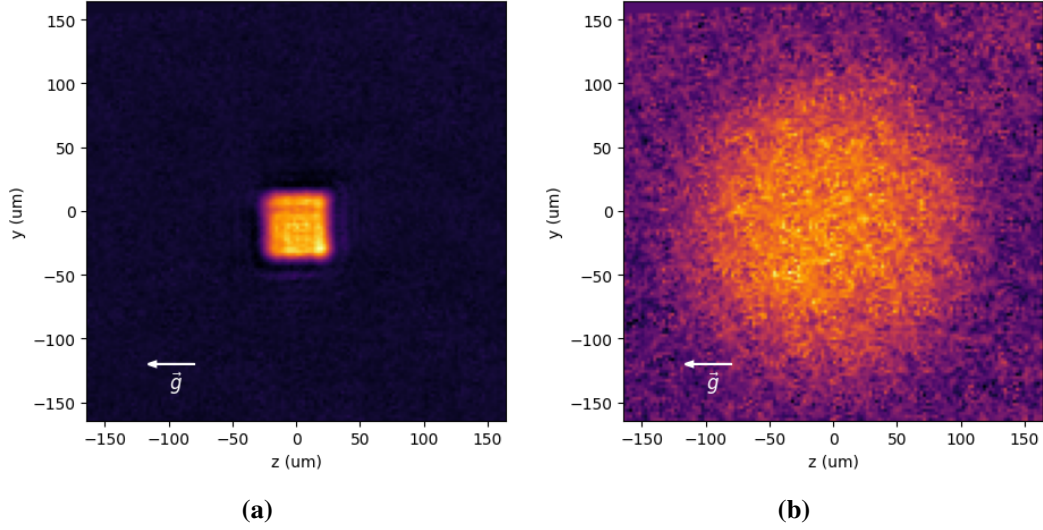


Figure 3.1. (a) Image of the ideal Fermi gas confined within a cubic trap with side length $45 \mu\text{m}$, taken with the horizontal imaging system. This image shows the in-situ density distribution of the gas in the trap. (b) Image of the Fermi gas after 4 ms of time-of-flight expansion. The horizontal imaging is chosen because the field of view of this camera is wider than the vertical one. Giving us the possibility to explore more time of flight for the Fermi gas.

As shown in Fig. 3.2a, the 1D density profiles obtained after averaging the measurements taken under the same time-of-flight conditions still appear extremely noisy. This is problematic, because the subsequent analysis requires the calculation of a numerical derivative of the signal. To make these profiles analyzable, we apply a two-step smoothing procedure:

- (1) **Bootstrap averaging.** We implement a bootstrapping-like technique: from the set of images acquired at the same TOF we repeatedly draw random ensembles, compute their mean images. This averaging suppresses noise, as illustrated in Fig. 3.2b.
- (2) **Low-pass filtering.** We perform a Fourier transform of each 1D density profiles obtained from the bootstrap procedure and fit the central peak of the power spectrum with a gaussian function (see Fig. 3.2c). All frequency components lying more than three standard deviations away from the peak center are discarded.

So, at this point we have a huge number of smoothed profiles given by the bootstrapping and low pass filtering procedure for each time of flight. Therefore we proceed calculating the numerical differentiation for each profile. To minimize artifacts arising from the finite-difference calculation itself, we compute derivatives using second-, fourth- and sixth-order finite-difference schemes, that are defined, for a generic function $f(x)$ as [48]:

$$\begin{aligned}
 f'_2(x) &\approx \frac{f(x+h) - f(x-h)}{2h} \\
 f'_4(x) &\approx \frac{-f(x+2h) + 8f(x+h) - 8f(x-h) + f(x-2h)}{12h} \\
 f'_6(x) &\approx \frac{f(x-3h) - 9f(x-2h) + 45f(x-h) - 45f(x+h) + 9f(x+2h) - f(x+3h)}{60h}
 \end{aligned} \tag{3.10}$$

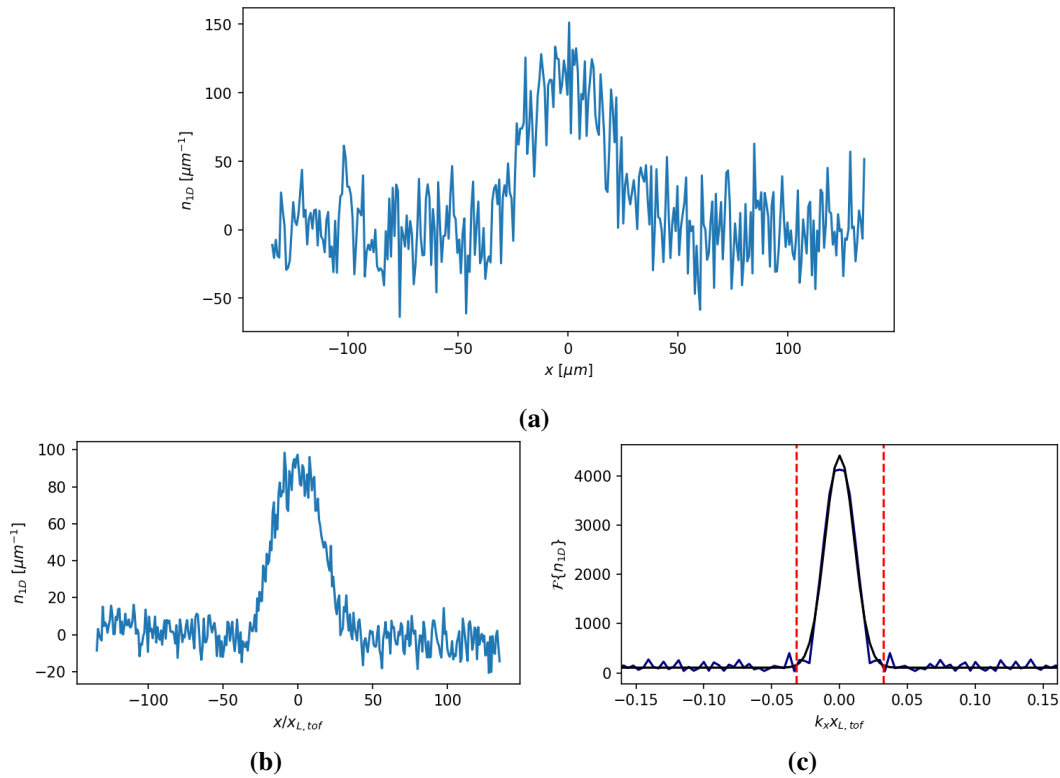


Figure 3.2. (a) One-dimensional density profile after 4 ms of time of flight, obtained by integrating the signal acquired with the horizontal imaging system along one direction. As can be seen, the signal is very noisy, making it impossible to compute the numerical derivative required for further analysis. (b) One-dimensional density profile after 4 ms of time-of-flight, obtained following the Bootstrap averaging procedure. As compared to Fig. (a), this process reduces the noise significantly, although the profile is still too noisy for reliable numerical differentiation. (c) Fourier transform of the signal shown on the left. The Fourier transform is truncated in the regions corresponding to high frequencies, highlighted by the red dashed lines, to allow reconstruction of a less noisy signal via a low-pass filter.

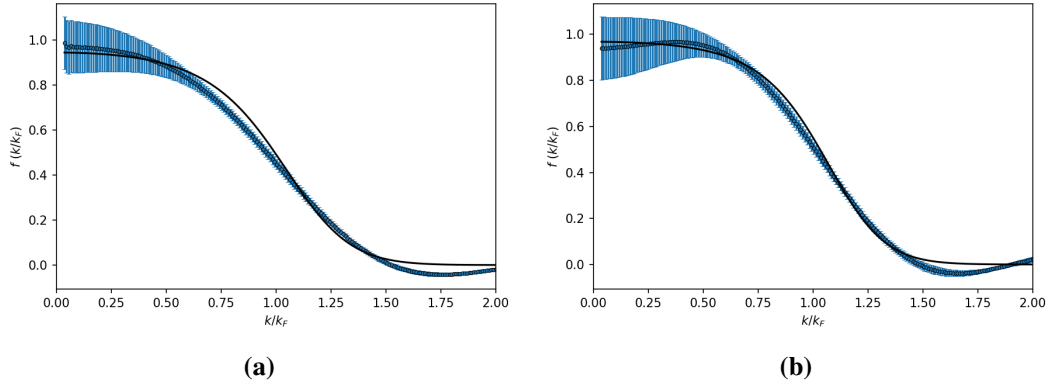


Figure 3.3. Momentum distributions extracted from the processed data for time-of-flight durations of 4 ms **(a)** and 8 ms **(b)**, along with the Fermi–Dirac fit. The error bars represent the statistical uncertainty from averaging multiple measurements.

Then we take their mean as our best estimation for the derivative. Multiplying this derivative by the appropriate factors from Eq. (3.9) gives the momentum distribution $f(k)$, as shown in Fig. 3.3, where positive and negative momenta are combined into a single symmetric distribution.

Once the momentum distribution is obtained, we fit it with the Fermi–Dirac function, Eq. (1.13), to extract the reduced temperature T/T_F and the chemical potential μ . Figure 3.4 shows the evolution of these two quantities as a function of the TOF. Both values saturate beyond a certain TOF, indicating that beyond this threshold the expansion is sufficiently long for the spatial information about the trap to be lost, as required by the model.

A simple semiclassical estimate of this threshold time τ can be made as follows. Consider a cubic trap of side L . At $T = 0$ the gas occupies all momentum states up to $k = k_F$, and the maximum distance across the cube is $d = \sqrt{3}L$. We define τ as the time for a particle moving at velocity $\hbar k_F/m$ to traverse the distance d , yielding

$$\tau = \frac{\sqrt{3} mL^2}{\hbar(6\pi^2 N)^{1/3}} \simeq 4 \text{ ms}, \quad (3.11)$$

where the atom number $N \simeq 1.0 \times 10^4$ is obtained from image analysis and $L = 45 \mu\text{m}$.

Another way to estimate this timescale is to consider the angular distribution. In particular, when the gas is trapped, the profile obtained by integrating from the center of the system outward in the radial direction, as a function of the angle with respect to which the integration is performed, strongly depends on the shape of the trapping potential. As shown in Fig. 3.5, in the case of a square trap, pronounced peaks appear at the angles corresponding to the diagonals of the square (blue line). The condition we are interested, corresponds to have an expansion that washes out the memory of the initial trap — and so to a profile that is flat within the experimental noise.

Such a profile, obtained after a 4 ms time of flight, is shown in Fig. 3.5 (purple line) and appears, within the experimental noise, essentially constant. This observation confirms our assumption that a time of flight of 4 ms is sufficiently long to reach the asymptotic regime. It is important to note, however, that this method is strongly dependent on the initial shape of the trapping potential. In particular, if the system were initially characterized by a circularly symmetric potential (as the one in figure 2.24) with respect to the imaging axis,

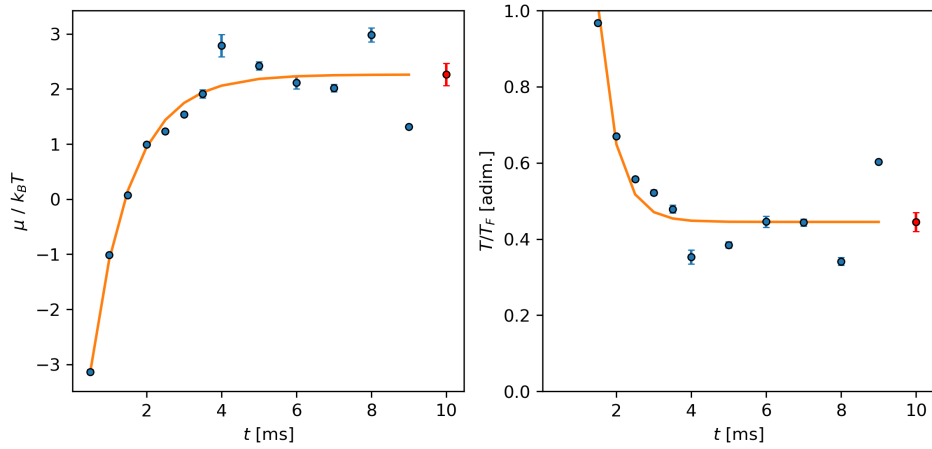


Figure 3.4. Time-of-flight dependence of the chemical potential $\beta\mu$ (left) and reduced temperature T/T_F (right). The solid lines represent fits to the saturation function f_{sat} . The red point marks the fit parameter $a \pm \Delta a$, taken as the most reliable value for each quantity.

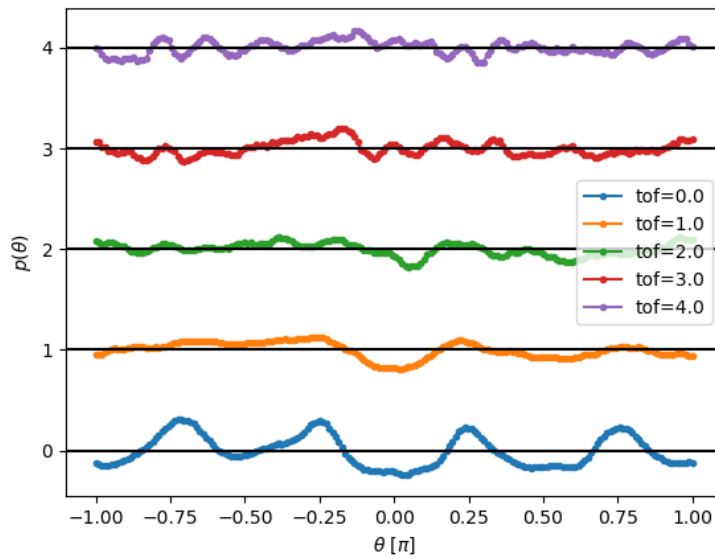


Figure 3.5. Profile obtained by radially integrating the signal from the center of the system outward, using an image analogous to the one in Fig. 3.1a, as a function of the angle along which the integration is performed, for different time-of-flight durations. As shown, for short times of flight, pronounced maxima appear at angles corresponding to $\pm\pi/4$ and $\pm3\pi/4$, highlighting the strong angular dependence imposed by the initial trap geometry. These angles correspond to the diagonals of the square box potential visible in the reference image. For longer times of flight, these peaks are no longer visible, and the profile is nearly constant, except for fluctuations associated with noise.

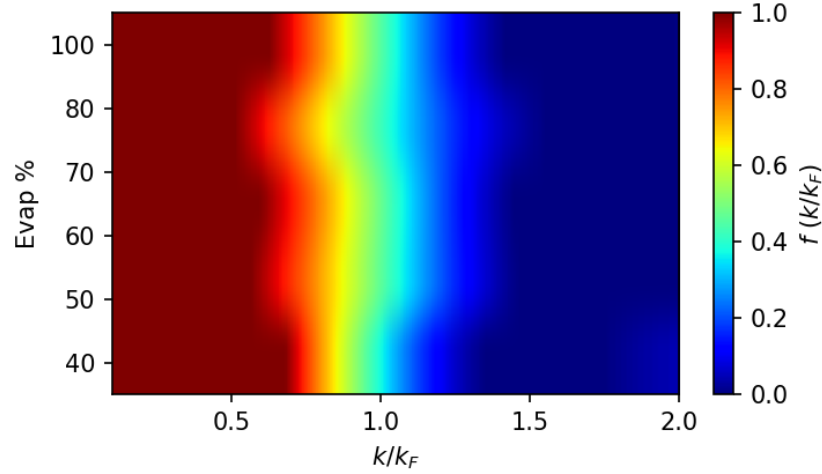


Figure 3.6. Momentum distribution diagram $f(k/k_F)$ as a function of box potential evaporation. The y -axis indicates the final trap power as a percentage of the initial value. As can be seen, for low k values a Fermi sea develops, while for $k \gg k_F$ the occupation $f(k/k_F) \rightarrow 0$.

the peaks would not appear at any time, even though this does not imply that the time of flight is already long. Therefore, this procedure cannot provide an exact determination of the minimum expansion time required to reach the long-time limit; it serves only as an additional consistency check of the value previously obtained.

The measurements in Fig. 3.4 are in good agreement with this estimate.

To extract the asymptotic values of T/T_F and $\beta\mu$, we fit the data with a saturation function

$$f_{\text{sat}}(t) = a + b e^{t/c}, \quad (3.12)$$

where the parameter a provides the best estimate of the long-TOF limit for both quantities. The analysis yields

$$\frac{T}{T_F} = 0.45 \pm 0.16, \quad \beta\mu = 2.3 \pm 0.2, \quad (3.13)$$

where the errors are derived from the fit.

3.2.3 Momentum distribution

Once we established the TOF conditions required to ensure long expansions, we now focus on a single expansion time while varying the final evaporation power of the box potential. In this case the TOF is fixed to 10 ms, well above the limit found.

Following the same analysis procedure as before, we reconstruct the momentum distribution for different evaporation ramps (see Fig. 3.6). As expected, we have the formation of the Fermi sea, for the lowest k -states, and the probability of occupation of these states goes to 1 (dark red). Another thing that one can see is that $f(k/k_F) = 1/2$ (in green-light blue in the diagram) corresponds to $k/k_F \simeq 1$, that is a characteristic behavior of the ideal Fermi gas. Moreover, the width of the transition zone between the Fermi sea, where $f(k/k_F) = 1$, and the region with $f(k/k_F) = 0$ (dark blue), decreases as the final evaporation power is reduced, providing a first indication that the evaporation ramp effectively "cools" the system.

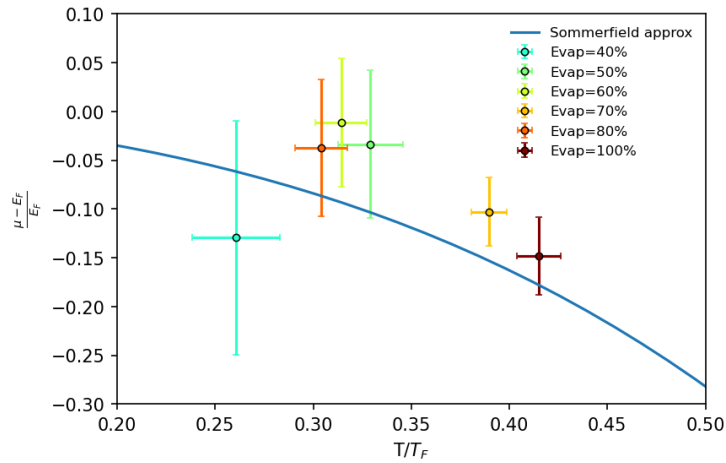


Figure 3.7. Measured values of the relative chemical potential $(\mu - E_F)/E_F$ as a function of the reduced temperature T/T_F for different evaporation percentages of the box potential (color-coded points). The solid line shows the Sommerfeld approximation prediction for an ideal Fermi gas.

It is important to emphasize that this "cooling" does not refer to the absolute temperature, but rather to the reduced temperature T/T_F . This is indeed the quantity that governs and characterizes the degeneracy of the system, and it is therefore the parameter that will be considered in the following analyses.

Figure 3.7 shows that T/T_F indeed decreases as the evaporation power is lowered. As can be seen, the data point corresponding to an evaporation of 70% evap the initial laser power, appears anomalous when compared with the overall trend. Although the laser power — and therefore the trap depth — is lower than in the 80% evap case for example, but the measured reduced temperature is actually higher than the one at 80% evap . This discrepancy may be due to statistical fluctuations affecting the measurement at 70% evap : this measurements were acquired at the end of the experimental run; thus, the experimental conditions may have changed over time between the first and the last measurements, causing these data to be shifted with respect to the others. As a first result, this study clearly confirms that the technique of evaporative cooling, when applied to a box potential, is equally effective.

In the figure 3.7 is illustrated the relationship between the chemical potential μ , rescaled with the Fermi energy, and the temperature T/T_F for the Fermi gas. At absolute zero temperature $T = 0$, according to the ideal Fermi-Dirac model, the chemical potential μ coincides exactly with the Fermi energy E_F . At finite temperature $T > 0$, the sharp occupation at E_F is smoothed out due to thermal excitations and this introduces a deviation to the respect with the case at $T = 0$. The Sommerfeld approximation provides a useful analytical expression for $\mu(T)$, valid in the low-temperature regime $T/T_F \ll 1$. Using this method, the chemical potential decreases slightly from E_F as temperature increases, and can be expressed as:

$$\mu(T) = E_F \left[1 - \frac{\pi^2}{12} \left(\frac{k_B T}{E_F} \right)^2 - \frac{\pi^4}{80} \left(\frac{k_B T}{E_F} \right)^4 + \dots \right] \quad (3.14)$$

As shown in Figure 3.7, there is good agreement between the Sommerfeld approximation

	a (a_0)	$1/k_F a$
BEC ⁶³³	1143.0	9.3
BEC ⁶⁴⁴	3770.5	2.4

Table 3.1. Table of the scattering lengths a and the interaction parameters $1/k_F a$ for the two BEC systems studied

(in blue) and the experimental data points. However, the experimental points consistently exhibit slightly higher values of the chemical potential compared to those predicted by the Sommerfeld approximation.

Regarding the data point at 40%, it appears somewhat outside the trend established by the other points, even if it is compatible with the theory within the errorbars. This deviation may be attributed to the fact that, with more extensive evaporation, the resulting atom number is significantly lower than in the other cases, leading to a reduced signal-to-noise ratio. The slight upward shift observed in the other data points could also be due to artifacts introduced by the smoothing and analysis procedures. By filtering out high-frequency components, sharp features in the profiles are lost. As a result, the measured temperature may appear higher than the actual temperature, and the chemical potential could also be shifted by this process.

In any case, we can conclude that the measured values are in good agreement with the theoretical predictions.

3.3 Bose distribution

3.3.1 Production of the gas

Regarding the sequence for the creation of a Bose gas, we proceed analogously to the ideal Fermi gas measurements, starting from a $|1\rangle - |3\rangle$ spin mixture in the unitary regime (with the Feshbach field set at 690 G), confined in the optical dipole trap (ODT). After performing evaporative cooling, the magnetic field is swept to the final value on the BEC side of the Feshbach resonance, such that the lithium atoms form bound molecular states, which behave as bosons. The measurements are carried out at two different final fields, 664 G (BEC⁶⁶⁴) and 633 G (BEC⁶³³). It is important to note that the first magnetic field corresponds to a more strongly interacting BEC, since at this value the gas is closer to the Feshbach resonance, while the second one corresponds to a less interacting BEC, deeper on the BEC side. More specifically, the parameter that characterizes the interaction regime is na^3 . If this quantity is greater than one, the gas is considered to be in the strongly interacting regime, whereas if it is smaller than one, the gas can be regarded as weakly interacting. As we will see, the bosonic gases prepared at the two different magnetic fields fall both into the weakly interacting regime, even if the BEC⁶⁶⁴ is more interacting.

In the table 3.1 are shown the main quantities that characterize the interaction regime of the gases.

After the evaporative cooling stage in the ODT, the gas is loaded into the box trap, with a cubic geometry, with a side length of $45\ \mu\text{m}$. Once the gas is confined in the uniform potential, a procedure that can be regarded as an evaporative cooling scheme within the box potential is processed. In particular, gravity is partially reintroduced and the potential

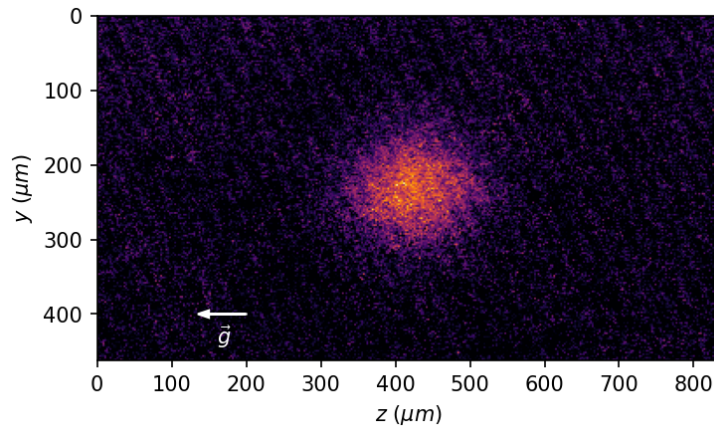


Figure 3.8. Image of the atomic cloud in the BEC⁶³³ regime after 10 ms of free expansion, acquired using the horizontal imaging system.

height is lowered, such that the most energetic atoms (in this case bound pairs) escape. After rethermalization, the system attains a lower temperature. Density distributions were recorded after 10 ms of time of flight for both cases, for different final value of box-potential evaporation.

An example of the signal after 10 ms of time of flight is reported in Fig. 3.8.

3.3.2 Momentum distribution

With an analysis analogous to the previous case, the measured profile is first cleaned and then numerically differentiated. In this way, we obtain the momentum distribution $f(k/k_F)$ as a function of the evaporation power, for both the BEC⁶³³ and BEC⁶⁶⁴ cases. It is important to note that k_F is usually defined for fermions, but in this case, as is commonly done for bosonic systems composed of fermion pairs, we define this quantity also for the bosons, as in Eq. (1.8).

Let us start with the BEC⁶³³ case. The resulting distribution is shown in Fig. 3.9.

As can be seen, lowering the evaporation laser power leads to an increased occupation of the lowest-energy states, demonstrating that evaporation in this regime is efficient and effectively reduces the temperature of the system. The differences between this diagram and the fermionic case are evident: in the fermionic diagram (see Fig. 3.6), all states with $k/k_F \leq 1$ are occupied with a probability close to 1, and some states above $k/k_F = 1$ are also occupied with non-negligible probability. In contrast, in the bosonic case, the atoms occupy only the lowest-energy states, well below $k/k_F = 1$, thus providing clear evidence of the different statistical nature of the two gases. After fitting $f(k/k_F)$ with a Bose–Einstein function as in Eq. (1.13) (see Fig. 3.12), the chemical potential and temperature are extracted and shown in Fig. 3.11. From this plot, it can be seen that the temperature is effectively reduced as the evaporation laser power decreases, reaching values below the critical condensation temperature, $T_c = 0.22 T_F$, for evaporation powers below 65 % of the initial value. Moreover, one can see in image 3.12 that the peculiar behavior of the condensation can be observed: as the evaporation arrives at increasingly smaller values, the signal from the atomic cloud increases.

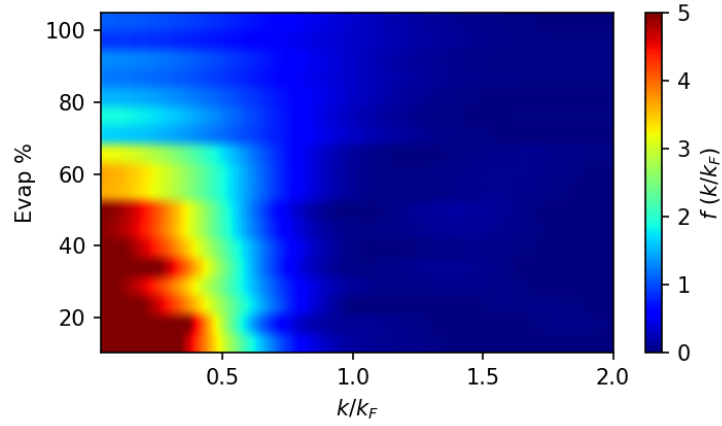


Figure 3.9. Momentum distribution diagram $f(k/k_F)$ as a function of box potential evaporation in the BEC⁶³³ regime. The y -axis shows the final trap power as a percentage of the initial value. For low k values and low evaporation, the distribution is highly peaked, reflecting the trend of the Bose-Einstein distribution, while for $k \gg k_F$, the occupation $f(k/k_F) \rightarrow 0$.

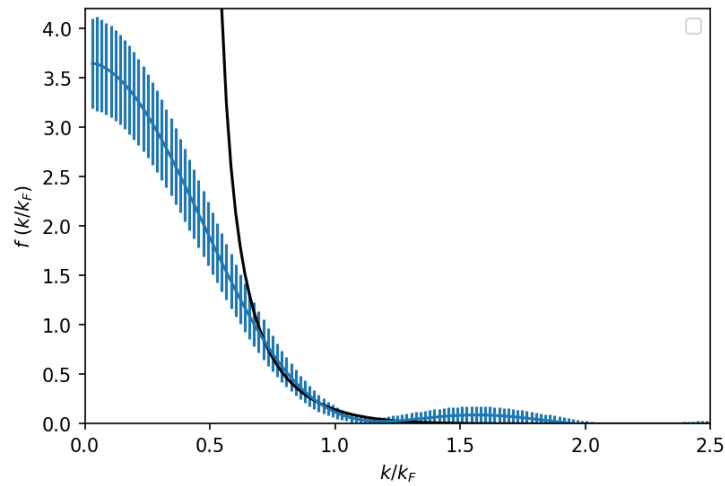


Figure 3.10. An example of the momentum distribution $f(k/k_F)$ obtained from the analysis is shown together with the corresponding fit using the Bose-Einstein distribution as defined in Eq. (1.13). This distribution corresponds to the measurement performed with the box potential evaporated to 60% of its initial depth. As can be seen, the fit accurately reproduces only the thermal tails of the distribution, since the model described in Sec. 3.1 accounts solely for a thermal Bose gas and does not include the contribution of the condensate.

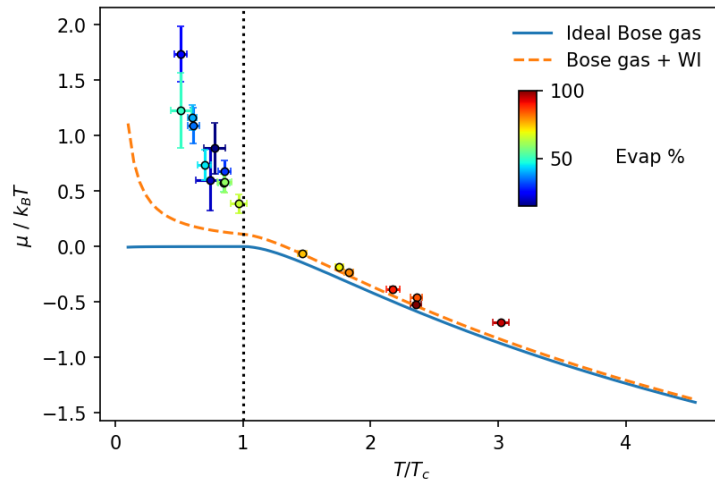


Figure 3.11. Measured chemical potential $\mu/k_B T$ as a function of reduced temperature T/T_c , color-coded by evaporation percentage. The solid line represents the theory for an ideal Bose gas, while the dashed line shows the prediction for a weakly interacting Bose gas. The vertical dotted line indicates the critical temperature for Bose-Einstein condensation.

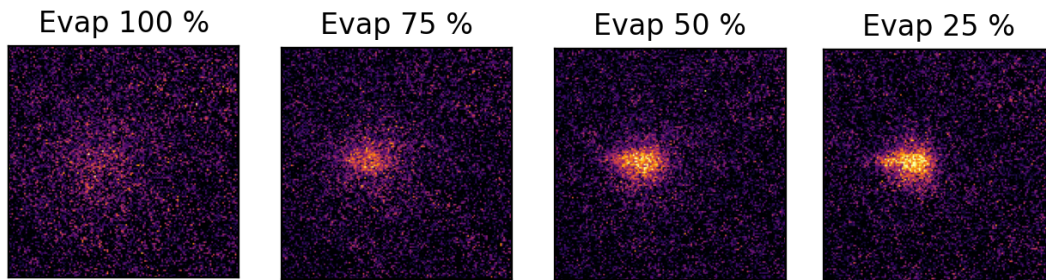


Figure 3.12. Image of the atomic cloud, in the BEC⁶³³ regime, after 10 ms time of flight for different values of box potential evaporation. As the final box potential height decreases, an increasingly large fraction of atoms remains visible, forming a progressively denser central region that corresponds to the emergence of the Bose–Einstein condensate.

On the graph, the ideal Bose gas model, which relates the chemical potential to the temperature (shown in blue), is plotted. In this model, the chemical potential is found by solving the equation:

$$\text{Li}_{3/2} \left(e^{\beta\mu} \right) = \zeta \left(\frac{3}{2} \right) \left(\frac{T}{T_c} \right)^{-\frac{3}{2}}. \quad (3.15)$$

As can be seen, for higher temperatures (corresponding to higher evaporation powers), the experimental points are close to the theoretical curve, although the measurements consistently lie above it. This deviation can be attributed to the presence of interactions, as the system is not an ideal Bose gas.

As already discussed, in this case the realized gas is in a weakly interacting regime, with $na^3 \simeq 2 \times 10^{-5}$. Therefore, it is possible to extend the ideal Bose gas model by including a weakly interacting correction, which adds a term $\mu_{\text{WI}} = gn$ to the ideal model (shown as the dashed orange line in the graph 3.11). This correction shows that, at temperatures above the critical temperature, the chemical potential follows the experimental data more closely.

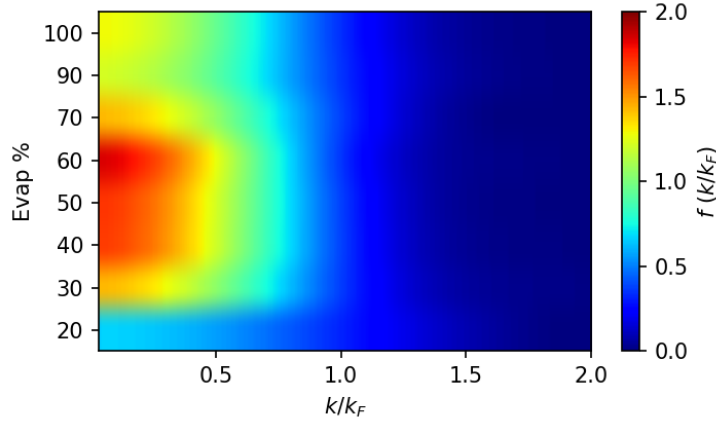


Figure 3.13. Momentum distribution diagram $f(k/k_F)$ as a function of box potential evaporation in the BEC⁶⁶⁴ regime. The y -axis shows the final trap power as a percentage of the initial value. For low k values and moderate evaporation, the distribution is peaked, following the Bose-Einstein distribution. However, at very high evaporation, the process becomes inefficient and atoms are lost without further cooling, resulting in a lower signal.

Furthermore, for temperatures below the critical temperature, the measured chemical potential significantly deviates from the ideal model. This is likely due to stronger interactions in the condensed fraction, which strongly affect the chemical potential. A more detailed investigation of this effect lies beyond the scope of this thesis.

We perform the same measurements for the BEC⁶⁶⁴ to determine whether evaporative cooling in the box remains effective at higher interaction strength. The state-occupation diagram (see Fig. 3.13) shows that, due to the stronger interactions, too low an evaporation power makes the evaporation process inefficient.

In this case, a larger fraction of atoms is lost overall — not only the hotter ones — thus reducing, rather than enhancing, the degree of degeneracy. These arguments also explain why, as shown in Fig. 3.14, the system cannot reach very low temperatures, and in fact, we never reach the critical temperature.

As for the chemical potential as a function of temperature, shown in Fig. 3.14, it can be seen that, in this case as well, the chemical potential is higher than that of an ideal Bose gas. Even in this case $na^3 \simeq 2 \times 10^{-3} \ll 1$, so we can add the correction to the model (see Fig. 3.14) and this correction (dashed orange line) improve the agreement between theory and experimental data. In any case, as in the previous case, a more detailed analysis of this behavior lies beyond the scope of this thesis.

Finally, it is important to emphasize that a crucial assumption underlying this analysis is the ballistic expansion, as described in the model in Section 3.1. While for the Fermi gas this assumption is easily justified, since the interactions are negligible at the zero-crossing where the measurements were performed, the same cannot be said for the bosonic gas.

By calculating λ_c , defined in Eq. (3.1), it is found that in the case of BEC⁶³³ this value is larger than the system size, with $\lambda_c/L \simeq 5$, which confirms that the analysis can be reliably performed as described. In contrast, for BEC⁶⁶⁴, the ratio $\lambda_c/L \simeq 0.2$, corresponding to a condition incompatible with ballistic expansion. In this case, the gas enters a hydrodynamic expansion regime, and the analysis performed no longer provides reliable measurements or

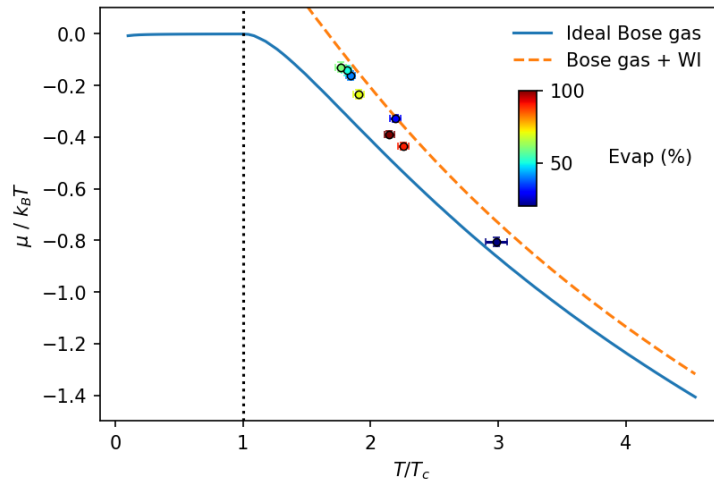


Figure 3.14. Measured chemical potential $\mu/k_B T$ as a function of reduced temperature T/T_c in the BEC⁶⁶⁴ regime, color-coded by evaporation percentage. The solid line represents theory for an ideal Bose gas, while the dashed line shows the prediction for a weakly interacting Bose gas. The vertical dotted line indicates the critical temperature for Bose-Einstein condensation. For high evaporation percentages, the process becomes inefficient, leading to atom loss without significant further cooling, as we can see from the dark blue dot.

quantities.

In any case, a more detailed investigation of this expansion regime lies beyond the scope of this thesis and is deferred to future studies.

3.3.3 Time of flight analysis

An additional investigation that can be conducted on the bosonic gas involves examining its condensed fraction. As discussed in section 1.3.3, bosonic gas condensation occurs exclusively within momentum space. This poses challenges in identifying the condensed portion, particularly when compared to harmonic confinement scenarios. Consequently, to ascertain the condensed fraction, we utilize a complete time-of-flight analysis on a bosonic gas confined within a box potential.

The procedure for preparing the gas mirrors that of prior experiments, with the distinction that the DMD power is reduced to 70% of its starting value, and the Feshbach field is adjusted to 650 G. The DMDs create a box in this scenario with a parallelepiped shape, featuring a horizontal square base with sides of $100 \mu\text{m}$, and a vertical height of $25 \mu\text{m}$. Figure 3.15a displays an image of the trapped gas.

When the evaporation is completed, the gas is released from the trap and expands in the Feshbach harmonic potential. During this expansion, we perform measurements every millisecond, up to a maximum time of 41 ms. At long times of flight, the gas can be considered as being in momentum space, so that the spatial distribution directly reflects the momentum distribution. In this way, we are able to identify and measure the condensed fraction of the gas. In particular, 40 ms represents a very long expansion time: if the gas were purely thermal, its signal would be completely washed out after such a long time of flight. An image of the gas at 40 ms time of flight is shown in Fig. 3.15b.

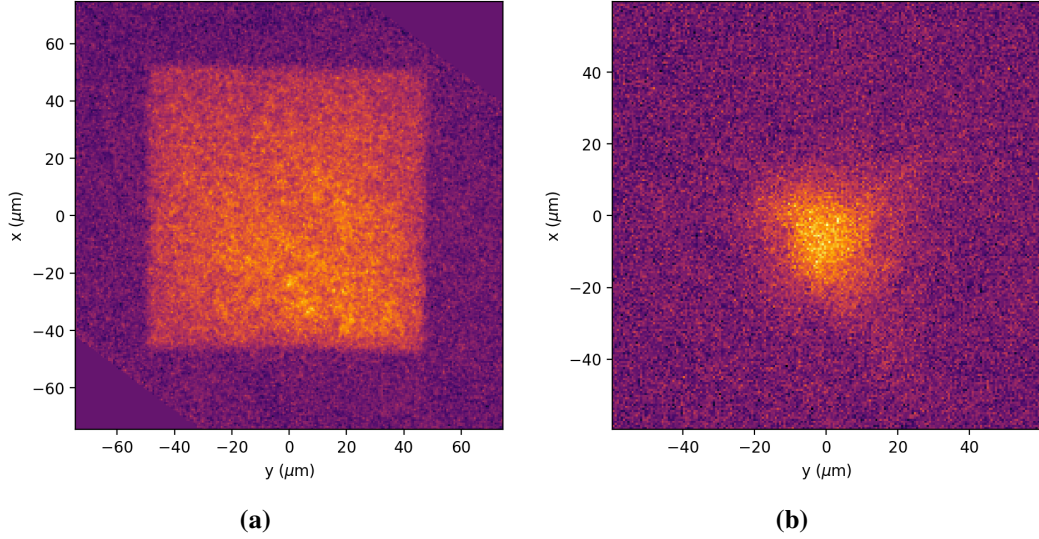


Figure 3.15. (a) Image of the gas in the box potential in the BEC⁶⁵⁰ regime, acquired with vertical imaging. The box has dimensions of $100 \times 100 \times 25 \mu\text{m}$. (b) Image of the gas after a 40 ms time-of-flight expansion. The presence of a significant signal after such a long expansion time indicates a substantial condensed fraction in the gas.

The recorded signal is then integrated along one direction in order to obtain the one-dimensional density profile. By performing a bimodal fit of this 1D profile, we can extract both the condensed and thermal contributions. More specifically, the bimodal fitting function is composed of two parts: the thermal component is described by the density of a Bose gas in ballistic expansion as [49]:

$$n_{th}(x) = -\frac{N}{\sqrt{\pi}R_{th} \text{Li}_{3/2}(e^{\beta\mu})} \ln \left[1 - e^{\beta\mu} e^{\frac{x^2}{R_{th}^2}} \right], \quad (3.16)$$

which corresponds to the one-dimensional case of Eq. (3.4).

The condensed component is instead fitted with the function

$$n_c(x) = A \text{sinc}(kx), \quad (3.17)$$

where A and k are fitting parameters. To verify the validity of this expansion, we evaluate both the interaction parameter na^3 and the mean free path λ_c . Concerning the interaction regime, although at this magnetic field the interaction strength is larger than in the cases studied in Sec. 3.3.2, the low density yields a value of $na^3 \simeq 2 \times 10^{-4} \ll 1$, which corresponds to the weakly interacting regime. For the mean free path, we find $\lambda_c \simeq 90 \mu\text{m}$, which is comparable to the largest edges of the parallelepiped-like box potential, of the order of $100 \mu\text{m}$. In any case, due to the fast expansion of the thermal cloud, its density rapidly decreases, and the system quickly reaches the ballistic regime shortly after the release from the trap. At sufficiently long times of flight, the non-ballistic part of the expansion can therefore be neglected, and the thermal component can be considered to be in the ballistic regime. The characteristic time at which this condition is reached is estimated following Eq. (3.11), giving a value of about 14 ms. The same argument, however, does not apply to the condensate. Owing to its slower expansion, the condensate density does not decrease fast

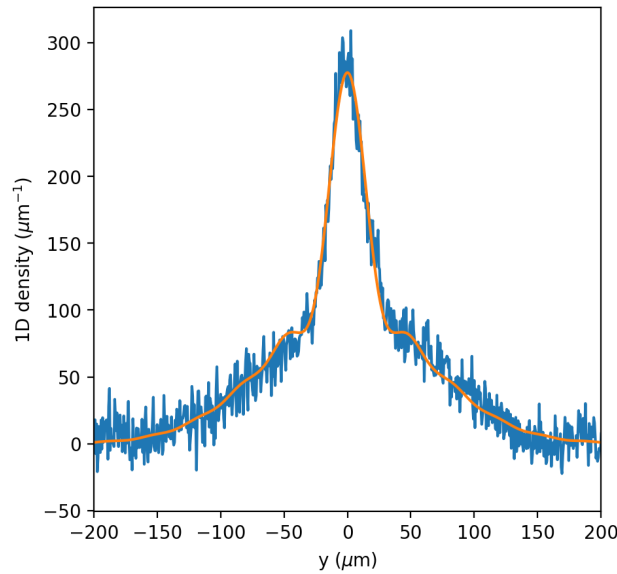


Figure 3.16. One-dimensional density profile of the atomic cloud after 40 ms time-of-flight expansion in the BEC⁶⁵⁰ regime. The blue line represents the experimental data, while the orange line is a bimodal fit composed of a polylogarithmic function (3.16) describing the thermal fraction and a Cartesian sinc function (3.17) corresponding to the condensed fraction. These two components allow for the quantitative determination of the thermal and condensed fractions in the system.

enough to enter the ballistic regime. Nevertheless, the fitting function of Eq. (3.17) remains valid: the condensate wavefunction, in the presence of interactions (see Sec. 1.3), follows the shape of the confining potential. In the present case, the trap is effectively box-like, so that the corresponding momentum distribution is given by the Fourier transform of a rectangular wavefunction, which corresponds to a sinc function, as in Eq.(3.17).

An example of the one-dimensional profile, together with the corresponding fit, is shown in Fig. 3.16. From the fit functions, we can compute the area under each curve, which is directly proportional to the number of atoms in the respective component. In this way, we can reconstruct the atom numbers of the system in both the condensed and thermal fractions.

As a consistency check, we verify that the total number of atoms obtained by summing the two contributions agrees with the total atom number measured directly by integrating the experimental images. Once this condition is verified, we define the condensed and thermal fractions as:

$$f_0 = \frac{N_0}{N_{\text{tot}}}, \quad f_{\text{th}} = \frac{N_{\text{th}}}{N_{\text{tot}}}, \quad (3.18)$$

where $N_{\text{tot}} = N_0 + N_{\text{th}}$. The corresponding results are shown in Fig. 3.17.

In order to ensure the validity of the assumptions underlying the fitting model, we restrict our analysis to measurements taken at expansion times larger than 15 ms. In this regime, the thermal cloud can still be treated as in the previous case, while the condensate distribution can also be reliably associated with momentum space. From these measurements we obtain a condensed fraction of approximately

$$f_0 = 0.27 \pm 0.09, \quad (3.19)$$

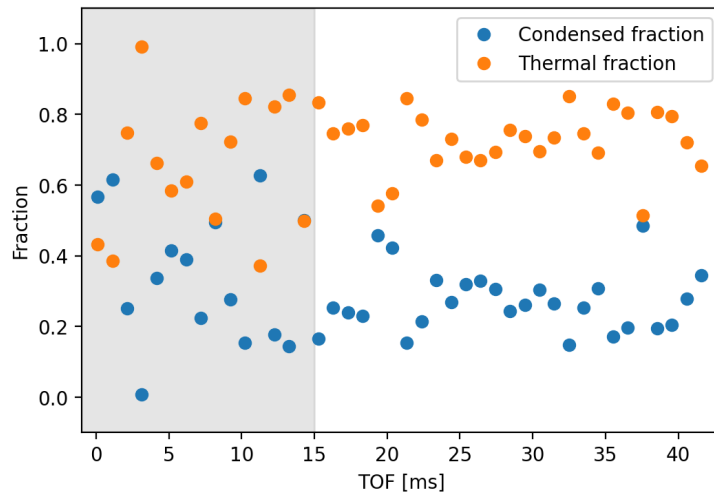


Figure 3.17. Condensed and thermal fractions of the atomic cloud in the BEC⁶⁵⁰ regime as a function of time-of-flight (TOF). The blue points show the condensed fraction and the orange points the thermal fraction, both extracted from bimodal fits to the density profiles. The shaded region indicates short TOF values, for which the time of flight is not sufficiently long and these points are not considered in the final value determination.

which represents a satisfactory outcome for a preliminary measurement.

By comparing this value with the results presented in Sec. 3.3.2, we can infer that a deeper evaporation in the box potential would likely lead to a higher condensed fraction. Moreover, it would be of great interest to measure the condensed fraction as a function of the gas temperature. Such measurements would allow one to reconstruct the behavior predicted by Eq. (1.55), where the scaling exponent differs significantly from the harmonic case of Eq. (1.54). In particular, deviations from the exponent $3/2$ could provide insight into the effective steepness of the box potential, which may be modeled as $V(r) \sim r^\alpha$.

A detailed analysis of these aspects, however, goes beyond the scope of this thesis.

Chapter 4

Conclusions and outlooks

Conclusions

The work presented in this thesis has focused on the realization and characterization of a uniform optical potential for ultracold ^6Li atoms, based on the use of Digital Micromirror Devices (DMDs). More in details I focused my work on the simulation, engineering, and implementation of the optical setup specifically for the vertical confinement. The developed setup enabled the creation of a box-like confinement along the vertical direction, providing a homogeneous three-dimensional potential when combined with the already existing horizontal confinement. Through careful optical design, precise alignment, and the implementation of active feedback control, the system achieved the degree of uniformity required to reproduce the physics of homogeneous quantum systems.

On the experimental side, we tested the quantum simulator with easy problems, in both fermionic and bosonic cases. The performed measurements demonstrated the capability to probe quantum statistics, revealing the paradigmatic signatures of Fermi and Bose distributions—showing that the achieved level of uniformity is sufficient to reproduce the expected behaviors. Furthermore, it was demonstrated that evaporative cooling of the box potential, with all the necessary precautions and calibrations, constitutes an effective and reliable technique to cool the gas.

In summary, the results of this thesis establish a solid experimental foundation for future investigations of homogeneous fermionic and bosonic systems. Together with the perspectives outlined in the following section, they highlight how the combination of precise optical engineering and advanced control of atomic interactions can open new avenues for the exploration of quantum many-body physics in uniform potentials.

Outlooks

The realization of uniform box potentials for ultracold atomic gases establishes a versatile platform for exploring many-body quantum physics under well-controlled and homogeneous conditions. A fundamental next step will be the thorough characterization of the implemented potential. This includes a detailed assessment of its spatial uniformity, residual roughness, and temporal stability. In particular, we aim to characterize the potential by expressing it as a power-law function $V(r) = r^\alpha$, where α quantifies the degree of “boxiness” of the trap. Such a careful characterization is crucial to ensure that the experimental system closely

approximates an ideal flat-bottom trap, which is essential for the reliable interpretation of subsequent quantum gas experiments. Thanks to the homogeneous potential, it will also be possible to implement a radio-frequency technique for temperature measurements of the unitary Fermi gas (UFG) [50], providing a precise and non-invasive thermometric tool essential for characterizing strongly interacting quantum gases.

If the parameter α is sufficiently large, the potential can be well approximated by a uniform hard-wall box. In this case, it is particularly interesting to study Friedel oscillations—spatial density oscillations produced by the interference of the wavefunctions of atoms inside the box trap—which are expected to appear in ideal Fermi gas systems [51]. Observing these oscillations would demonstrate a textbook quantum-mechanical phenomenon that, to date, has never been measured in atomic fermionic systems.

Building upon this foundation, future research will focus on probing the collective excitations and quantum phases of fermionic superfluids confined in box potentials. In particular, the study of sound-wave propagation across the BEC–BCS crossover promises to shed light on the fundamental nature of quasiparticle interactions and hydrodynamics in strongly interacting Fermi systems. The ability to tune interactions and confine atoms in a homogeneous volume offers unprecedented opportunities to explore damping mechanisms and dispersion relations in superfluid matter.

Another exciting direction is the investigation of vortex dynamics and their interactions with sound in a uniform system. Understanding vortex–sound coupling is essential for unraveling the microscopic processes behind energy dissipation and quantum turbulence in superfluids [52, 53]. The controlled generation and detection of vortex dipoles within a box potential will allow new insight into these complex phenomena, potentially revealing novel coupling mechanisms unique to fermionic superfluids.

Moreover, the homogeneous trapping geometry opens the door to studying non-equilibrium dynamics [54], phase-transition kinetics[55], and universal scaling behavior in ultracold gases [23]. These experiments can provide stringent tests of theoretical models in statistical mechanics and quantum field theory, where homogeneous conditions are typically assumed, and that are inaccessible to classical computation. Finally, simulations performed with these systems can offer valuable insights and inspiration to theorists, guiding the development of new models and theories that advance our understanding of quantum many-body phenomena.

Appendix A

Atoms light interaction

A.1 Atom light interaction

Adopting a semiclassical approach, we can treat an atom as a quantum object with quantized internal states $|i\rangle$ and consider a classical monochromatic electromagnetic field:

$$\mathbf{E}(\mathbf{r}, t) = E_0(\mathbf{r})e^{i(\phi(\mathbf{r})-\omega t)}\hat{\mathbf{e}} + \text{c.c.} \quad (\text{A.1})$$

The Hamiltonian of the atom in the external field is:

$$H = H_A + H_I, \quad (\text{A.2})$$

where H_A is the unperturbed atomic Hamiltonian, whose eigenvectors correspond to the atomic energy levels, and H_I is the atom–light interaction Hamiltonian.

For a two-level atom in the dipole approximation, the interaction Hamiltonian is given by:

$$H_I = -\mathbf{d} \cdot \mathbf{E}(\mathbf{r}), \quad (\text{A.3})$$

where \mathbf{r} is the atomic center-of-mass position and \mathbf{d} is the atomic dipole operator, related to the field amplitude via the complex polarizability α :

$$\mathbf{d}(\omega) = \alpha(\omega)\mathbf{E}(\omega). \quad (\text{A.4})$$

In the Heisenberg picture, the force acting on the atom is:

$$\mathbf{F} = \frac{d\mathbf{p}}{dt} = \frac{i}{\hbar}[H, \mathbf{p}] = -\nabla H_I. \quad (\text{A.5})$$

Since the induced dipole moment can be considered independent of the atomic position, it can be taken outside the derivative, yielding $\mathbf{F} \propto \nabla \mathbf{E}(\mathbf{r})$. The electric field depends on position through both its amplitude and its phase. Therefore, the derivative of the field results in two contributions, associated with the gradient of the phase and of the amplitude, respectively.

The total force acting on the atom can thus be expressed as the sum of two terms:

$$\mathbf{F} = \mathbf{F}_{\text{scatt}} + \mathbf{F}_{\text{dip}}, \quad (\text{A.6})$$

where $\mathbf{F}_{\text{scatt}} \propto \nabla \phi(\mathbf{r})$ is the *scattering force*, arising from the absorption and re-emission of photons, and $\mathbf{F}_{\text{dip}} \propto \nabla E_0(\mathbf{r})$ is the *dipole force*, a non-dissipative force related to dispersion. While the first one is a dissipative force, so is used in the cooling processes, the second one is conservative, therefore is perfect to create trapping potentials for atoms.

A.2 Photon Absorption and Re-emission

Whenever an atom interacts with light, momentum conservation must be satisfied. Thus, when an atom absorbs or emits a photon, it recoils so that its momentum change compensates that of the absorbed or emitted photon. This light-induced change in momentum can be regarded as a force exerted by light on the atom.

The corresponding scattering force is given by

$$F_{\text{scatt}} = \hbar \mathbf{k} \Gamma_{\text{sc}}, \quad (\text{A.7})$$

where \mathbf{k} is the photon wavevector and Γ_{sc} is the scattering rate, such as the rate at which photons are absorbed and spontaneously re-emitted. Neglecting stimulated emission, we can write $\Gamma_{\text{sc}} = \Gamma \rho_{22}$, where Γ denotes the natural linewidth of the atomic transition and ρ_{22} is the probability of finding the atom in the excited state.

Considering laser light detuned by $\delta = \omega - \omega_0$ from the atomic resonance, the steady-state solution of the optical Bloch equations yields:

$$\Gamma_{\text{sc}}(r) = \frac{\Omega(r)^2/\Gamma}{1 + 2\Omega(r)^2/\Gamma^2 + 4\delta^2/\Gamma^2}, \quad (\text{A.8})$$

where Ω is the Rabi frequency describing the atom–field coupling:

$$\Omega(r) = \frac{\langle g | \hat{\mathbf{e}} \cdot \mathbf{d} | e \rangle E_0(r)}{\hbar}. \quad (\text{A.9})$$

The scattering rate exhibits an inverse quadratic dependence on the detuning, leading to a rapid decrease in photon absorption probability as the detuning increases.

Introducing the saturation intensity I_s , and expressing the field intensity as $I(r) = 2\epsilon_0 c |E_0(r)|^2$, Eq. A.8 can be rewritten as

$$\Gamma_{\text{sc}}(r) = \frac{\Gamma}{2} \frac{I(r)/I_s}{1 + I(r)/I_s + 4\delta^2/\Gamma^2}. \quad (\text{A.10})$$

This expression shows that the absorption probability increases linearly with intensity for $I \ll I_s$. The scattering force is bounded from above by the maximum value

$$F_{\text{scatt,max}} = \frac{\hbar k \Gamma}{2}, \quad (\text{A.11})$$

which is attained in the limit $I \gg I_s$.

A.3 Optical Dipole Force and Potentials

To cool atomic gases to degeneracy and manipulate them in a non-dissipative and coherent manner, it is customary to employ non-resonant light. For far-detuned light, photon absorption is strongly suppressed, allowing the exploitation of the dipole force as a conservative optical force acting on atomic samples. While the scattering force originates from the quadrature (out-of-phase) component of the induced dipole moment, or equivalently from the imaginary part of the polarizability α , the dipole force arises from the in-phase component of the dipole moment, corresponding to the real part of α .

The dipole force can be computed as

$$F_{\text{dip}}(r) = -\frac{\hbar\delta}{1 + 2\Omega(r)^2/\Gamma^2 + 4\delta^2/\Gamma^2} \nabla\Omega(r)^2. \quad (\text{A.12})$$

This expression can be rearranged to highlight the conservative nature of the dipole force, which derives from a potential:

$$F_{\text{dip}}(r) = -\nabla V_{\text{dip}}(r), \quad (\text{A.13})$$

with the dipole potential given by

$$V_{\text{dip}}(r) = \frac{\hbar\delta}{2} \log \left[1 + \frac{|\Omega(r)|^2}{2((\Gamma/2)^2 + \delta^2)} \right]. \quad (\text{A.14})$$

The optical dipole potential, V_{dip} , is the key mechanism that enables coherent laser-based manipulation of atoms. In the far-detuned regime, $|\delta| \gg \Gamma, \Omega$, it simplifies to

$$V_{\text{dip}}(r) \simeq \frac{\hbar|\Omega(r)|^2}{4\delta}. \quad (\text{A.15})$$

Expressed in terms of the saturation parameter $s = I/I_s$, this becomes

$$V_{\text{dip}}(r) \simeq \frac{3\hbar\Gamma^2}{8\delta} \frac{I(r)}{I_s} = \frac{3\hbar\Gamma^2}{8\delta} s(r), \quad (\text{A.16})$$

where the factor 3 accounts for the possible light polarization states.

Thus, atoms exposed to non-resonant light experience an optical potential proportional to the light intensity and inversely proportional to the detuning. Red-detuned light ($\omega < \omega_0$) creates attractive potentials, whereas blue-detuned light ($\omega > \omega_0$) generates repulsive potentials. Importantly, while the scattering rate scales as $1/\delta^2$, the dipole potential scales as $1/\delta$, making far-detuned light particularly advantageous: at large detuning, scattering is strongly suppressed while sizable optical potentials can still be realized. Moreover, unlike the scattering force, which saturates at high intensities, the dipole potential continues to grow with increasing intensity, though only logarithmically at very large values.

The flexibility in shaping the spatial intensity profiles of laser beams allows the engineering of both attractive and repulsive dipole potentials for manipulating ultracold atomic samples. Specifically, attractive red-detuned gaussian beams form optical dipole traps (ODTs) that confine atoms in regions of high intensity, while repulsive blue-detuned beams can create tailored geometries or repulsive ODTs within the atomic ensemble. Both types of beams can thus be employed to produce versatile trapping potentials for ultracold atoms.

We stress that expression ((A.16)), although it captures the general behavior of atoms exposed to non-resonant light, should be used with caution, as it relies on three assumptions that may not always be valid.

- (1) The first assumption is the rotating wave approximation, such as $\omega - \omega_0 \ll \omega + \omega_0$, which allows us to neglect terms proportional to $1/(\omega + \omega_0)$. In the range of optical atomic transitions, this condition is generally satisfied.

- (2) The second assumption is that the detuning δ from the atomic transition is much larger than the transition linewidth Γ . This is typically the case when employing optical potentials for manipulating atoms with non-resonant light, since a detuning comparable to the linewidth would result in a high probability of photon absorption.
- (3) The third assumption is the two-level approximation, which is, in general, not strictly valid. Atoms in a given state typically have many accessible higher-energy excited states, and deciding which transitions can be neglected is an important consideration. Usually, one transition has the smallest detuning from the light frequency; this is the transition taken into account in the two-level approximation. Transitions with significantly larger detunings can be neglected, as well as those whose energy splittings are so small that they cannot be resolved, in which case they contribute effectively as a single transition with the appropriate degeneracy.

An alternative way of describing optical potentials is through the picture of light shifts, or dressed states. This approach is equivalent to the previous treatment but particularly appealing for describing state-dependent optical potentials. In this framework, interaction between the light's electromagnetic field and the internal atomic levels induces an energy shift of the levels, which become "dressed" by the interaction. For the ground state of the transition, these light shifts (AC Stark shifts) are negative (positive) for red (blue) detuned light, leading to an effective attraction (repulsion) toward (away from) regions of high light intensity.

Acknowledgements

We now come to the acknowledgements, where I will focus on the lab-related ones — the others will find their way through different channels.

First of all, I would like to thank **Giulia**, who, even if a bit surprised (at least from what I felt) by the fact that I accepted the thesis project she had proposed, welcomed me warmly and made me feel part of the group. Together with **Marcia**, they are also the point of reference for everyone when it comes to stylistic matters.

Moving on to **Diego**, conversations with him are always stimulating and formative. Reading his coding, written as naturally as if he were signing his name, is truly impressive.

As for **Nicola**, his advice on any topic he has just dealt with — and which invariably turns out to be right — is invaluable.

Finally, **Giacomo**: your “Milan-style” encouragements to work, as well as our always enlightening discussions, have been essential for efficient and well-thought-out work. I also want to thank you for the opportunities you offered me, such as the one in Cargèse.

Bibliography

1. Bloch, I., Dalibard, J. & Zwirger, W. Many-body physics with ultracold gases. en. *Rev. Mod. Phys.* **80**, 885–964 (July 2008).
2. Gross, C. & Bloch, I. Quantum simulations with ultracold atoms in optical lattices. en. *Science* **357**, 995–1001 (Sept. 2017).
3. Sobirey, L. *et al.* Observation of superfluidity in a strongly correlated two-dimensional Fermi gas. en. *Science* **372**, 844–846 (May 2021).
4. Guo, Y. *et al.* Observation of the 2D–1D crossover in strongly interacting ultracold bosons. en. *Nat. Phys.* **20**, 934–938 (June 2024).
5. Dyke, P. *et al.* Crossover from 2D to 3D in a weakly interacting Fermi gas. en. *Phys. Rev. Lett.* **106**, 105304 (Mar. 2011).
6. Peppler, T. *et al.* Quantum anomaly and 2D-3D crossover in strongly interacting Fermi gases. en. *Phys. Rev. Lett.* **121** (Sept. 2018).
7. Albiez, M. *et al.* Direct observation of tunneling and nonlinear self-trapping in a single bosonic Josephson junction. en. *Phys. Rev. Lett.* **95**, 010402 (July 2005).
8. Gauthier, G. *et al.* in *Advances In Atomic, Molecular, and Optical Physics* 1–101 (Elsevier, 2021).
9. Veeravalli, G., Kuhnle, E., Dyke, P. & Vale, C. J. Bragg spectroscopy of a strongly interacting Fermi gas. en. *Phys. Rev. Lett.* **101**, 250403 (Dec. 2008).
10. Weimer, W. *et al.* Critical velocity in the BEC-BCS crossover. en. *Phys. Rev. Lett.* **114**, 095301 (Mar. 2015).
11. Abo-Shaeer, J. R., Raman, C., Vogels, J. M. & Ketterle, W. Observation of vortex lattices in Bose-Einstein condensates. en. *Science* **292**, 476–479 (Apr. 2001).
12. Gaunt, A. L., Schmidutz, T. F., Gotlibovych, I., Smith, R. P. & Hadzibabic, Z. Bose-Einstein condensation of atoms in a uniform potential. en. *Phys. Rev. Lett.* **110**, 200406 (May 2013).
13. Mukherjee, B. *et al.* Homogeneous Atomic Fermi Gases. *Phys. Rev. Lett.* **118** (Mar. 2017).
14. Hueck, K. *et al.* Two-dimensional homogeneous Fermi gases. *Phys. Rev. Lett.* **120** (Feb. 2018).
15. Anderson, M. H., Ensher, J. R., Matthews, M. R., Wieman, C. E. & Cornell, E. A. Observation of bose-einstein condensation in a dilute atomic vapor. en. *Science* **269**, 198–201 (July 1995).

16. Dalibard, J. & Cohen-Tannoudji, C. in *Atomic and Molecular Beams* 43–62 (Springer Berlin Heidelberg, Berlin, Heidelberg, 2001).
17. Navon, N., Smith, R. P. & Hadzibabic, Z. Quantum gases in optical boxes. en. *Nat. Phys.* **17**, 1334–1341 (Dec. 2021).
18. Pitaevskii, L. & Stringari, S. en. in *Bose-Einstein Condensation and Superfluidity* 15–28 (Oxford University Press Oxford, Jan. 2016).
19. Caraci, C., Cenatiempo, S. & Schlein, B. The excitation spectrum of two-dimensional Bose gases in the Gross-Pitaevskii regime. en. *Ann. Henri Poincaré* **24**, 2877–2928 (Mar. 2023).
20. Pelissetto, A. & Vicari, E. Renormalization-group flow and asymptotic behaviors at the Berezinskii-Kosterlitz-Thouless transitions. *Phys. Rev. E Stat. Nonlin. Soft Matter Phys.* **87** (Mar. 2013).
21. Jiang, X. *et al.* Domain formation and universally critical dynamics through phase separation in two-component Bose-Einstein condensates. en. *Phys. Rev. A (Coll. Park.)* **110** (Dec. 2024).
22. Beugnon, J. & Navon, N. Exploring the Kibble-Zurek mechanism with homogeneous Bose gases. eprint: 1611.01145 (cond-mat.quant-gas) (2016).
23. Eigen, C. *et al.* Universal scaling laws in the dynamics of a homogeneous unitary Bose gas. en. *Phys. Rev. Lett.* **119** (Dec. 2017).
24. Su, L. *et al.* Fast single atom imaging for optical lattice arrays. en. *Nat. Commun.* **16**, 1017 (Jan. 2025).
25. Del Pace, G. *et al.* Imprinting persistent currents in tunable fermionic rings. en. *Phys. Rev. X* **12** (Dec. 2022).
26. Polo, J. *et al.* Persistent currents in ultracold gases. en. *Phys. Rep.* **1137**, 1–70 (Sept. 2025).
27. Amico, L. *et al.* Roadmap on Atomtronics: State of the art and perspective. en. *AVS Quantum Sci.* **3**, 039201 (Sept. 2021).
28. Kaufman, A. M. & Ni, K.-K. Quantum science with optical tweezer arrays of ultracold atoms and molecules. en. *Nat. Phys.* **17**, 1324–1333 (Dec. 2021).
29. Feynman, R. P. Simulating physics with computers. en. *Int. J. Theor. Phys.* **21**, 467–488 (June 1982).
30. Pathria, R. K. & Beale, P. D. in *Statistical Mechanics* 1–23 (Elsevier, 2011).
31. DeMarco, B. & Jin, D. S. Onset of fermi degeneracy in a trapped atomic Gas. en. *Science* **285**, 1703–1706 (Sept. 1999).
32. Pitaevskii, L. P. & Stringari, S. *Bose-Einstein Condensation* en (Clarendon Press, Oxford, England, Apr. 2003).
33. Chin, C., Grimm, R., Julienne, P. & Tiesinga, E. Feshbach resonances in ultracold gases. en. *Rev. Mod. Phys.* **82**, 1225–1286 (Apr. 2010).
34. Landau, L. D. & Lifshitz, E. M. *Quantum mechanics: Non-relativistic theory* en (Elsevier, Amsterdam, Netherlands, Oct. 2013).

35. Regal, C. A., Greiner, M. & Jin, D. S. Observation of resonance condensation of fermionic atom pairs. en. *Phys. Rev. Lett.* **92**, 040403 (Jan. 2004).
36. Ketterle, W. & Zwierlein, M. W. Making, probing and understanding ultracold Fermi gases. *Rivista del Nuovo Cimento* **31**, 247–422 (2008).
37. Del Pace, G. *Tunneling transport in strongly-interacting atomic fermi gases* PhD thesis (Università degli Studi di Firenze, 2020).
38. Pethick, C. J. & Smith, H. *Bose-Einstein condensation in dilute gases* 2nd ed. (Cambridge University Press, Cambridge, England, Jan. 2011).
39. Giorgini, S., Pitaevskii, L. P. & Stringari, S. Theory of ultracold atomic Fermi gases. en. *Rev. Mod. Phys.* **80**, 1215–1274 (Oct. 2008).
40. Valtolina, G. *Superfluid and spin dynamics of strongly interacting atomic Fermi gases* PhD thesis (Scuola Normale Superiore di Pisa, 2016).
41. Hecht, E. *Optics* 4th ed. en (Pearson, Upper Saddle River, NJ, Feb. 2003).
42. Amico, A. *Probing the many body dynamics of ultracold repulsive Fermi gases of Lithium atoms*. PhD thesis (Università degli Studi di Firenze, 2018).
43. Hueck, K. *et al.* Calibrating high intensity absorption imaging of ultracold atoms. en. *Opt. Express* **25**, 8670 (Apr. 2017).
44. Del Pace, G. *Tailored optical potentials for experiments with atomic superfluids* MA thesis (Università degli studi di Firenze, 2017).
45. IEEE Spectrum, L. H. *Chip Hall of Fame: Texas Instruments Digital Micromirror Device* tech. rep. (Texas Instruments, 1987).
46. Popoff, S. M., Shih, G., Boonzajer, D. & GustavePariente. *wavefrontshaping/ALP4lib: 1.0.3* 2025.
47. Gotlibovych, I. *Degenerate Bose Gases in a Uniform Potential* PhD thesis (University of Cambridge, 2014).
48. LeVeque, R. J. *Finite difference methods for ordinary and partial differential equations* (Society for Industrial and Applied Mathematics, Jan. 2007).
49. Ketterle, W., Durfee, D. S. & Stamper-Kurn, D. M. in *Bose-Einstein Condensation in Atomic Gases* 67–176 (IOS Press, Amsterdam, NY, 1999).
50. Mukherjee, B. *et al.* Spectral response and contact of the unitary Fermi gas. en. *Phys. Rev. Lett.* **122**, 203402 (May 2019).
51. Simion, G. E. & Giuliani, G. F. Friedel oscillations in a Fermi liquid. *Phys. Rev. B Condens. Matter Mater. Phys.* **72** (July 2005).
52. Tsatsos, M. C. *et al.* Quantum turbulence in trapped atomic Bose–Einstein condensates. en. *Phys. Rep.* **622**, 1–52 (Mar. 2016).
53. Sonin, E. B. *Dynamics of Quantised Vortices in Superfluids* (Cambridge University Press, Cambridge, England, Feb. 2016).
54. Navon, N. *et al.* Synthetic dissipation and cascade fluxes in a turbulent quantum gas. en. *Science* **366**, 382–385 (Oct. 2019).

55. Navon, N., Gaunt, A. L., Smith, R. P. & Hadzibabic, Z. Quantum gases. Critical dynamics of spontaneous symmetry breaking in a homogeneous Bose gas. en. *Science* **347**, 167–170 (Jan. 2015).